

**ON DESIGN FOR  
ELECTROCHEMICAL ENERGY STORAGE MATERIALS**

**DISSERTATION**

**zur Erlangung des akademischen Grades**

**Doctor of Philosophy**

**(Ph. D.)**

Vorgelegt

**der Fakultät Mathematik und Naturwissenschaften**

**der Technischen Universität Dresden**

von

**Ken Sakaushi**

**坂牛 健**

geboren am 22.07.1985 in Tokyo, Japan

Eingereicht am 24.04.2013

Die Dissertation wurde in der Zeit von Oktober 2010 bis März 2013  
am Institut für Anorganische Chemie der TU Dresden und IFW Dresden  
gefördert durch den Deutschen Akademischen Austauschdienst angefertigt.

Gedruckt mit Unterstützung des  
Deutschen Akademischen Austauschdienstes.

# ON DESIGN FOR ELECTROCHEMICAL ENERGY STORAGE MATERIALS

## -TABLE OF CONTENTS-

<b>Preface</b>	<i>1</i>
<b>1. Introduction: Challenge for the energy issues in the 21<sup>st</sup> century</b>	<i>4</i>
<b>2. Materials for electrochemical energy storage: A review on energy storage mechanism and properties</b>	<i>10</i>
2.1. Introduction	<i>10</i>
2.2. Intercalation compounds	<i>12</i>
2.3. Materials for conversion reactions	<i>15</i>
2.4. Organic materials for energy storage devices	<i>16</i>
2.5. Other possible materials for energy storage devices	<i>18</i>
2.6. Summary for the chapter 2	<i>19</i>
<b>3. Analytical techniques</b>	
3.1. Reagents	<i>21</i>
3.2. Characterization Techniques	<i>22</i>
3.2.1. X-Ray Diffraction (XRD) measurements	<i>22</i>
3.2.2. Transmission Electron Microscopy (TEM)	<i>24</i>
3.2.3. Scanning Electron Microscopy (SEM)	<i>26</i>
3.2.4. N <sub>2</sub> physisorption measurements	<i>27</i>
3.2.5. Fourier Transform-Infrared (FT-IR) and Raman spectroscopy measurements	<i>29</i>
3.3. Electrochemical measurements	<i>30</i>
3.3.1. Fundamental theory of electrochemical reaction	<i>30</i>
3.3.2. Constant current change potential (CCCP) method	<i>37</i>
3.3.3. Galvanostatic intermittent titration technique (GITT)	<i>38</i>
3.3.5. Electrochemical impedance spectroscopy (EIS) analysis	<i>41</i>

**4. Synthesis of nanostructured 1D MoO<sub>3</sub> and its Application to cathode and anode for lithium-ion batteries 42**

- 4.1. Introduction 42
- 4.2. Experiment 47
- 4.3. Results and discussion 48
  - 4.3.1. Synthesis of 1D MoO<sub>3</sub> 48
  - 4.3.2. Electrochemical properties of 1D MoO<sub>3</sub> 51
  - 4.3.3. Self-assembly of 1D MoO<sub>3</sub> towards oxide papers 54
- 4.4. Summary for the chapter 4 59

**5. An energy storage principle using bipolar porous polymeric frameworks 60**

- 5.1. Introduction for the chapter 5 60
- 5.2. Experiment 62
  - 5.2.1. Synthesis of porous polymeric frameworks (PPFs) 62
  - 5.2.2. Physical characterization 63
  - 5.2.3. Electrochemical measurements 63
- 5.3. Lithium-organic energy storage devices 65
  - 5.3.1. Introduction 65
  - 5.3.2. Results and discussion 66
  - 5.3.3. Conclusion for lithium-organic energy storage device 81
- 5.4. Sodium-organic energy storage devices 82
  - 5.4.1. Introduction 82
  - 5.4.2. Results and discussion 83
  - 5.4.3. Conclusion for sodium-organic energy storage device 95
- 5.5. All-organic energy storage devices 96
  - 5.5.1. Introduction 96
  - 5.5.2. Results and discussion 97
  - 5.5.3. Conclusion for all-organic energy storage device 101
- 5.6. Electronic structures and electrochemical properties of PPFs 101
  - 5.6.1. Introduction 101
  - 5.6.2. Results and discussion 103
  - 5.6.3. Conclusion for electronic structures and electrochemical properties of PPFs 109
- 5.7. Summary for the chapter 5 110



<b>6.</b>	<b>Porous carbon/sulfur composites towards high-power lithium-sulfur battery cathodes</b>	<i>111</i>
6.1.	Introduction	<i>111</i>
6.2.	Experiment	<i>112</i>
	6.2.1. Fabrication of carbon/sulfur composites	<i>112</i>
	6.2.2. Electrochemical measurements for Li-S batteries	<i>113</i>
6.3.	Results and Discussion	<i>113</i>
6.4.	Summary for the chapter 6	<i>121</i>
<b>7.</b>	<b>Summary and future prospects</b>	<i>122</i>
<b>8.</b>	<b>Scientific achievements related to the project</b>	<i>125</i>
<b>9.</b>	<b>Acknowledgement</b>	<i>130</i>
<b>10.</b>	<b>References</b>	<i>132</i>
<b>Appendix</b>		<i>141</i>
<b>A-1.</b>	HRTEM images of CTF-1	<i>141</i>
<b>A-2.</b>	<i>Ab-initio</i> calculation and tight-binding model	<i>143</i>

*Dilige et quod vis fac.*  
Aurelius Augustinus (354 – 430 A. D.)

# PREFACE

Electrical energy supply is one of the most important fundamental challenges of our modern life. We, human beings living in the 21<sup>st</sup> century, cannot imagine a life without PCs and cell phones. You will find that these devices need electrical energy supplied from batteries to work. From this point of view, even for modern economics and politics in several countries, these systems depend on electricity, for example, online trading and electric voting systems operated from smart phones. This fact shows that rechargeable batteries are one of the most important key devices for a modern social life. Although, rechargeable battery system is a classical energy storage system since the invention of the first rechargeable battery system, i.e. lead batteries, by R. Plante in 1859, rechargeable battery systems are still of great interests due to the following electrical energy issue; ongoing dramatic increase in population and resulting high demand on the limited fossil fuels in future are potential causes of crisis which originates in the necessity of electricity. This suggests that, by mastering the electrical energy supply, we can not only improve our life standard but also contribute to society needs. Therefore, a large number of researchers all over the world are working on the electrical generating system, such as photovoltaic and wind power. However, there is a question: electricity needs a grid to go through and a destination to be stored. Yes, we have the “same” question: “*Quo vadis, Domine*”. One of the reasons for the battery research being urgent is that there are still no suitable batteries for grid applications combined with renewable energy, i.e. a smart grid, and for electronic vehicles.

This dissertation was written based on the research project supported by Deutscher Akademischer Austausch Dienst (DAAD) from year 2010 to 2013: Project number A/09/74990. The motivation of the project was to design electrode materials for next-generation rechargeable batteries in order to address to a crucial issue on our society mentioned above. Here, I am deeply indebted to DAAD for giving me an opportunity to build own research project in Germany.

January 2013, Tokyo, Japan

Ken Sakaushi

*Ich gehe gerne, weil ich fühle, daß es sein muß, und weil ich heute etwas so Wunderbars erlebt habe. Aber ich denke mir nicht, daß ich in lauter Glück und Vergnügen hineinlaufe. Ich denke mir, der Weg wird schwer sein. Und doch wird er auch schön sein, hoffe ich. Es ist für mich der Weg zum Leben und der Weg zum Sinn des Lebens.*

*Narziß und Goldmund* **1930**, Hermann Hesse (1877 – 1962 A. D.)

# CHAPTER 1. INTRODUCTION: CHALLENGE FOR THE ENERGY ISSUES IN THE 21<sup>st</sup> CENTURY

The chapter 1 shows the introduction indicating what kinds of electrode materials have potential to be applied to the next generation batteries and why so. There are two main themes in this chapter: (I) possible electrical energy storage system towards smart grid and electric vehicles (EVs) and (II) the issue on the affordability of batteries. Why energy storage system is important? This is because batteries will be the key device for a sustainable energy systems based on renewable energy. It is an urgent issue to establish a platform for use of renewable energy due to climate change and high demand for the limited fossil fuels.<sup>1-6</sup> It has been already predicted that peak-oil, -coal, and natural gas have passed and will be decreasing their production in 2020s.<sup>7,8</sup> Energy is one of the most important requirements from our modern life. It is the grand challenge in the 21<sup>st</sup> century to be independent from Earth's legacy and to build a certain technology which can make sure that our children can live in peace.<sup>9</sup> Figure 1-1 shows variations of electricity production from wind power and sun light.<sup>10</sup> It is clear that these systems cannot produce electricity constantly by themselves because the energy generation systems are completely dependent on the Mother Nature. Here, if we put together batteries with such renewable energy, we can stabilize the distribution of electricity from bulk generation to residential.<sup>11</sup>

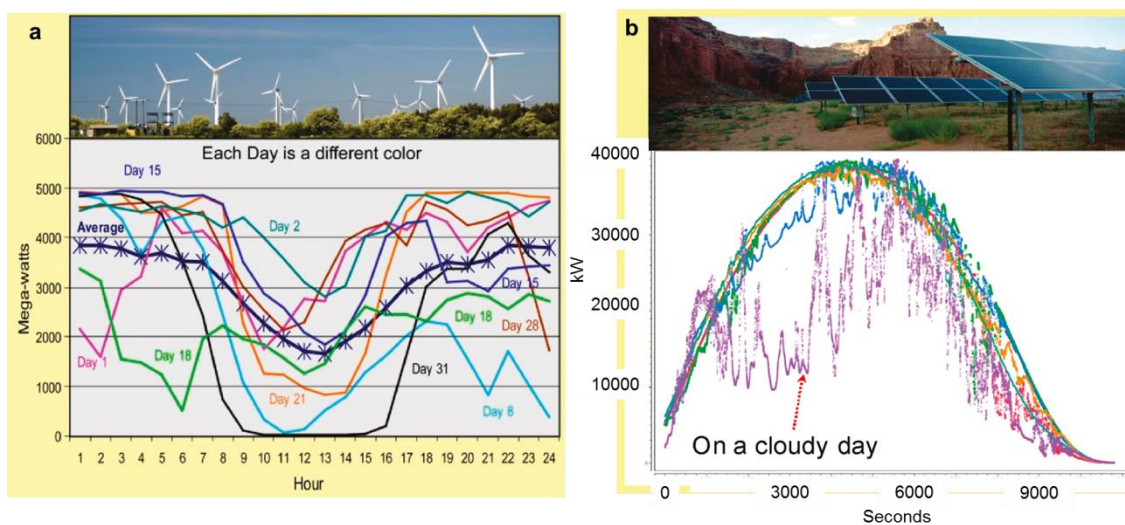


**Figure 1-1 | Electricity production from wind power and photovoltaic (PV).** (a) Daily profile of wind power in California. (b) 5 MW PV power over a span of 6 days in Spain. Reprinted with permission from ref. 10. Copyright (2011) American Chemical Society. (b) was modified by the author.

Therefore, there is a strong need for batteries which can repeat storage and supply a large amount of electrical energy in a small volume in a short time, i.e. batteries with high energy density and high power density.<sup>1,3,10</sup> Li-ion battery (LIB) system has both a high energy density and high power. Figure 1-2 shows a variety of energy storage devices and their electrochemical properties.<sup>12</sup> From Figure 1-2a, we can find that there are several candidates which have better rate performances compared to LIBs. However, if we check both specific energy and power (1-2b), we confirm that LIBs are the best devices having both high specific energy and power. LIBs can show higher energy density than other electrical energy storage systems. This is simply because lithium is the most electropositive element ( $-3.04$  V vs. SHE) and also is a light element (density is  $0.53$  g/cm<sup>3</sup>).<sup>13</sup> This nature enables to design an energy storage device having a high energy density, which can enable to make portable batteries. High-power, -energy feature is important for electronic vehicles (EVs). From this point of view, LIBs are serious candidates for an energy storage device which is expected to be combined with renewable energies such as solar power and wind power.<sup>1-4,10-12</sup>

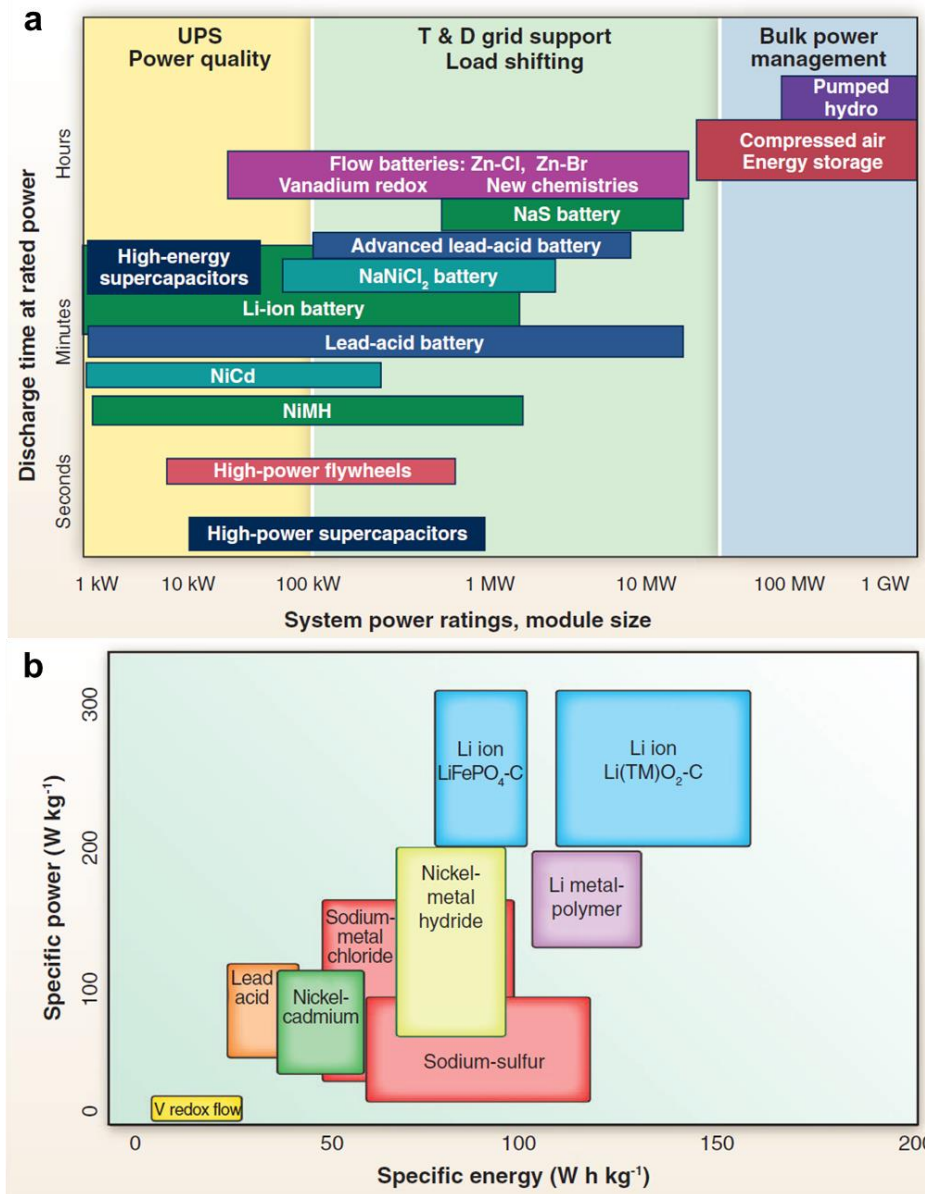


**Figure 1-2 | Electrochemical performances of various energy storage devices.** (a) Comparison of discharge time and rate performance for a various energy storage devices. (b) Specific energy and power for some rechargeable batteries which are investigated for grid storage applications. Reprinted from ref. 12. with permission from AAAS.

Therefore, intensive research for LIBs is currently running from fundamental science to technology close to industry under highly competitive conditions even though this system was commercialized in 1991 by Sony. However, a question has been arisen whether the LIBs'



gravimetric and volumetric energy are enough or not. In conclusion, current battery community and industrial field are thinking that current batteries are not enough to use in grid and EVs.<sup>1,3,4</sup> This is because, for example, i-MiEV, a recent commercialized EV produced from Mitsubishi Motors, can run only ~180 km from full-charged state.<sup>14</sup> This means we cannot go and back between Berlin and Dresden. Therefore, current issue on battery community is the development of “Next-generation electrical energy devices”. As candidates for the next-generation batteries, lithium-air batteries (LABs) and lithium-sulfur batteries (LSBs) are considered due to their super-large theoretical specific energy.<sup>15</sup> Although the cost of lithium-ion batteries (LIBs) is decreasing faster, where its cost was ~2000 \$/kWh in 2008 but LG Chem showed ~400 \$/kWh LIBs in 2011,<sup>16</sup> which will constitute the Chevrolet Volt manufactured by General Motors,<sup>17</sup> it is still expensive. In Figure 1-3, the expected driving distance and price in U.S. \$/kWh is shown for rechargeable batteries.<sup>15</sup> From this figure, we will find that battery system with less than 150 \$/kWh is a criteria for next-generation batteries. It is a very tough challenge to achieve a high-performance energy storage with cost of 150 \$/kWh if you check the price of Ni-MH batteries (= 900 \$/kWh), which is applied to current hybrid vehicles, such as Toyota Prius.<sup>18</sup> Our task is as follows; we have to reduce the cost more than half and improve the energy density more than double. These cost and cell performance issues above tells us that any promising battery system should be affordable. Thus, we have to design new materials to satisfy these harsh however vital criteria for future technology.

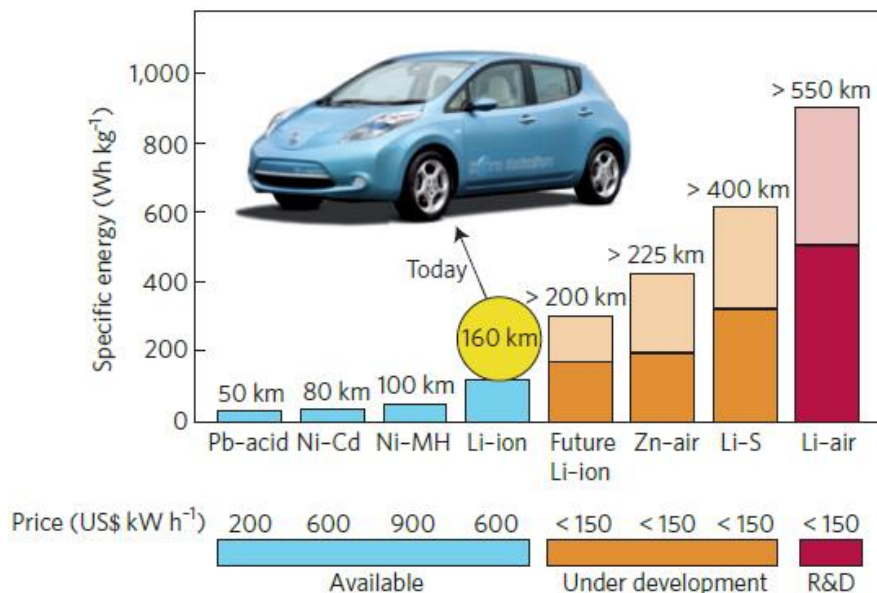


**Figure 1-3 | Practical specific energy for a various rechargeable batteries, along with estimated driving distance and packed price.** Reprinted by permission from Macmillan Publishers Ltd: [Nature Materials] (ref. 15), copyright (2012).

The importance lies not in “*Discover*” but in “*Design*”. Design is essential because, almost all key materials for electrochemical energy storage have been found until 1980s.<sup>19</sup> Therefore, improvement of these “*old*” energy storage systems will be given by combination of such old knowledge discovered until the 20<sup>th</sup> century and new aspects of science which were born in the 21<sup>st</sup> century. We have to synthesize promising electrode materials not only by depending on experiences but also by certain knowledge and principles toward purely artificial materials. In addition to design of new electrodes, from point of practical application, affordable

synthetic routes could contribute to realize an affordable, high-performance energy storage device.

# CHAPTER 2. MATERIALS FOR ELECTRO-CHEMICAL ENERGY STORAGE: A REVIEW ON THEIR MECHANISMS AND PROPERTIES

## 2. 1. INTRODUCTION

The importance of affordability was already discussed in the last chapter. Novel electrode materials should be designed with consideration of both cost-effectiveness and high-performance. Even though it is often that expensive element, such as cobalt, gold, platinum, and rhodium, showing great performance; but we have to think beyond in order to achieve next-generation batteries. In this chapter, typical compounds for each electrical energy storage system are introduced with a consideration of affordability mentioned above.

First of all, we should think how much batteries are necessary if we begin to introduce batteries in our daily life. This discussion was already pointed out by Murphy and Pickerd, respectively.<sup>20,21</sup> Murphy has claimed that we would need “*a nation-sized battery*”; if we assume Lead-acid batteries are utilized as base-storage of smart grid in U.S. to supply whole electricity in this country, the battery requires five billion tons of lead in total. Unfortunately, the Earth does not have enough lead even for U.S. alone to build grid based on lead-acid batteries because estimated lead resources of the world is 1.5 billion tons.

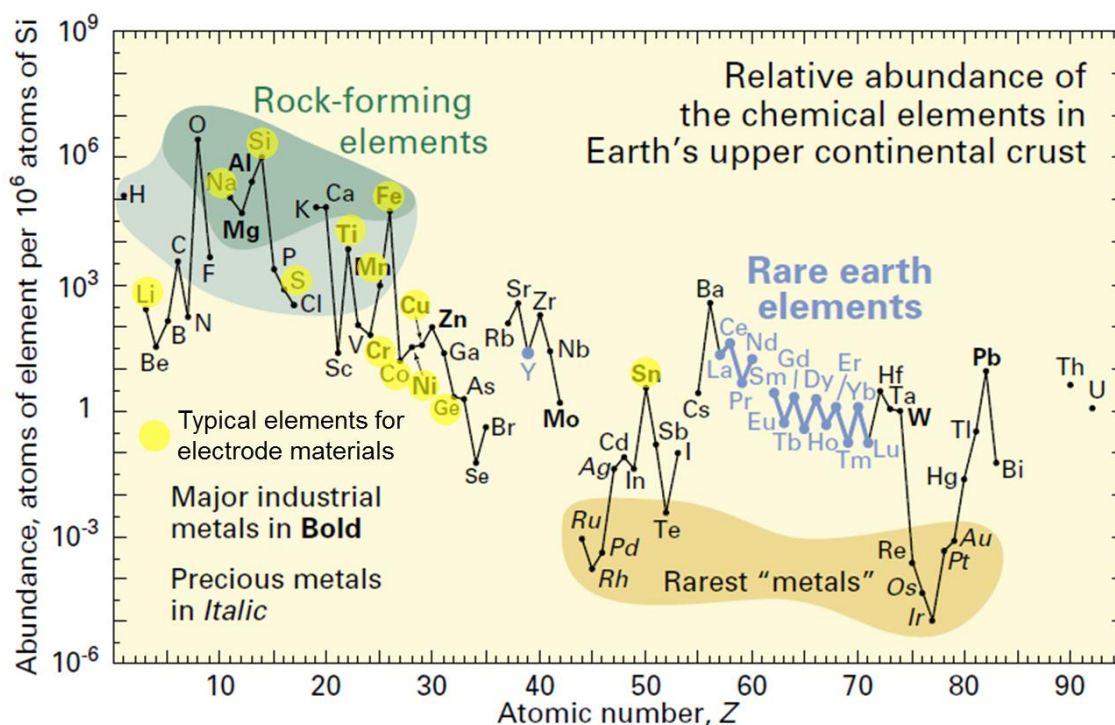


**Figure 2-1 | Abundance of the chemical elements in Earth's upper continent crust as a function of atomic number.** Reprinted from ref. 22. The author modified the original figure to show the typical elements for electrode materials in batteries.

Therefore, the strategy for building new batteries will come to start from checking the abundance of elements (Figure 2-1).<sup>22</sup> Next, the abundance of metals is also important because metal cations are major redox center for the electrochemical reaction in cathode materials. From this point of view, iron and titanium are abundant. For instance, NaFePO<sub>4</sub>//TiO<sub>2</sub> cell is a very promising battery system from the point of material's existence aside electrochemical properties.

## 2. 2. INTRCALATION COMPOUNDS

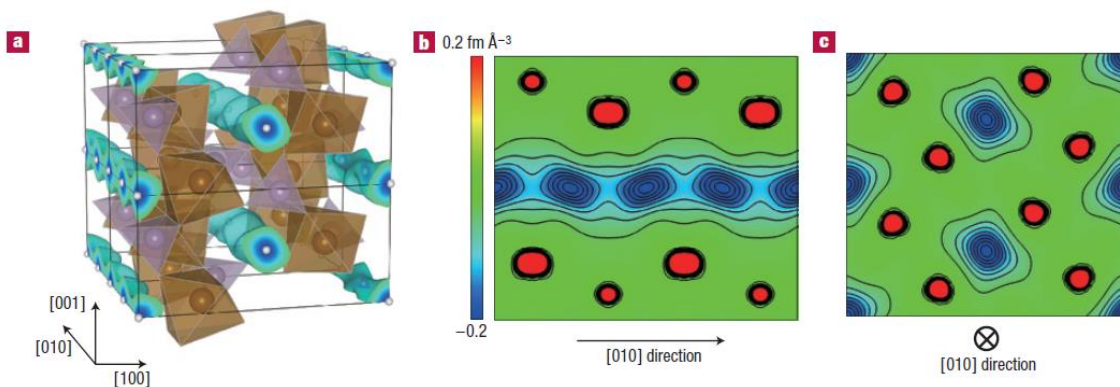


**Figure 2-2 | Visualization of lithium diffusion in  $\text{Li}_x\text{FePO}_4$ .** Reprinted by permission from Macmillan Publishers Ltd: [Nature Materials] (ref. 29), copyright (2008).

Let us begin from the most common electrode materials for LIBs. Electrochemical lithium intercalation is the fundamental knowledge for modern battery technology. Even intercalation itself has been known from 1920s, the concept of electrochemical intercalation was defined in 1972 (ref. 23) and a promising report of the electrochemical lithium insertion into layered  $\text{TiS}_2$  was given by Whittingham in 1976 (refs. 24, 25); researchers in the same field told that even specialists could not imagine  $\text{Li}^+$  can be electrochemically inserted into a robust inorganic compound at that time (See ref.13 for a detailed story). This is the dawn of rechargeable lithium batteries and also of solid-state ionics. Later discovery of  $\text{LiCoO}_2$  by J. B. Goodenough in 1980 boosted the lithium battery research.<sup>26</sup> The battery system using intercalation compounds in both anode and cathode is called rocking-chair system demonstrated by Murphy and then Scrosati Laboratory.<sup>27,28</sup> The energy storage mechanism of intercalation compounds can be described by host-guest chemistry. As a guest,  $\text{Li}^+$  is topotactically inserted

in the host compounds and diffuses in specific diffusion pathway associated with redox reaction (Figure 2-2).<sup>29</sup>

The diffusion pathway is a key nature of intercalation compounds to achieve a high power feature. In simple consideration,  $\text{Li}^+$  in two-dimensional (2D) pathway can reach faster diffusion coefficient than 1D one even for micro crystals. This can be supported from the research on  $\text{Li}_2\text{FeP}_2\text{O}_7$  and  $\text{LiFePO}_4$ .<sup>30,31</sup> The typical electrode having 1D diffusion pathway is olivine compounds such as  $\text{LiMPO}_4$  (M = transition metals).<sup>30</sup> The  $\text{LiFePO}_4$  attracts thousands of interests due to its superior cycle stability and proper energy density. However, there is still a lot of issues from point of basic science for these compounds, especially  $\text{Li}^+$  diffusion mechanisms. In fact, electrochemical insertion/de-insertion mechanism, the  $\text{LiFePO}_4$ 's phase change mechanism is still unclear, even  $\text{LiFePO}_4$ -based LIBs are already commercialized.<sup>32-35</sup>

Layered oxide compounds, for example  $\text{LiMO}_2$  (typical M = Co and Ni),  $\text{LiNi}_{0.5}\text{Mn}_{0.5}\text{O}_2$ ,  $\text{LiNi}_{1/3}\text{Mn}_{1/3}\text{Co}_{1/3}\text{O}_2$  (NMC), and  $x\text{Li}_2\text{MnO}_3 \cdot (1-x)\text{LiMn}_{0.5}\text{Ni}_{0.5}\text{O}_2$  (Li-rich system), are one of the most promising candidates for intercalation-based cathode materials having 2D ion diffusion pathway.  $\text{LiNi}_{0.5}\text{Mn}_{0.5}\text{O}_2$  and NMC were synthesized by Ohzuku and his co-workers to improve the stability of  $\text{LiMO}_2$ .<sup>36-38</sup>  $\text{LiMO}_2$  has several crystal phase changes during Li insertion and extraction. Indeed, in case of M = Ni, stoichiometric  $\text{LiNiO}_2$  is difficult to synthesize due to instability of  $\text{Ni}^{3+}$ .  $\text{LiNi}_{0.5}\text{Mn}_{0.5}\text{O}_2$  has a stable cycle property because this compound is much closer to stoichiometry compared to  $\text{LiNiO}_2$  and only  $\text{Ni}^{2+}$  is oxidized during the Li extraction.<sup>36,37</sup> These features of  $\text{LiNi}_{0.5}\text{Mn}_{0.5}\text{O}_2$  are considered as the reasons for a stable cycling. Additionally this material has an acceptable specific capacity of  $\sim 150$  mAh/g (cut-off voltage = 2.5–4.3 V vs.  $\text{Li/Li}^+$ ). NMC has a high specific capacity of  $\sim 200$  mAh/g and a high thermal stability. NMC is considered as a promising practical cathode material because of its affordability compared to  $\text{LiCoO}_2$ .<sup>38</sup>

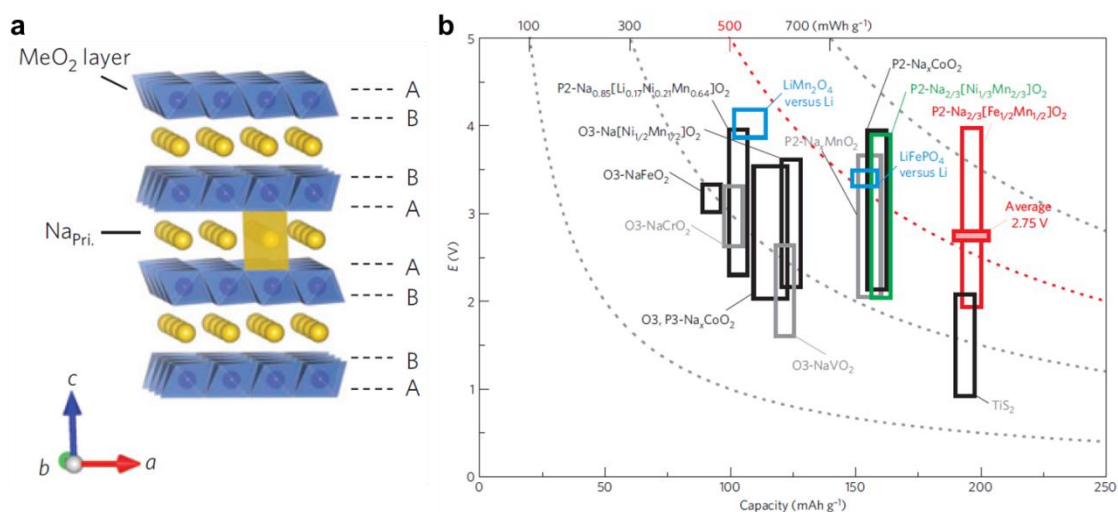


**Figure 2-3 | (a) Crystal structure of P2-Na<sub>2/3</sub>Fe<sub>0.5</sub>Mn<sub>0.5</sub>O<sub>2</sub> and (b) its electrochemical property compared to other materials.** Reprinted by permission from Macmillan Publishers Ltd: [Nature Materials] (ref. 45), copyright (2012).

The Li-rich system is not well understood its electrochemical mechanism.<sup>39–42</sup> Although this compound shows a high specific capacity of  $\sim 300$  mAh/g, unstable cycling due to complex crystal phase change during charge/discharge cycling and a capacity degradation due to oxygen extraction at the first cycle should be solved.

Even for the sodium battery systems, layered compounds are still promising candidates to be applied to. One of the oldest reports was also given by Whittingham and his co-workers in 1978 by using TiS<sub>2</sub>.<sup>43</sup> Thus, C. Delmas and his co-workers developed sodium batteries by using layered oxides.<sup>44</sup> The recent development was reported by Yabuuchi, Komaba, and their co-workers showing a great success by using P2-Na<sub>2/3</sub>Fe<sub>0.5</sub>Mn<sub>0.5</sub>O<sub>2</sub> which shows electrochemical properties comparable to developed cathode materials for LIBs (Fig. 2-3).<sup>45</sup> Significant benefit of P2-Na<sub>2/3</sub>Fe<sub>0.5</sub>Mn<sub>0.5</sub>O<sub>2</sub> are its high-performance and affordability: Na, Fe, Mn are all highly abundant.



Spinel oxide compounds, such as  $\text{LiMn}_2\text{O}_4$  (LMO)<sup>46</sup> and  $\text{Li}_4\text{Ti}_5\text{O}_{12}$  (ref. 47), are typical 3D Li diffusion materials. Since Mn is abundant compared to Co, researches on the LMO is active, however, due to the desolvation into electrolyte and Jahn-Teller effect of  $\text{Mn}^{3+}$  at discharged state causes capacity degradation. The substitution of Mn to Ni or Cr in LMO leads to a 5 V-class cathode.<sup>48</sup> For other compounds, there are Li-ion super ionic conductor (LISICON) type compounds for example  $\text{Li}_2\text{MSiO}_4$  (typical M = Fe, Mn, Co)<sup>49-51</sup> as well as Na-ion super ionic conductor (NASICON) type compounds.

Strategy to improve the electrochemical properties of intercalation compounds is limited because major features are decided by its crystal structure and a redox cation. Li diffusivity and a specific capacity are basically limited by its crystal structure. Redox potential is decided by each cation; a high redox potential is given by  $\text{Co}^{3+/4+}$  as a redox cation but it is a limited resource and toxic. One strategy is the use of inductive effect: by changing a component of polyanion and/or substitution of electronegative materials, such as F, an electronic structure of materials can be modified.<sup>52-54</sup> This strategy is powerful to develop the electrochemical properties of Fe-based intercalation compounds because  $\text{Fe}^{2+/3+}$  show a lower redox potential compared to other transition metals but much abundant.<sup>52</sup> Additional improvements of electrochemical properties are given by surface modification and nano-sizing of active materials, especially for achieving high-power electrodes. Indeed, understanding in two-phase reaction mechanism could help further development on high-power LIBs.<sup>34,35</sup>

## **2. 3. MATERIALS FOR CONVERSION REACTION**

**C**onversion reaction was found by Tarascon's group in 2001.<sup>55</sup> The mechanism can be described by following equation<sup>56,57</sup>:

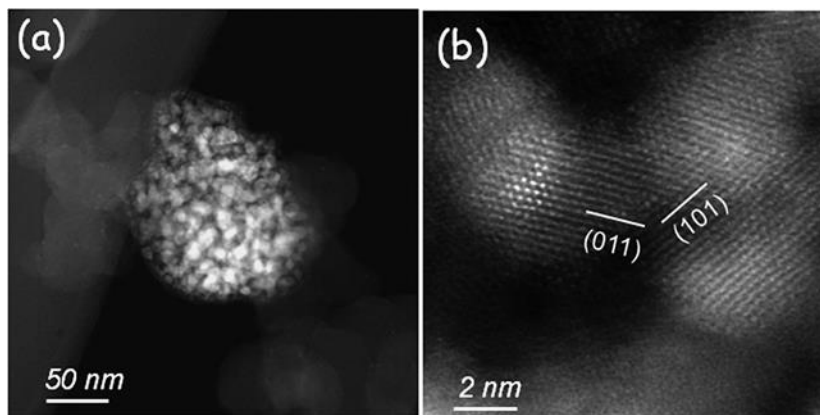
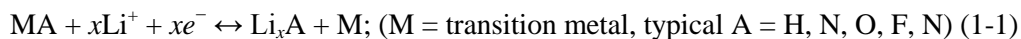


**Figure 2-4 | (a) Fe particles in LiF matrix obtained by fully lithiation of FeF<sub>3</sub>. and (b) Structural coherence at a high-magnification.** Reprinted by permission from ref. 57. Copyright (2012) American Chemical Society.

An electrochemical reduction of MX is driven by lithium incorporation and nano M<sup>0</sup> is formed in non-crystalline Li<sub>x</sub>A matrix (Fig. 2-4). By the oxidation from M<sup>0</sup> + Li<sub>x</sub>A state, MX will be formed again by giving a proper electromotive force. As the positive aspect, conversion reaction can produce high specific capacity because this reaction destroys the crystal structure and incorporate Li until transition metal becomes M<sup>0</sup> state from M<sup>x+</sup>. As the negative aspect, due to this destruction of crystal structure, a high volume expansion causes cracks of electrode and this leads to bad cycle performance. Moreover, a large hysteresis typically > 1 V during charge-discharge cycles is a problematic issue on the energy efficiency.

## 2. 4. ORGANIC MATERIALS FOR ENERGY STORAGE DEVICES

The first indication of the electronic conductivity of organic compounds was given by H. Akamatsu and his co-workers in Perylene-bromine complex in 1954.<sup>58</sup>

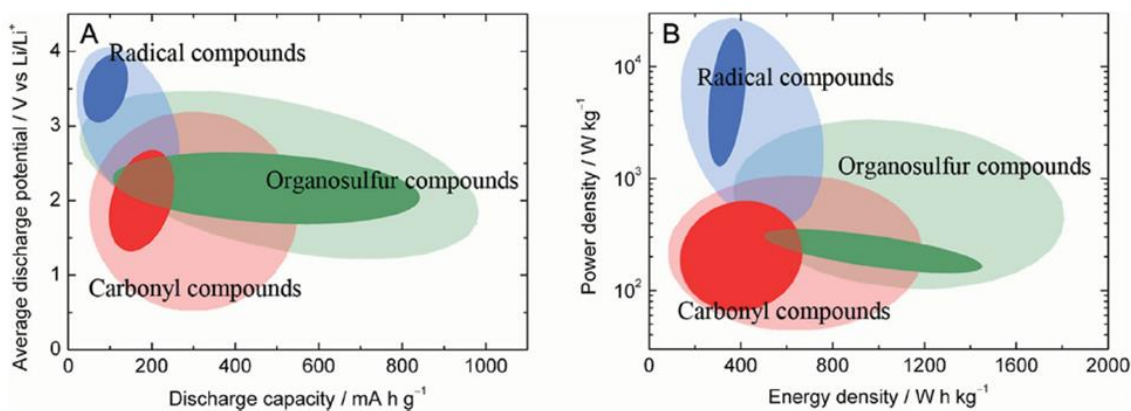


**Figure 2-5 | (a) Electrochemical properties of major organic compounds in discharge capacity vs. average discharge potential. (b) Ragone plot for main organic compounds.** Reprinted from ref. 62 by permission with Copyright © 2012 Wiley-VCH Verlag GmbH & Co. KGaA.

Later, further improvements were achieved by H. Shirakawa, A. G. MacDiarmid, A. J. Heeger and their co-workers in 1970s by using polyacetylene.<sup>59,60</sup> Ever since conductive organic compounds were discovered, they are still of great interests due to promising possibility to be used in a variety of sustainable and flexible electronic devices, such as photovoltaic cells and batteries. Indeed, the use of organic compounds could reduce the cost of products compared to that of current metal-based devices.

There are mainly three organic compounds for the battery use<sup>61,62</sup>: radical polymers, organosulfur compounds, and carbonyl compounds. Despite radical polymers show a high power density, they require a high amount of conductive additives due to a poor electronic conductivity. This disadvantage results in low specific capacities in full-cells. On the other hand organosulfur compounds can produce a high specific energy. However, due to the desolvation of polymer into electrolytes, the cycle property is poor. Compared to last two organic compounds, carbonyl compounds could be a practical compound group to be applied to batteries since both a relatively high energy density and a good cycle property exist. Organic

compounds have a promising potential to be utilized in energy storage devices as electrodes. However, further investigations on the materials are necessary, especially on the following problem; charge-transfer processes during electrochemical reaction on organic compounds have several questions which need to be solved.

## 2. 5. OTHER POSSIBLE MATERIALS FOR ENERGY STORAGE DEVICES

Even oxygen ( $O_2$ ) can be electrochemically lithiated and be de-lithiated at the theoretical electromotive force of  $\sim 3$  V vs.  $Li/Li^+$ .<sup>63,64</sup> This chemical reaction can produce a super-large theoretical energy density of Li- $O_2$  batteries (LOBs) with  $106,515$  Wh  $kg^{-1}$  ( $= 3$  V vs.  $Li/Li^+ \times 3,505$  mAh  $g^{-1}$  based on the mass of  $O_2$ ).<sup>15</sup> This high energy density brings LOBs as a battery which can be comparable to internal combustion engines (ICEs). However, a large polarization between charge-discharge cycles leads to poor energy efficiency. A problem regarding side reactions which are caused by decomposition of organic electrolytes due to radical oxygen species should also be solved.<sup>65,66</sup> Indeed, LOB systems require catalysts, typically precious metals.<sup>67,68</sup> This might be a crucial problem on the cost of LOBs analogue to fuel-cells.

Above problems are the reasons why Li-sulfur batteries (LSBs) are of great interests. The electrochemical redox reaction on lithium and sulfur (S) occurs at around 2 V vs.  $Li/Li^+$  with a large specific capacity of  $2,567$  mAh  $g^{-1}$  and it results in a theoretical specific energy density of  $5134$  Wh  $kg^{-1}$  based on the mass of sulfur.<sup>69-71</sup> LSBs cannot be compared to ICEs in terms of energy density, but this system neither require catalysts nor show a large polarization. Also, S is a very cost-effective material. These positive aspects of LSBs are expected to lead

LSBs as practical next-generation batteries. As one of the major problems of LSBs, the desolvation of polysulfides into electrolytes based on organic solvents can be pointed out. This causes the degradation of a specific capacity.<sup>71</sup> In spite of the existence of such problems in LSBs, it has been commercialized by Sion Power. These light elements can adopt not only  $\text{Li}^+$  but also other alkali species as charge carriers.

Energy storage materials, which use an exotic ion as a charge carrier, will be indicated. Recently, an energy storage system using oxygen ion ( $\text{O}^{2-}$ ) as a charge carrier, so-called oxygen rocking batteries, was reported. It has been already known in 1970s that some perovskite-type compounds have a good  $\text{O}^{2-}$  diffusivity.<sup>72</sup> This report showed that energy storage system based-on  $\text{O}^{2-}$  intercalation could be a promising candidate towards lithium-free rechargeable batteries.<sup>73</sup>

## **2. 6. SUMMARY FOR THE CHAPTER 2**

As various electrode materials were discussed, almost all compounds being able to apply to batteries have been already well known, especially for intercalation mechanism. One possibility to achieve high-performance and affordable batteries could be development of synthetic process for electrode materials. If we can succeed to establish a general cost-effective process to obtain already-known electrode materials having high electrochemical properties, this could be a contribution on the battery research. Making a design of novel electrode materials which does not depend on *Mother Nature* would be even more important. Since finding of intercalation materials and commercialization of LIBs, the researchers have been carried out in the “cage” of crystal structures existing in nature. The successful design of artificial crystalline

compounds could lead a giant leap on the further development on the electrical energy storage device.

# CHAPTER 3. ANALYTICAL TECHNIQUES

## 3. 1. REAGENTS

**Table 2-1-1** | Regents for Synthesis and Electrochemical measurements

Regent Name	Purity	Production Company
Sodium molybdenum oxide dihydrate ( $\text{Na}_2\text{MoO}_4 \cdot 2\text{H}_2\text{O}$ )	AR grade	Alfa Aesar
Molybdenum trioxide ( $\text{MoO}_3$ )	99.5 %	Alfa Aesar
Zinc Chloride ( $\text{ZnCl}_2$ )	98 %	ABCR
1,4-Dicyanobenzene (pDCB)	98 %	Aldrich
Tris(4-cyanophenyl)benzene (TCPB)	98 %	ABCR
Bis(trifluoromethane)sulfonimide lithium salt (LiTFSI)	99.95 %	Aldrich
Sulfur	99.5 %	Alfa Aesar
Super-P (conductive additive)		TIMCAL
Poly(tetrafluoroethylene) (PTFE)	98 %, 30 $\mu\text{m}$ particle size	Alfa Aesar
Sodium Carboxymethyl Cellulose (CMC)	99.5 % WALOCCEL CRT 2000 PA	Dow Chemicals
1M $\text{LiPF}_6$ in Ethylene Carbonate (EC):Dimethyl Carbonate (DMC) (1/1 w/w)	-	Kishida Chemical or Merck
1M $\text{NaClO}_4$ in Propylene Carbonate (PC)	-	Kishida Chemical

1M NaClO <sub>4</sub> in Ethylene Carbonate (EC):Diethyle Carbonate (DEC) (1/1 w/w)	-	Kishida Chemical
1,3-dioxolane	99 %	Aldrich
1,2-dimethoxyethane	99.5 %	Aldrich

---

## 3. 2. CHARACTERIZATION TECHNIQUES

### 3. 2. 1. X-Ray Diffraction (XRD) measurements<sup>74,75</sup>

**X**-Ray diffraction (XRD) is one of the most standard and powerful methods to characterize materials by using an electromagnetic wave with a wave length ranged from 0.5 to 10 Å, so-called X-ray. X-ray was found by Röntgen in 1895 and XRD in crystals was found by Laue in 1912. After a while, Bragg senior and junior succeeded in crystal structure analysis of NaCl by using XRD method. The basic physics in XRD is based on Thomson scattering (an elastic scattering) of X-ray.

When an electromagnetic wave is irradiated to an electron, a forced vibration of electron occurs, and then a secondary electromagnetic wave is generated as a coherent spherical wave. Let us consider a diffraction of X-ray in two electrons system which has  $s_0$  and  $s_1$  as the unit vector of the incident and scattered X-ray, respectively. There are electrons at the point O and R (position vector  $\mathbf{r}$ ), and scattered X-ray will be observed at enough far point P (Fig. 3-2-1). The Laue condition, which shows the geometrical condition to be in phase, is given by eq. 3-2-1.

$$(\mathbf{s}_1 - \mathbf{s}_0) \cdot \mathbf{r} = n\lambda, \quad n = \text{an integer} \quad (3-2-1)$$



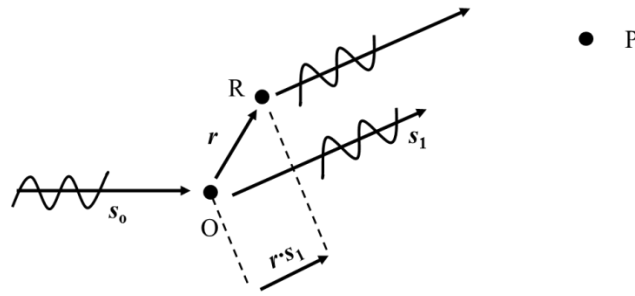


**Figure 3-2-1 | Schematic illustration of X-ray scattering in two electrons system.**

This condition is equal to the Bragg's law, which means eq. 3-2-1 just describes a diffraction condition.

To describe an X-ray scattering intensity  $I$  for a crystal, a factor which is related to  $I$  should be fixed because even if a condition for diffraction (eq. 3-2-1) is satisfied, Bragg diffraction cannot be achieved when structure factor is zero. By using Laue function  $G$  and structure factor  $F(\mathbf{k})$ ,  $I$  can be written as follows;

$$I = I_e G |F(\mathbf{k})|^2 \quad (3-2-2)$$

where,  $I_e$  and  $\mathbf{k}$  is a single electron scattering intensity and a scattering vector, respectively.

Laue function  $G$  shows information about strength and expanse of  $I$  in reciprocal lattice space.

Structure factor  $F(\mathbf{k})$  can be written

$$F(\mathbf{k}) = \int \rho(\mathbf{r}) \exp(2\pi i \mathbf{k} \cdot \mathbf{r}) dV \quad (3-2-3)$$

where,  $\rho(\mathbf{r})$  and  $dV$  is electron density and volume element, respectively.

### 3. 2. 2. Transmission Electron Microscopy (TEM)<sup>76</sup>

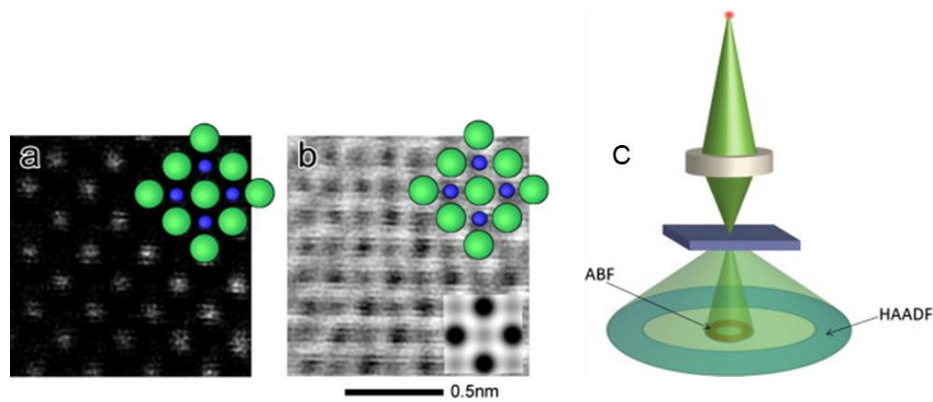


**Figure 3-2-2 | Features of the state-of-the-art TEM.** (a) The annular dark-field image of a crystal of VH<sub>2</sub> viewed along [0 0 1]. (b) The annular bright-field (ABF) image recorded simultaneously with (a). (c) A schematic illustration of ABF imaging technique in a scanning transmission electron microscope. The projected structure is superposed on all images. A simulated ABF image assuming a specimen thickness of 5 nm is superposed on (b). See the reference for further details on ABF mode. Reprinted from R. Huang & Y. Ikuhara *Curr. Opin. Sol. Stat. Mater. Sci.* **2012**, *16*, 31. Copyright (2012) with permission from Elsevier.

When accelerated electrons are irradiated to solid-states, interactions between atoms occur. There are two main physics due to these interactions, i.e. Thomson scattering (elastic scattering) and Compton scattering (inelastic scattering). For transmission electron microscopy (TEM), elastic scattered electrons are used for high-resolution transmission electron microscopy (HRTEM) mode, selected-area electron diffraction (SAED) mode, etc., and inelastic scattered electrons are used for, such as, electron energy-loss spectroscopy (EELS).

First of all, we will see a TEM's short history. E. Ruska and M. Knoll observed Mo mesh by using a cathode-ray oscilloscope equipped with solenoid in 1931. They also succeeded to invent field-type electron lenses. After moving to Siemens, Ruska improved TEM with B. von Borries. In 1939, they launched the first commercialized TEM having accelerating voltage of 100 kV, a maximum magnification of 20,000 and a resolution of 120 Å. Now, the

state-of-the-art TEM can observe light elements, even hydrogen atom which was believed that it is impossible to be investigated (Fig. 3-2-2).

The original aim of TEM's development was the improvement of resolution limit of light microscopes. The light microscope resolution limit is determined by the radius of diffraction aberration  $\delta_B$ :

$$\delta_B = 0.6 \cdot \lambda / n \cdot \sin \alpha \quad (3-2-4)$$

where  $n \cdot \sin \alpha$  and  $\lambda$  is aperture and wave length of light, respectively. The maximum value for aperture in light microscope can be ca. 1.4 and  $\lambda$  is submicron order. One way to further increase resolution can be achieved by using a light source having shorter  $\lambda$ . Here comes the idea to use electron wave because the electron's wave length can be controlled by acceleration voltage. If we have a certain value for the acceleration voltage of  $V$ ,  $\lambda$  can be determined by following equations:

$$E = \sqrt{m_0 c^4 + p^2 c^2} = m_0 c^2 + eV \quad (3-2-5)$$

$$\lambda = \hbar / p \quad (3-2-6)$$

where  $m_0$ ,  $p$ ,  $c$ ,  $\hbar$  is rest mass of electron, momentum, light speed, Planck constant, respectively.

From above two equations,  $\lambda$  can be described:

$$\lambda = \frac{\hbar}{c \sqrt{2m_0 e}} / \sqrt{V(1 + \frac{e}{2m_0 c^2} V)} \quad (3-2-7)$$

For instance, when  $V = 100 \text{ kV}$ ,  $\lambda = 0.038 \text{ \AA}$ .

The TEM can be operated in imaging and diffraction mode. An image with high-point resolution can be achieved by imaging mode resulting in maximum beam aperture due to the lowest illumination coherence. On the other hand, diffraction mode is operated with the highest illumination coherence to obtain a reduced beam aperture by over-focusing of electron beam. As the diffraction effect increases by using this mode, an electron diffraction image can be obtained.

The observation of ordering of atoms or unit cells in materials can be obtained by the HRTEM mode. In the HRTEM mode, the primary electron beam is either transmitted through or diffracted by the specimen. The transmitted and diffracted wave brings the information about atomic orientation. Because a diffracted wave is a Fourier transform of the periodic potential of the electrons, the back transform of the wave leads to an enlarged picture of the periodic potential, so-called phase-contrast imaging, which is drawn by the interference of waves. These images can be magnified by electron-optical system.

### 3. 2. 3. Scanning Electron Microscopy (SEM)

**S**canning Electron Microscopy (SEM) is a piece of equipment which can observe the material with a magnification range from 10 to 100000 by scanning scattered electrons and analyze the stoichiometry of materials. This equipment was also initiated by M. Knoll in 1935. After the great contribution of M. von Ardenne and V. A. Zworykin in 1940s, the SEM was developed under the supervision of C. W. Oatley in 1950s and was commercialized in 1965 by Cambridge Scientific Instruments.

There are two operation modes for SEM: (I) secondary electron mode and (II) back scattered electron mode. The main difference is the way to capture electrons by collector field.

The mode (I) captures the secondary electrons, which is a low-energy electron being created during the primary electron's energy loss. The mode (II) captures the back scattered electrons, which are elastic-diffracted primary electrons.

### 3. 2. 4. N<sub>2</sub> physisorption measurements<sup>77-79</sup>

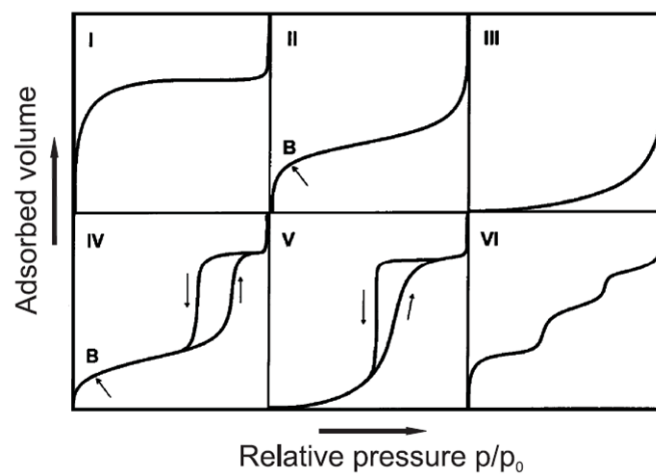


Figure 3-2-3 | Six main isotherms. Reprinted from ref. 78.

N<sub>2</sub> physisorption measurements are techniques to characterize porous solids. Adsorption and desorption using gases such as nitrogen, carbon dioxide, or krypton as adsorptive are applied. The use of physisorption has advantages such as fast and reversible reaction compared to chemisorption.

In general, total amount of gas is measured as a function of relative pressure ( $p/p_0$ ) with keeping temperature  $T$ . The amount of adsorbed molecules correlates with the surface area and porosity of materials. As the result, a curve, so-called physisorption isotherm, can be obtained. According to the IUPAC classification, there are six main types of physisorption isotherms (Fig. 3-2-3): (I) is typical isotherm for microporous materials. Once pores are filled, the isotherm shows a plateau which indicates a tiny external surface area; (II) is typical for

nonporous materials; (III) is also a typical isotherm for nonporous materials but they have weak gas-solid interactions; (IV) and (V) are isotherms for porous materials having a specific porous structure. The shape is involved with pore shape, uniformity, and interconnectivity. However, there is still ongoing discussions how to interpret each shape due to complex pore networks of mesoporous materials; (VI) is an isotherm for step-wise multilayer adsorptions on a nonporous materials.

There are several models to analyze a surface area from isotherms obtained by gas adsorption/desorption: The Brunauer-Emmett-Teller (BET) and Barret-Joyner-Halenda (BJH) model. The BET model shows a relationship in relative pressure  $p/p_0$ , adsorbed molecular  $n$  and the monolayer capacity  $n_m$ :

$$\frac{p/p_0}{n(1-p/p_0)} = \frac{1}{n_m C} + \frac{C-1}{n_m C} (p - p_0) \quad (3-2-8)$$

where  $C$  is correlated with the adsorption and condensation enthalpies.  $n_m$  and  $C$  can be derived from the ascending slope and the axis intercept, respectively. The specific surface area can be calculated from  $n_m$  by assuming an average area  $\sigma$  that each adsorbed molecule occupies on the surface.

The BJH model, which shows a gas condensation in pores before reaching its saturating pressure  $p_0$ , is based on the Kelvin equation, which describes the relationship between meniscus and a change in vapor pressure. The mathematical description of BJH mode can be given by the following equation with  $\gamma$ ,  $V_m$ ,  $r_p$ ,  $t$ , and  $R$  as surface tension, molar volume of a liquid, a pore radius, a thickness of physisorbed film and the universal gas constant, respectively:

$$r_p \left( \frac{p}{p_0} \right) = - \frac{2\gamma V_m}{RT \ln(p/p_0)} + t(p/p_0) \quad (3-2-9)$$

The total pore volume can be obtained by the amount of adsorbed gas at plateau region. However, there are few concerns on eq. 3-2-9 according to the validity of the equation for smaller pores, the exact relationship between a meniscus curvature and a pore size, and an assumed constance of the surface tension.

Indeed, use of density functional theory is important for correct investigations on micro and mesoporous materials. For above use, non-local density functional theory (NLDFFT) and quenched solid density functional theory (QSDFT) are standard methods (See following papers as references: Ravikovich *et al.*, *Langmuir* **2006**, *22*, 11171; Neimark *et al.*, *Carbon* **2009**, *47*, 1617.)

### 3. 2. 5. Fourier-transform infrared (FT-IR) and Raman spectroscopy measurements<sup>80</sup>

**B**oth FT-IR and Raman spectroscopy methods measure the interaction of light and molecular vibrations. The incident light will lose a specific energy, which is depended on each vibration type. The difference between FT-IR and Raman spectrometry can be found at the transition process of vibration states (Fig. 3-2-4): FT-IR spectroscopy observes direct transitions of vibration states by infrared absorption(Fig. 3-2-4a); Raman spectroscopy observes the transitions of vibration states processed tarnation at an excited electronic state by Raman scattering, which is an inelastic scattering (Fig. 3-2-4b).

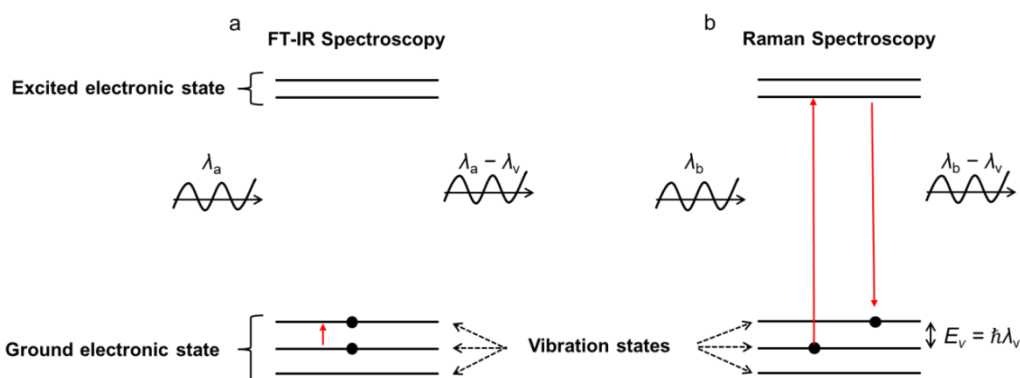


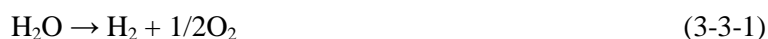
**Figure 3-2-4 | Schematic illustration for state transition type in (a) FT- IR and (b) Raman spectroscopy measurements.** Anti-Stokes process is not described here.

This is the reason to use infrared light ( $\lambda_a$  in Fig. 3-2-4a = 1–10  $\mu\text{m}$  order). These orders of lights are well suited with energy value for molecular vibration states. For Raman spectroscopy measurements, the transition goes an excited electronic state from a vibration state and back to the different vibration state, therefore, visible lights ( $\lambda_b$  in Fig. 3-2-4b = 100 nm order) are applied for Raman spectroscopy measurements. This difference comes to the selection of observable molecular vibration; infrared absorption is for the molecular vibration based on dipole moments and Raman scattering is for the molecular vibration based on polarizability. Indeed, Raman spectroscopy can measure dilute samples due to a strong intensity of Raman scattering originated from a resonance effect.

### 3. 3. ELECTROCHEMICAL MEASUREMENTS<sup>81–84</sup>

#### 3. 3. 1. Fundamental theory of electrochemical reaction

**E**lectrochemical reaction is an energy conversion process. For example, in ideal case, we need the applied voltage of  $\sim 1.23$  V for decomposition of water ( $\text{H}_2\text{O}$ ) to form oxygen ( $\text{O}_2$ ) and hydrogen ( $\text{H}_2$ ), i.e. eq. 3-3-1:





For eq. 3-3-1, we should give energy to process the reaction from left to right regarding of  $\Delta G^\circ = -237 \text{ k J/mol}$ . Thus, as the products,  $\text{O}_2$  and  $\text{H}_2$  can be generated from  $\text{H}_2\text{O}$  by applying a specific potential of  $\sim 1.23 \text{ V}$ , i.e.  $\text{H}_2\text{O} \xrightarrow{\Delta G} 2\text{H}^+ + 2e^- + 1/2\text{O}_2$ :  $\Delta G = \text{change of free energy for } \text{O}_2 = 237130 \text{ J/mol}$ ,  $1 F = 96485 \text{ C/mol}$ , energy (J) = potential (V)  $\times$  electric charge (C). From the last description, we can immediately find that the mechanism of electrochemical reactions is based on thermodynamics and statistical mechanics. After the dawn of electrochemistry by L. Galvani in 1791 and establishment of electrochemistry as science by M. Faraday by using Faraday's law in 1833, finding of the basic theory on electrochemistry using thermodynamics was established by H. L. F. von Helmholtz, J. W. Gibbs, and W. Nernst in the 19<sup>th</sup> century. Then, by contribution to statistical mechanics by, for instance, L. E. Boltzmann and H. A. Bethe, during the early 20<sup>th</sup> century, fundamental theory which is necessary to discuss electrochemical reaction was established.

Energy storage devices based on chemical reactions, so-called chemical batteries, are devices which can take energy to outside from spontaneous reactions divided into a couple of electrodes. Electromotive force (EMF) of a cell  $E$  can be described by Nernst equation by giving a Gibbs free energy  $\Delta G$

$$E = \frac{\Delta G}{nF} \quad (3-3-2)$$

Here,  $n$  is a number of electrons related to the reaction and  $F$  is Faraday constant. This  $E$  is called theoretical EMF or thermodynamic EMF because reactions in thermodynamic equilibrium state are hypothesized for this equation.

Kinetics in electrochemistry is important to discuss charge transfer reactions. Let us consider the reaction kinetics by using lithium deposition reaction



There are three processes for eq. 3-3-3, i.e. (I) diffusion of solvated lithium ion ( $\text{Li}^+$ ) to an electrode, (II) desolvation of molecules from  $\text{Li}^+$  at the near electrode (at electric double-layer) and following charge transfer (receiving electrons) at interface of electrode, and (III) diffusion in the solid-state (Fig. 3-3-1: this figure does not describe the lithium deposition process but lithium intercalation process).  $\text{Li}^+$  receives electrons around at outer Helmholtz plane (OHP). This charge transfer process has the main roll in reaction kinetics of electrodes.

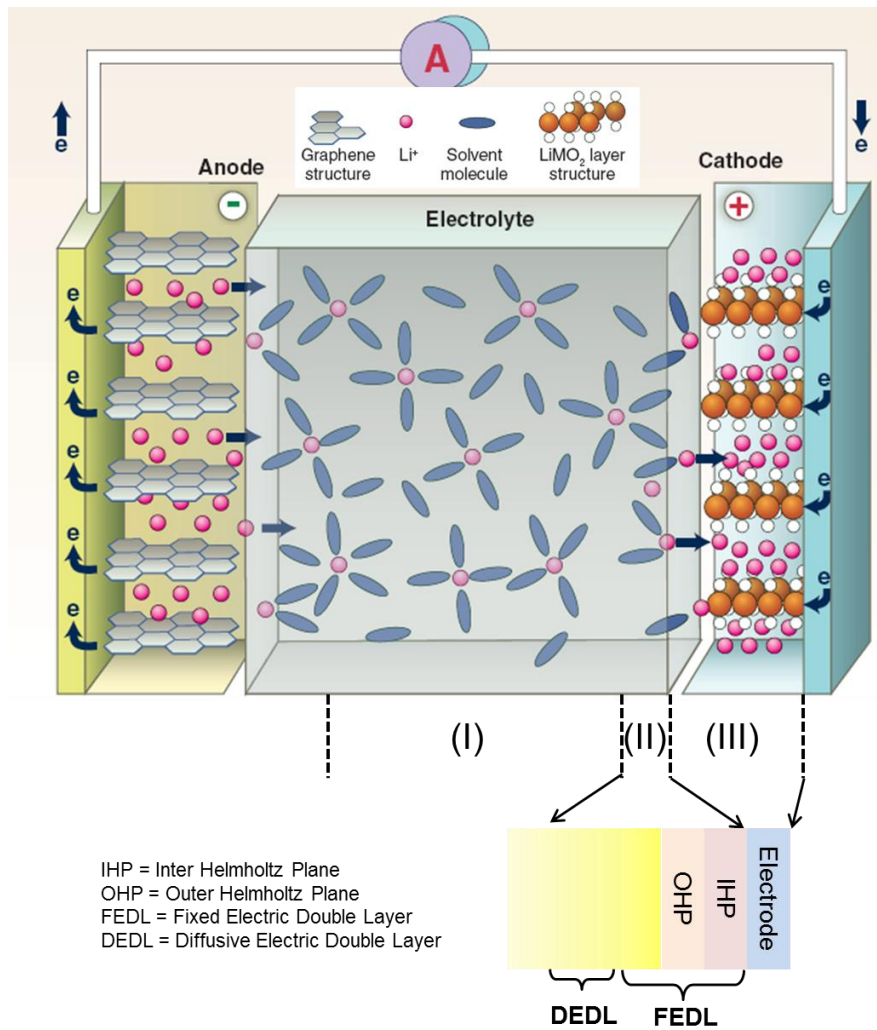


**Figure 3-3-1 | Schematic illustration for desolvation process of  $\text{Li}^+$ .** In this figure, intercalation of  $\text{Li}^+$  into a layered compound is described. Reprinted from ref. 12. with permission from AAAS. The author modified the original figure to describe the details on the electrode/electrolyte interface.

Reaction rate  $v$  ( $\text{mol/s cm}^2$ ) can be given by using current density  $i$

$$v = \frac{i}{F} \quad (3-3-4)$$

If we define  $i_a$  ( $> 0$ ) as the anodic current (oxidation process:  $\text{Li} \rightarrow \text{Li}^+ + e^-$ ) and  $i_c$  ( $< 0$ ) as the cathodic current (reduction process:  $\text{Li}^+ + e^- \rightarrow \text{Li}$ ), the total current  $i$  is

$$i = i_a + i_c = i_a + -|i_c| \quad (3-3-5)$$

We define the current density at the equilibrium state as  $i_{eq}$ , then, at this state,  $i_{eq} = i_a = |i_c|$ . During the lithium deposition process (eq. 3-3-3), there is a potential barrier, so-called activation energy  $u$ , in the reaction pathway. This activation energy takes a different value for the direction of reaction for eq. 3-3-3. We assume that the electrode is polarized  $\Delta\phi$  in negative direction from the equilibrium state, then, activation energy for cathodic reaction  $u_c$  and anodic reaction  $u_a$  can be written by using transfer coefficient  $\alpha$  and the initial activation energy  $u_0$  where the activation energy is 0 at  $\Delta\phi$ :

$$u_c = u_0 + \alpha F \Delta\phi \quad (3-3-6)$$

$$u_a = u_0 - (1 - \alpha) F \Delta\phi \quad (3-3-7)$$

We introduce the Arrhenius equation in this system. Here, we define that the rate constant for the cathodic reaction is  $k_c$  and for the anodic reaction is  $k_a$ :

$$k_c = A_c \exp\left(-\frac{u_c}{RT}\right) = k_c^0 \exp\left(-\frac{\alpha F \Delta\phi}{RT}\right), \text{ because of eq. 3-3-6 and } k_c^0 = A_c \exp\left(-\frac{u_0}{RT}\right) \quad (3-3-8)$$

$$k_a = A_a \exp\left(-\frac{u_a}{RT}\right) = k_a^0 \exp\left\{\frac{(1-\alpha) F \Delta\phi}{RT}\right\}, \text{ because of eq. 3-3-7 and } k_a^0 = A_a \exp\left(-\frac{u_0}{RT}\right) \quad (3-3-9)$$

The reaction rate  $v_c$  and  $v_a$  can be written as follows:  $v_c = k_c[\text{Li}^+]$  and  $v_a = k_a[\text{Li}]$ . If we give the electrode potential at equilibrium state as  $\Delta\phi_{eq}$ , the reaction rate for cathodic reaction and anodic reaction is equal

$$v_{\text{eq}} = v_c = v_a$$

$$\Leftrightarrow v_{\text{eq}} = k_c^0 \exp\left(-\frac{\alpha F \Delta \varphi_{\text{eq}}}{RT}\right) [\text{Li}^+] = k_a^0 \exp\left\{\frac{(1-\alpha) F \Delta \varphi_{\text{eq}}}{RT}\right\} [\text{Li}] \quad (3-3-10)$$

Because of eq. 3-3-8 and eq.3-3-9

We define the difference of potential between  $\Delta \varphi$  and  $\Delta \varphi_{\text{eq}}$  as  $\zeta$  ( $\because \zeta = \Delta \varphi - \Delta \varphi_{\text{eq}}$ ). From eq. 3-3-8, 3-3-9 and 3-3-10,  $|i_c|$  and  $i_a$  can be described

$$|i_c| = Fv_c = Fv_{\text{eq}} \exp\left(-\frac{\alpha F \zeta}{RT}\right) = i_{\text{eq}} \exp\left(-\frac{\alpha F \zeta}{RT}\right)$$

$$i_a = Fv_a = Fv_{\text{eq}} \exp\left\{\frac{(1-\alpha) F \zeta}{RT}\right\} = i_{\text{eq}} \exp\left\{\frac{(1-\alpha) F \zeta}{RT}\right\}$$

$$\text{therefore, } i = i_{\text{eq}} \left[ \exp\left\{\frac{(1-\alpha) F \zeta}{RT}\right\} - \exp\left(-\frac{\alpha F \zeta}{RT}\right) \right] \quad (\text{because of eq. 3-3-5})$$

$$(3-3-11)$$

The eq. 3-3-11 is called the Butler-Volmer equation. In case of  $\zeta \gg 0$ , eq. 3-3-11 becomes

$$i = i_{\text{eq}} \exp\left(\frac{(1-\alpha) F \zeta}{RT}\right) \quad (3-3-12)$$

Further modifications on eq. 3-3-12 lead to the Tafel equation (eq. 3-3-13)

eq. 3-3-12

$$\Leftrightarrow \zeta = \frac{RT}{(1-\alpha) F \zeta} \ln\left(\frac{i}{i_{\text{eq}}}\right)$$

$$\Leftrightarrow \zeta = \psi \ln i - \psi \ln i_{\text{eq}} \quad (\text{Here } \frac{RT}{(1-\alpha) F \zeta} = \psi) \quad (3-3-13)$$

These equations describe a relationship between an electrode potential and current density: Butler-Volmer equation shows the relation when concentrations of reaction species at the electrode surface and bulk electrolytes are equal; Tafel equation is a case of Butler-Volmer equation at higher electrode potential regions. However, cyclic voltammogram (CV) which actually shows potential (V) vs. current density ( $i$ ) does not follow both eq. 3-3-11 and eq. 3-3-13 because, in case of CV, current density is not only related to the charge transfer but also depends on mass transport such as diffusion of  $\text{Li}^+$  from bulk electrolyte to electrode. Therefore, eq. 3-3-11 and eq. 3-3-13 are applicable only if mass transport is fast enough.

As mentioned above, to describe CV, the effect of transportation of oxidant (Ox) or reductant (Red) from a bulk electrolyte to an electrode surface should be considered. Either cathodic or anodic current, we can describe this current  $i$  by the following equation by defining  $x$  as a distance from the electrode surface,  $n$  as the number of electrons related to the reaction, and  $D$  as a diffusion efficiency and  $C(x)$  as a concentration of Ox or Red species as a function of  $x$ :

$$i = nFD\left(\frac{\partial C(x)}{\partial x}\right)_{x=0} \quad (3-3-12)$$

By scanning a potential, for example in a negative direction, a reduction reaction of Ox occurs. As the potential is scanned a potential to the negative direction, cathodic current keeps on increasing and, at some point, shows a peak current then begins to decrease due to a low concentration of Ox at the surface of the electrode. After reaching to the peak current, the current is dominated by a diffusion-limited process.

### 3. 3. 2. Constant-current change-potential (CCCP) method

By giving or extracting electrons from redox active materials, redox reactions occur.

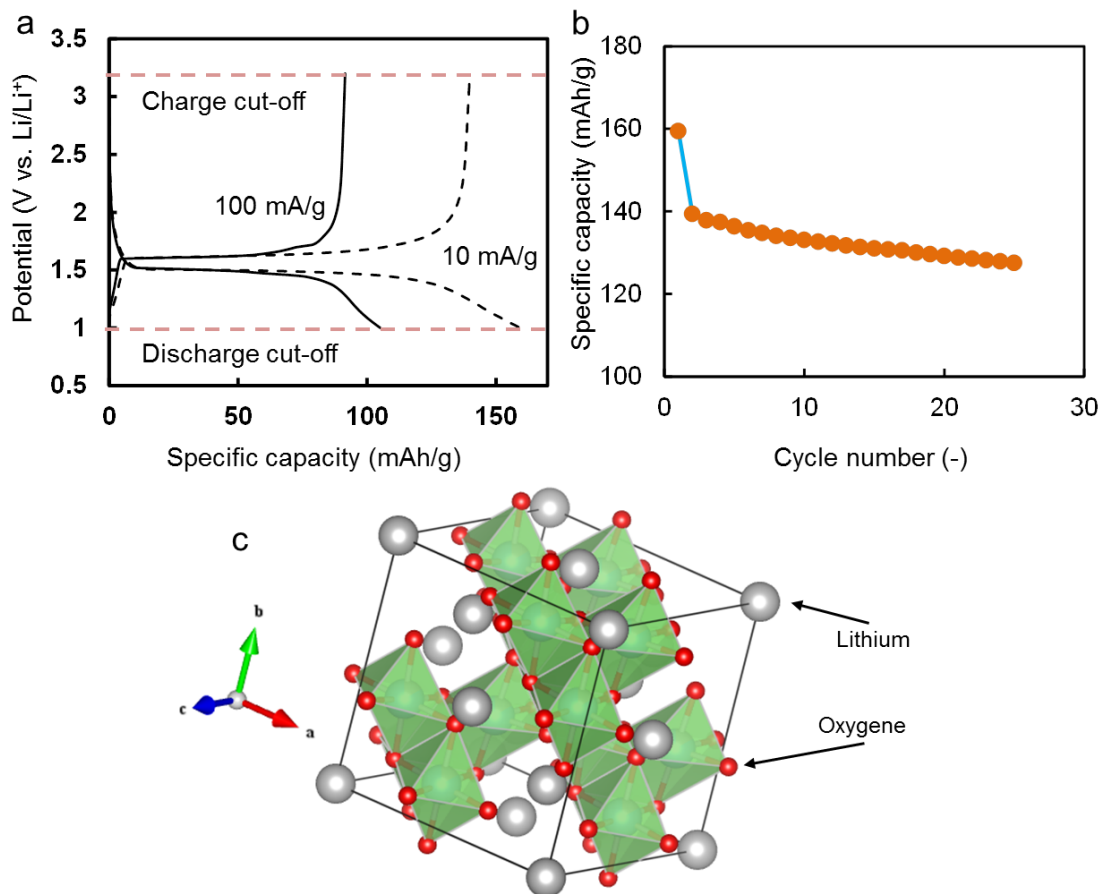


**Figure 3-3-2 | Example for CCCP method by using commercial  $\text{Li}_4\text{Ti}_5\text{O}_{12}$ .** (a) Charge-discharge curves in different current densities of 10 mA/g (dotted-line) and 100 mA/g (solid-line). (b) Cycle performance until 25<sup>th</sup> cycle. (c) Crystal structure of  $\text{Li}_4\text{Ti}_5\text{O}_{12}$ .

In principle, the CCCP method is used to investigate how many electrons are transferred or extracted from the redox active materials, how stable the materials are, and to recognize the kinetics of the redox reactions and related phenomena. One decides a current density, cycle number, and cut-off voltage, then can start experiments. Let us see the Fig. 3-3-2 showing an example of CCCP method by using  $\text{Li}_4\text{Ti}_5\text{O}_{12}$  (LTO) purchased from Aldrich. LTO

is a spinel type insertion compound showing a reversible  $\text{Li}^+$  insertion/de-insertion reaction at 1.55 V vs.  $\text{Li}/\text{Li}^+$ . In Fig. 3-3-2a, the first charge-discharge curves in different current densities are shown: solid-line and dotted-line was taken at a current density of 100 and 10 mA/g, respectively. A charge and discharge cut-off was fixed at 3.2 and 1.0 V vs.  $\text{Li}/\text{Li}^+$ , respectively. The spinel LTO has a theoretical specific capacity of 175 mAh/g. On the other hand, the commercial LTO showed less than 160 mAh/g. Indeed, by increasing the current density from 10 to 100 mA/g, the specific capacity decreased from 160 to 100 mAh/g. In general, 100 mA/g is not a high current density, however, the LTO showed an obvious decrease of the specific capacity. This is because, LTO is a poor electronic conductor, and thus, it is necessary to be synthesized in nanoscale and to be covered with conductive material to improve the electrochemical properties. Moreover, cycle performance in Fig. 3-3-2b is poor. The spinel LTO should be very stable even  $\text{Li}^+$  is inserted due to the zero-strain material even insertion of  $\text{Li}^+$ . Fig. 3-3-2b suggests that there are problems in materials.

### 3. 3. 3. Galvanostatic intermittent titration technique (GITT)

The determination of electrochemical reactions is one of the most important studies. Often, electrochemical reactions are obtained as the mixture of thermodynamic and kinetic reactions, thus, it makes difficult to discuss about equilibrium states. The GITT is a method to study a quasi-equilibrium state during electrochemical reactions. The original idea of GITT was introduced by R. A. Huggins and W. Weppner in 1977 to determine ion diffusion coefficients. The details of the theory can be found in their paper: *J. Electrochem. Soc.* **1977**, *124*, 1569.



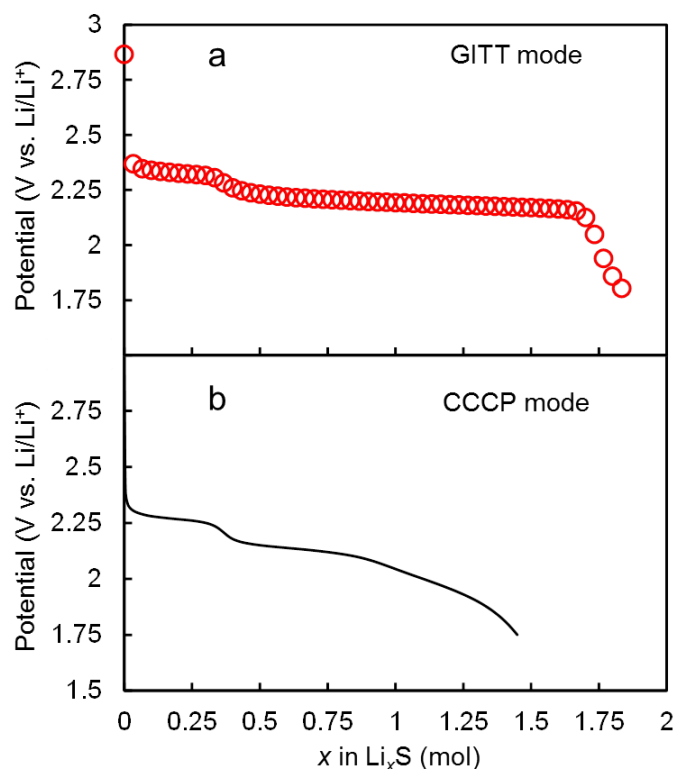


**Figure 3-3-3 | Example for GITT by using Li-S batteries.** (a) Discharge curve taken by GITT. (b) Discharge curve taken by CCCP method at a current density of 100 mA/g. The cathode is made by mixture of commercial S and porous carbon in the ratio of 1:1. Measurement conditions for both methods are same.

Fig. 3-3-3 shows a discharge curve taken by GITT (Fig. 3-3-3a) and CCCP method (Fig. 3-3-3b), respectively. The discharge curve taken by GITT (Fig. 3-3-3a) showed an ideal curve: The first plateau at around 2.4 V vs. Li/Li<sup>+</sup> is attributed to the conversion of solid sulfur to soluble polysulfides. The next plateau at around 2.1 V vs. Li/Li<sup>+</sup> suggests the conversion of polysulfides to solid Li<sub>x</sub>S. On the other hand, CCCP method (Fig. 3-3-3b) showed a sloping curve instead of a plateau at 2.1 V vs. Li/Li<sup>+</sup>. This is because of a polarization due to the insulating nature of S or side reactions, such as desolvation of polysulfides into electrolytes. Especially, main cause of polarization comes from kinetics electrochemical reaction. GITT can

suppress the negative effects of kinetics reactions to achieve an ideal charge-discharge curve on an electrode material.

### 3. 3. 5. Electrochemical impedance spectroscopy (EIS) analysis

**E**lectrochemical reaction is constituted of complex elemental processes. Even if we consider the simplest case, it would include three different processes: formation of electric double-layer, charge-transfer reaction, and mass transport. Electrochemical impedance spectroscopy (EIS) method enables to divide and analyze these complicated processes by introducing an idea of electric circuits into electrochemical reactions. The basic idea of AC impedance is that by applying a various range of frequency ( $f$ ), we can divide the integrated responses from charge-carrier due to change of the potential reversal velocity.

To describe electrochemical reactions, the Randles model (Fig. 3-3-4a) is often adopted as the equivalent circuit. In the Randles model in electrochemical reactions, it is constituted by an electrolyte resistance ( $R_s$ ), a capacitance element ( $C_{dl}$ ) as an electric double layer (EDL), charge-transfer resistance for the Faradaic reaction ( $\theta$ ) and the Warburg impedance ( $Z_w$ ), where is the field for reactions being mainly diffusion. There are two routes for ions: (1) charge on the surface of active materials as EDL or (2) getting into solid state through an electrochemical reaction. Therefore, from this point of view,  $C_{dl}$  and  $\theta$  are put as a parallel circuit. The diffusion of ions comes after charge transfer reaction; therefore, CPE comes after  $\theta$  as series. The Nyquist plot (Fig. 3-3-4b), which shows elements of complex reactions by using the Fourier transform. In the high frequency region, a semicircle will be shown in the Randles model due to the charge transfer and the capacitance due to the formation of EDL. This semicircle is often obtained with a crashed form because of the surface roughness and inhomogeneous sizes of active materials.

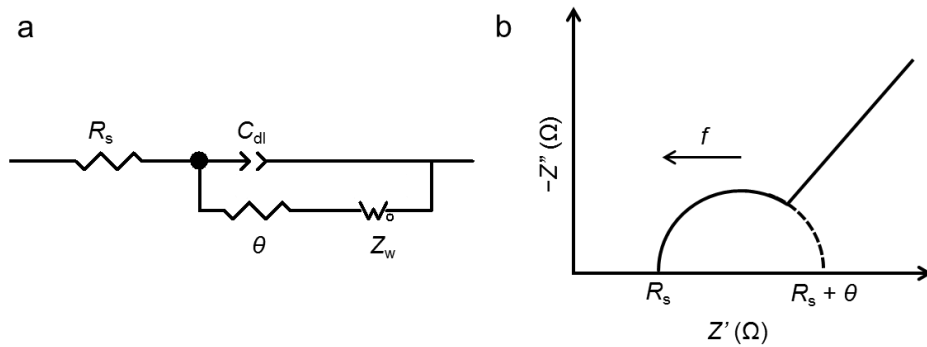


**Figure 3-3-4 | Example for EIS.** (a) the Randles model. (b) the Nyquist plot taken by the Randles model.

In the low frequency region, the transport of ions will be the limiting reaction, thus a linear part with the tilt angle of  $45^\circ$  will appear. The detailed theory and background of EIS can be found in following papers:

Ho *et al.*, *J. Electrochem. Soc.* **1980**, 127, 343.

Mizuno *et al.*, *Electrochim. Acta*, **2012**, 63,139.

# CHAPTER 4. SYNTHESIS OF NANOSTRUCTURED 1D $\text{MoO}_3$ AND ITS APPLICATION IN LITHIUM-ION BATTERIES

## 4. 1. INTRODUCTION

Following contents are based on the paper to be published in *Chemistry of Materials* (American Chemical Society) as “Aqueous Solution Process for the Synthesis and Assembly of nanostructured 1D  $\alpha$ - $\text{MoO}_3$  electrode materials”. A battery having both high-power and -energy is a highly demanded application.<sup>85,86</sup> As it is already discussed, electric conductivity, ionic diffusivity and specific capacity are robust natures of each electrode material. Therefore, a strategy for developing the electrochemical properties regarding materials characteristic properties is necessary. For example, in case of  $\text{LiFePO}_4$  (LFP), to overcome its electrically insulating feature, several procedures have been developed to achieve a high-power character.

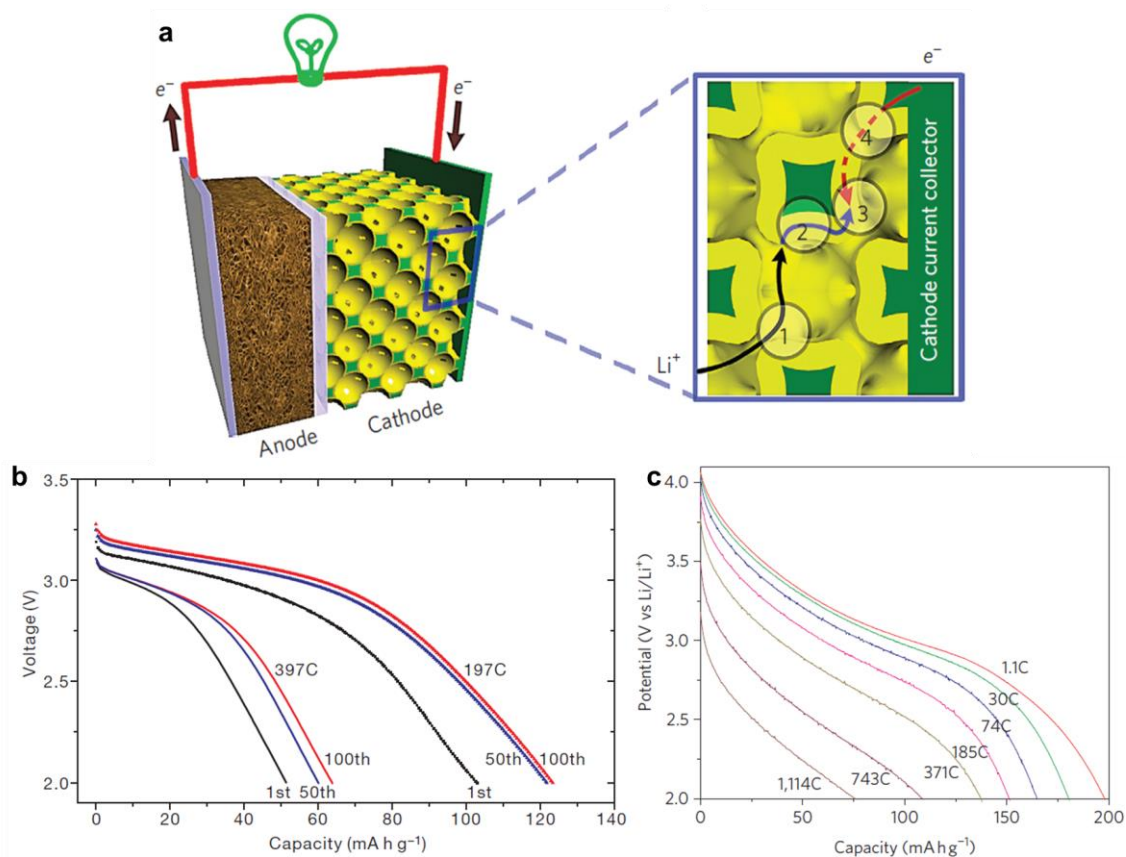


**Figure 4-1 | Ultra-high rate performances in cathodes for lithium-ion batteries. (a,b)  $MnO_2$  3D**

bicontinuous electrode showing a rate performance of over 1000C with a discharge specific capacity of 75 mAh/g. (c)  $LiFe_{0.9}P_{0.95}O_{4-\delta}$ :  $LiFePO_4$  covered with amorphous conducting layer, which shows  $\sim 400C$  with a discharge specific capacity of 60 mAh/g. (c) Reprinted by permission from Macmillan Publishers Ltd:

[Nature] (ref. 85) for Figure 4-1c copyright (2009); and [Nature Nanotechnology] (ref. 86), copyright (2011) for Figure 4-1a,b.

One of the most common strategies to improve electronic conductivity is coating of by conductive layers.<sup>85</sup> Another is nanosizing: a short ionic diffusion time can be obtained by shortening a diffusion length.<sup>84,87</sup> The 3D porous electrodes are also based on these strategies<sup>86</sup>: uniform, continuous porous electrode combined with conductive materials can ensure an optimized transport of electrons and electrolytes (Fig. 4-1a,b). Also, by combining these two methods, even for an insulating material, ultra-high rate performance was achieved (Fig. 4-1c).

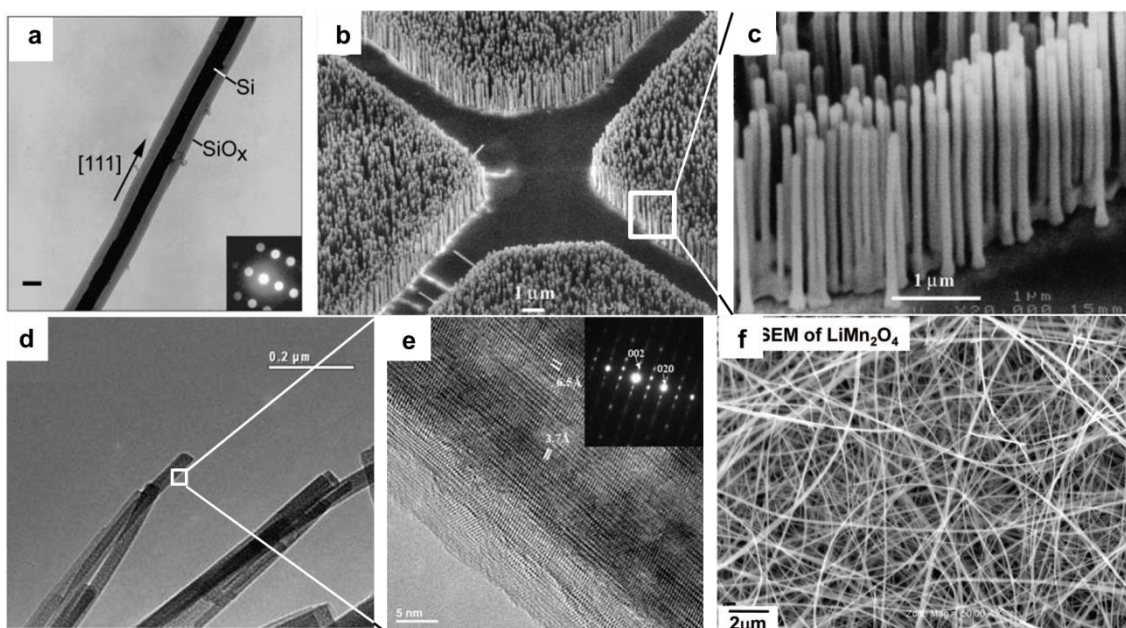


**Figure 4-2 | Various of 1D materials.** (a) Si nanowire. The scale bar shows 10 nm. (b,c) ZnO nanowires for Laser applications. (d,e) TiO<sub>2</sub>(B) nanowire for high-power cathode. (f) Ultra-long LiMn<sub>2</sub>O<sub>4</sub> nanowire for high-power cathode. Reprinted from ref. 88 and 89 for Figure 4-2a-c with permission from AAAS. Reprinted from ref. 90 by permission with Copyright © 2008 Wiley-VCH Verlag GmbH & Co. KGaA, Weinheim for Figure 4-2d,e. Reprinted with permission for ref. 91 for Figure 4-2f. Copyright (2009) American Chemical Society.

However, since these methods require too complex processes, they are often unrealistic methods. It can be mention for covering process of conductive layers on the surface of active materials and fabrication of 3D porous structures which are promising methods to improve electrochemical properties. They are too complicated processes to be applied in industrial field for mass production. Therefore, a simple crystal growth strategy to control nanostructures in appropriate morphology could be a realistic way to synthesize, and indeed, to assemble electrode materials for LIBs. Here, in this chapter, an aqueous solution process to synthesize a 1D electrode material and to assemble it in macroscopic freestanding paper is proposed.

The recent successful preparation of one-dimensional (1D) nanomaterials shows the great improvement of properties that is difficult to achieve in bulk materials (Fig. 4-2).<sup>88-91</sup>

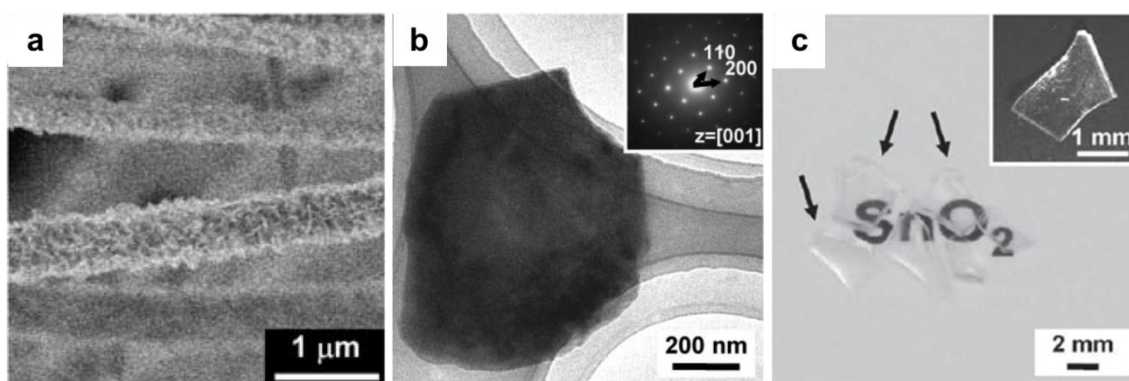


**Figure 4-3 | Several nanostructured oxides from aqueous solution process.** (a) Hierarchical nanostructured (1D + 2D) tin monoxide (SnO). (b) Single crystalline 2D SnO. (c) Tin dioxide (SnO<sub>2</sub>) superstructure constituted of 0D SnO<sub>2</sub> with ~2nm of diameter. Reprinted from ref. 118 for Figure 4-3a by the author of the paper. Reproduced by permission of The Royal Society of Chemistry. Reprinted from refs. 119 and 121 by permission with Copyright © 2010 Wiley-VCH Verlag GmbH & Co. KGaA, Weinheim for Figure 4-3b,c.

1D materials have shown already their promising properties in numerous applications, such as lasers<sup>88</sup>, photovoltaics<sup>89</sup> and energy storage devices.<sup>90–91</sup> From the perspective of application, another challenge is to assemble these functional nanomaterials in macroscopic scales. Assembly techniques of 1D material attract much interest because of their promising potential in electronic, optical, and energy storage devices mentioned above. A few interface-assembly method<sup>92–94</sup>, Langmuir-Blodgett approach<sup>95–97</sup> and oil-water-air interface self-assembly process<sup>98</sup>, have been proposed for the self-assembly of 1D materials, however, they require assistance of organic compounds and control of thickness is a challenge. The existence of organic compounds in assembled films sometimes causes the negative effect, if we consider their application of them to electronic and optical devices. Moreover, a self-assemble process for 1D oxides without the assistance of organic compounds is a still challenging issue. In this report, a spontaneous and facile assembly route is described for 1D  $\alpha$ -molybdenum trioxide (MoO<sub>3</sub>) through the evaporation of water as the dispersion medium without any organic compounds to form a large-scale freestanding film. In previous reports, MoO<sub>3</sub> has been

synthesized in a wide variety of nanostructures<sup>99–101</sup> and these nanomaterials have been applied in a variety of devices, such as photovoltaic<sup>102,103</sup> and batteries<sup>104–106</sup>. Especially, MoO<sub>3</sub> can be used as both an anode and a cathode for lithium-ion batteries (LIBs). LIBs are of great interests because they are expected to be a green technology to achieve a sustainable society.<sup>1–3</sup> For example, LIBs are applied to electronic vehicles and smart grid which is an electricity supply network combined with renewable energy. The current challenge in LIBs is how to increase the energy density of cells. From this point of view, MoO<sub>3</sub> has promising characters: it can provide theoretical specific capacity of ~1100 mAh g<sup>-1</sup> as an anode<sup>106</sup> by conversion reaction<sup>55</sup> and a theoretical specific energy of ~750 Wh kg<sup>-1</sup> (= 300 mAh g<sup>-1</sup> × 2.5 V vs. Li/Li<sup>+</sup>)<sup>104,107</sup> by intercalation mechanism<sup>24,25</sup>. These electrochemical properties of MoO<sub>3</sub> are attractive compared to graphite (372 mAh g<sup>-1</sup>)<sup>108</sup> and LiFePO<sub>4</sub> (~600 Wh kg<sup>-1</sup>)<sup>30</sup>, representing anode and cathode used in commercialized LIBs, respectively. Nanostructure is an important factor to obtain high-performance electrochemical properties<sup>109,110</sup>, and moreover some electrochemical properties can be only obtained from nano-electrode materials<sup>55</sup>. Hence, the integration of nanostructured MoO<sub>3</sub> synthesis by eco-efficient process and spontaneous self-assembly of nanostructured MoO<sub>3</sub> could lead to further development of indispensable devices in a facile and cost-effective way. Previous studies on the synthesis of MoO<sub>3</sub> from solution phase suggest that this material is a practically suitable candidate for growing 1D morphology due to its anisotropic crystal growth.<sup>99,101</sup> Here, we have synthesized 1D MoO<sub>3</sub> through a low-temperature aqueous solution route by one-step. We tested this 1D MoO<sub>3</sub> as a cathode material with high rate capability, which was originated by successful nanostructure control. And we fabricated oxide papers which are macroscopic, freestanding films consisting 1D MoO<sub>3</sub>. The low-temperature (< 373 K) aqueous solution route is a promising route to synthesize metal oxides and to control their nanostructures under an eco-efficient condition.<sup>111–123</sup> This route is



based on the precise control of the driving force for the crystal growth by manipulating the supersaturated state of a liquid phase.<sup>112,115,117</sup> Successful results in control of nanostructures and oxidation states of metal oxides through the aqueous solution route led to the next challenge to assemble these synthesized nanomaterials in specific morphology, such as ordered, macroscopic freestanding-film. Indeed, this method can apply for a formation of a composite paper made from metal oxide and carbon materials and we tested this composite paper as an anode for LIBs as an example of applications.

## 4. 2. EXPERIMENT

### 4.2.1. Aqueous solution synthesis of nanostructured 1D MoO<sub>3</sub> and oxide papers

The stock solution containing 0.05 M of sodium molybdenum oxide dihydrate (Na<sub>2</sub>MoO<sub>4</sub>·2H<sub>2</sub>O) was prepared with 100 dm<sup>3</sup> of purified water in polypropylene bottles. After the adjustment of pH to 0.5 by HNO<sub>3</sub> and following stirring for 1 hour, the sample bottles were maintained at 75 °C for 24 hours. The resultant materials were rinsed with purified water. In this condition, we can achieve ~0.25 g of dried 1D MoO<sub>3</sub> powder. In case of the fabrication of oxide papers, 30 ml of purified water was mixed with rinsed 1D MoO<sub>3</sub> (with acetylene black to fabricate the oxide/carbon composite papers) to form the suspensions. The suspensions were casted on an aluminum foil and dried at 75 °C in air to obtain the oxide paper.

Characterizations were carried out by using following procedures: The crystal phases of resulting materials were identified by using an X-ray diffractometer (PANalytical X'Pert PRO with Co-Kα<sub>1</sub> radiation). The morphologies of the resultant materials were observed by using a Field-emission scanning electron microscopy (FE-SEM; Zeiss LEO1530 Gemini

operated at 5.0 kV) and a field-emission scanning electron microscopy (FE-TEM; FEI Tecnai F30 operated at 300 kV). Crystal structures were drawn by using VESTA.

#### 4.2.2. Electrochemical measurements for nanostructured MoO<sub>3</sub>

The cell assembly was carried out in a glove box under argon atmosphere and tested on a multichannel potentiostatic-galvanostatic system VMP3 (Biologic). The electrochemical measurements were carried out using Swagelok type cells. We used lithium metal as an anode and 1M LiPF<sub>6</sub> in ethylene carbonate:dimethyl carbonate (1:1) as an electrolyte. The charge-discharge performance for cathodes, the electrodes were made by the 1D MoO<sub>3</sub> (50 wt.%), carbon black (Super-P; 45 wt.%) and binder (PTFE; 5 wt.%), was measured at current density of 1.0, 5.0, 10 and 20 A g<sup>-1</sup> in the potential range of 1.5–3.2 V versus Li/Li<sup>+</sup>. The charge-discharge performance for anodes (= the composite oxide papers), which were made by the 1D MoO<sub>3</sub> (80 wt.%) and Super-P (20 wt.%), was measured at current density of 0.1 A g<sup>-1</sup> in the potential range of 0.05–3.2 V versus Li/Li<sup>+</sup>.

## 4. 3. RESULTS AND DISCUSSION

#### 4.3.1. Synthesis of nanostructured MoO<sub>3</sub>

The 1D MoO<sub>3</sub> (Fig. 4-4) can be formed from a precursor aqueous solution containing 0.05 M sodium molybdenum oxide dihydrate (Na<sub>2</sub>MoO<sub>4</sub>·2H<sub>2</sub>O) with pH of 0.5 by maintaining 24 hours in 75 °C (See experimental section). The formation of MoO<sub>3</sub> in acidic solution can be described by following reaction:  $\text{MoO}_4^{2-} + 2\text{H}^+ \rightarrow \text{MoO}_3\downarrow + \text{H}_2\text{O}$  (4-1)

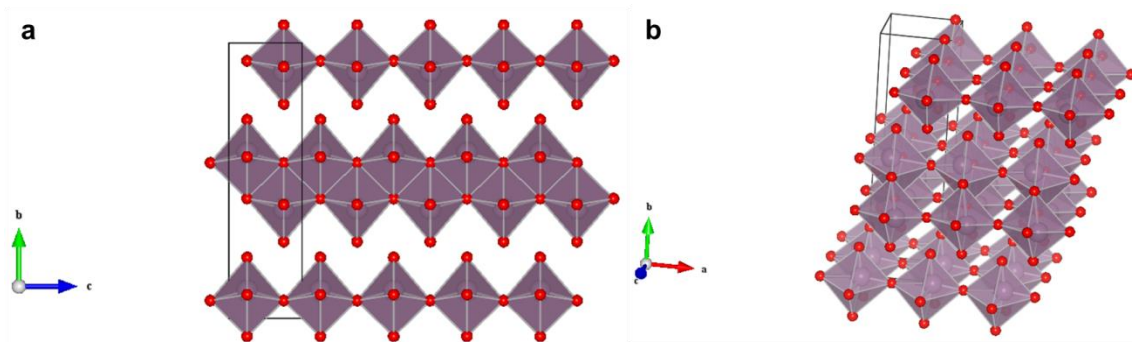


Figure 4-4 | Crystal structure of MoO<sub>3</sub> from different point of view.

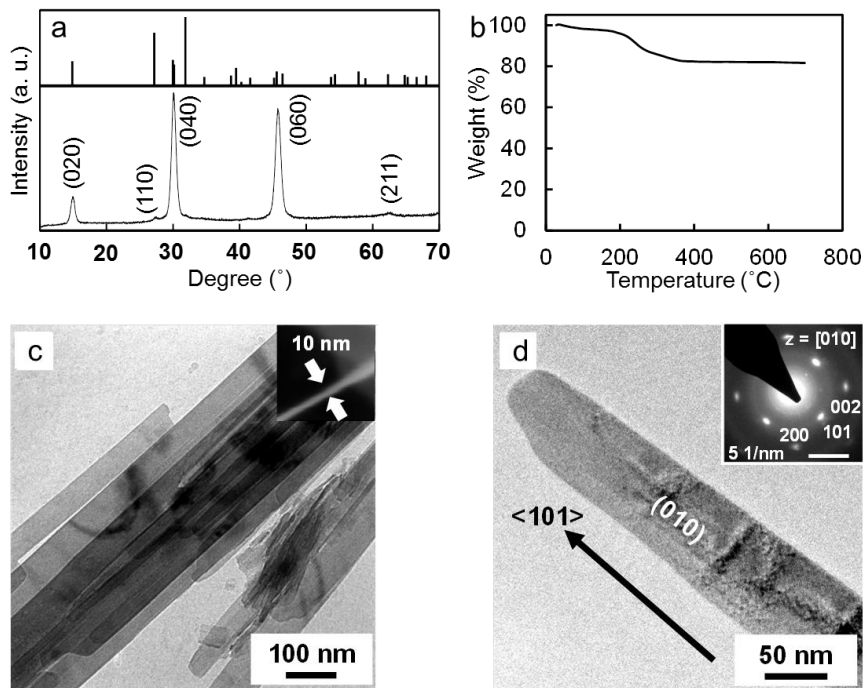
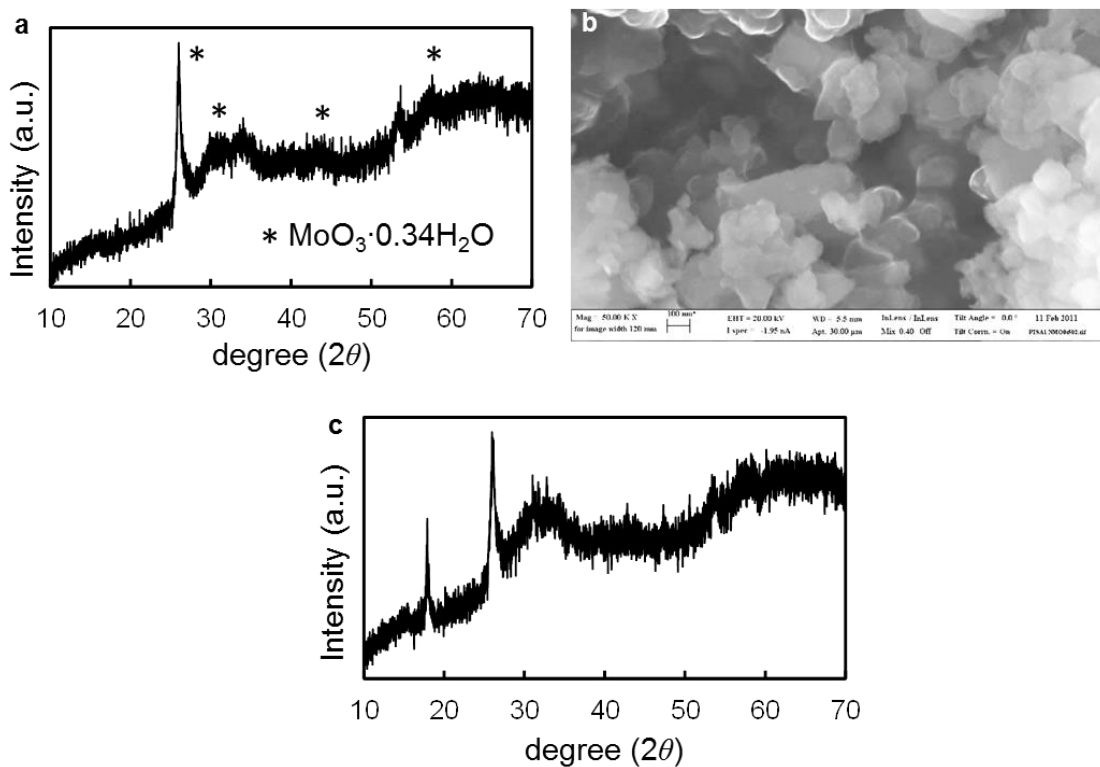


Figure 4-5 | Characterizations of 1D MoO<sub>3</sub>. (a) XRD pattern of the resultant materials. The reference indicates the pattern of ICDD 00-035-0609. (b) TG curve for 1D MoO<sub>3</sub>. (c) FETEM image showing 1D MoO<sub>3</sub>. Inset shows the thickness of 1D MoO<sub>3</sub> by FESEM image. (d) FETEM image with SAED pattern (inset). a. u. means arbitrary unit.

The powder X-ray diffraction (XRD) pattern of the dried resulting precipitate (Fig. 4-5a) confirms the formation of MoO<sub>3</sub> (The crystal system is Orthorhombic; The space group is *Pnma*; The lattice parameters are:  $a = 3.963 \text{ \AA}$ ,  $b = 13.855 \text{ \AA}$ ,  $c = 3.696 \text{ \AA}$ ; ICDD 00-035-0609). The intensified peaks from (010) plane on the powder XRD pattern suggest that the obtained

material has an anisotropic morphology with the (010) face which is preferentially arranged parallel to the sample holder. The thermogravimetry (TG) curve of 1D MoO<sub>3</sub> (Fig. 4-5b) indicates the existence of water molecules and molybdenum oxide hydrates. Field-emission scanning electron microscopy (FE-SEM) and high-resolution transmission electron microscopy (HR-TEM) images (Fig. 4-5c,d) show fibers 50–100 nm in width, with length in micro scale, and with thickness in ~10 nm (Fig. 4-5c inset). The selected area electron diffraction spots the (SAED) pattern for a single 1D MoO<sub>3</sub> (Fig. 4-5d inset) shows the spot patterns including the diffraction spots the {100}, {101}, and {001} planes. From this SAED pattern, the zone axis can be assigned to the [010] direction. These results suggest that the MoO<sub>3</sub> is elongated in the <101> direction (Fig. 4-5d). By changing the Mo(VI) concentration in the precursor solutions, we can estimate the formation process of 1D MoO<sub>3</sub> because a change of cation concentration in a solution could mean a change of supersaturated state, which is a driving force of nucleation and crystal growth.<sup>112,115,117</sup> In case of the Mo(VI) concentration of 0.5 M, we obtained the low-crystalline compounds which might be a mixture of hydrate molybdenum oxides (Fig. 4-6a,b). Even in the case of the lower concentration of 0.1 M, we also obtained the poor crystalline compounds (Fig. 4-6c in the supporting information). These results suggest that a high Mo(VI) concentration leads a high driving force for nucleation, thus it leads the promotion of large quantity of nuclei in the solution phase and forms amorphous-like nanocrystalline compounds (4-6b).<sup>115</sup> Therefore, in further lower Mo(VI) concentration of 0.05 M, we can obtain MoO<sub>3</sub> nanocrystals in specific morphology due to a proper driving force for nucleation and the crystal growth. MoO<sub>3</sub> nanocrystals have been often obtained in 1D morphology elongated in <100> or <001>.<sup>99–101</sup> This fact indicates us that the (100) and (001) faces of MoO<sub>3</sub> crystals have the faster growth rate compared to the (010) face.



**Figure 4-6** | (a) XRD pattern of resultant materials at 0.5 M of  $\text{Na}_2\text{MoO}_4 \cdot 2\text{H}_2\text{O}$ . \* indicates the patterns from  $\text{MoO}_3 \cdot 0.34\text{H}_2\text{O}$ . (b) FESEM image of resultant materials at 0.5 M of  $\text{Na}_2\text{MoO}_4 \cdot 2\text{H}_2\text{O}$ . (c) XRD pattern of resultant materials at 0.1M of  $\text{Na}_2\text{MoO}_4 \cdot 2\text{H}_2\text{O}$ .

Therefore, an anisotropic growth of  $\text{MoO}_3$  nanocrystals could occur at the (101) face due to the instability of the growing surface under the diffusion-controlled condition.<sup>120</sup>

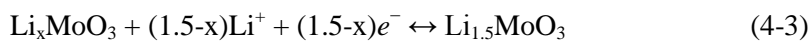
#### 4.3.2. Electrochemical properties of 1D $\text{MoO}_3$

We tested our as-prepared 1D  $\text{MoO}_3$  as a cathode material for LIBs and analyzed its electrochemical properties. Typically, high-performance electrochemical properties require high crystallinity of electrode materials to form less grain boundaries and a single crystalline feature, thus often, high-temperature synthesis routes are applied to obtain better electrode materials. However, recent reports on solution processes have shown that high-performance functional

oxides can be synthesized through these eco-efficient processes, even in less than 30 °C.<sup>121-123</sup> Here, we show the electrochemical properties of MoO<sub>3</sub> as a cathode material. The energy storage process of MoO<sub>3</sub> is based on the intercalation mechanism. It is quite important to control crystallinity and nanostructures of intercalation-based electrodes due to following two reasons: 1) Li<sup>+</sup> travels through along with specific ion channels in solid states, therefore, single crystalline electrode has an advantage for a smooth Li<sup>+</sup> diffusion due to less grain boundary<sup>91,110</sup>, thus this advantage can support to improve the cycle performance; 2) a nanosized electrode can show the high rate capability due to shorter Li<sup>+</sup> diffusion length.<sup>87</sup> From these points of view, improved electrochemical properties of 1D MoO<sub>3</sub> (Fig. 4-7a-d) compared to those of bulk MoO<sub>3</sub> also confirm the well crystalline and the successful control of nanostructure. The first charge-discharge cycle for 1D MoO<sub>3</sub> at a low current density of 0.1 A g<sup>-1</sup> is shown in Fig. 4-7a. The first discharge cycle in the potential range up to 1.5 V vs. Li/Li<sup>+</sup> can be ascribed to the reaction as:



After the first discharge, the electrochemical reaction from the second discharge can be described to:



These two reactions can be described as the insertion of Li<sup>+</sup> into the layered structure of MoO<sub>3</sub> (eq. (4-2) and (4-3)).<sup>104,105</sup> It is suggested that some amount of Li<sup>+</sup> form a new phase of Li<sub>x</sub>MoO<sub>3</sub> in the host material (x = ~0.25).<sup>124</sup>

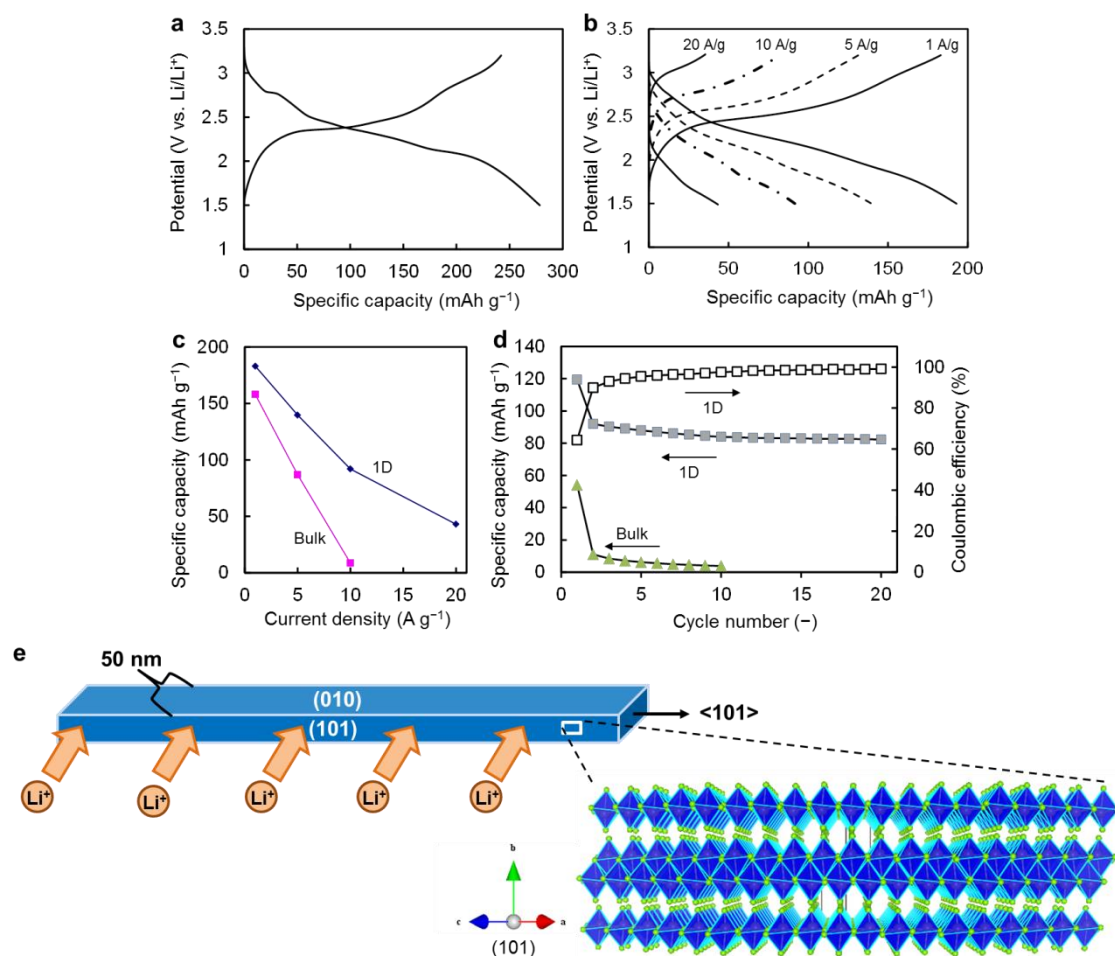


**Figure 4-7 | Electrochemical properties of 1D MoO<sub>3</sub> electrode.** (a) First charge-discharge curves of 1D MoO<sub>3</sub> electrode at a current density of 0.1 A g<sup>-1</sup>. (b) Charge-discharge curves of 1D MoO<sub>3</sub> electrode at a various current densities up to 20 A g<sup>-1</sup>. (c) Rate capability of 1D and bulk MoO<sub>3</sub> electrode. (d) Cycle performance and Coulombic efficiency of 1D MoO<sub>3</sub> electrode at high current density of 20 A g<sup>-1</sup>. (e) Schematic illustration for the short Li diffusion path of 1D MoO<sub>3</sub>.

Thus, there is the irreversible specific capacity of ~30 mAh g<sup>-1</sup> at first specific charge capacity compared to the first specific discharge capacity (Fig. 4-7a). In Fig. 4-7b and c, we show the rate capability of 1D MoO<sub>3</sub>. At a high current density of 20 A g<sup>-1</sup>, 1D MoO<sub>3</sub> shows the specific discharge capacity of ~50 mA g<sup>-1</sup>, however, the bulk micro crystalline MoO<sub>3</sub> (Alfa Aesar) cannot work as an electrode at the same condition.

Even in a harsh condition, the 1D MoO<sub>3</sub> exhibited a stable cycle property (Fig. 4-7d). In contrast, the bulk MoO<sub>3</sub> crystals lost the specific capacity only after the only first cycle at the current density of 10 A g<sup>-1</sup> (Fig. 4-7d). The MoO<sub>3</sub> nanofibers exhibited the improved reversible stability during the charge-discharge cycles. This improved rate performance could be the result of not only nanosizing, but also, the precise control of the morphology of nanocrystals. The 1D MoO<sub>3</sub>, which has the 2D diffusion channel<sup>104</sup>, the short Li<sup>+</sup> diffusion path ca. 50 nm along [101] direction was observed (Fig. 4-5c, 4-7e). These results agree well with past intensive researches on LiFePO<sub>4</sub>, which suggests that control of particle shape could be as important as average size control. For example, LiFePO<sub>4</sub>, it is suggested that thin particle with large (010) face of LiFePO<sub>4</sub>, where it has the 1D Li<sup>+</sup> diffusion path along the [010] direction, would increase the active area and reduce the diffusion length for Li ions.<sup>125,126</sup>

#### 4.3.3. Self-assembly of 1D MoO<sub>3</sub> towards oxide papers

As we show in the electrochemical properties of 1D MoO<sub>3</sub> as an example for an application of 1D materials, they have promising features to be used in electronic devices. However, the difficult collection and large scale synthesis of nanomaterials is the one of the major challenges for practical application.

Here we show a facile method to assemble the 1D MoO<sub>3</sub> (Fig. 4-8): We can fabricate large-scale oxide paper just by mixing the fibers and water as the dispersion medium (step 1), casting the mixture on Al foils as the substrates (step 2), and drying it (step 3).



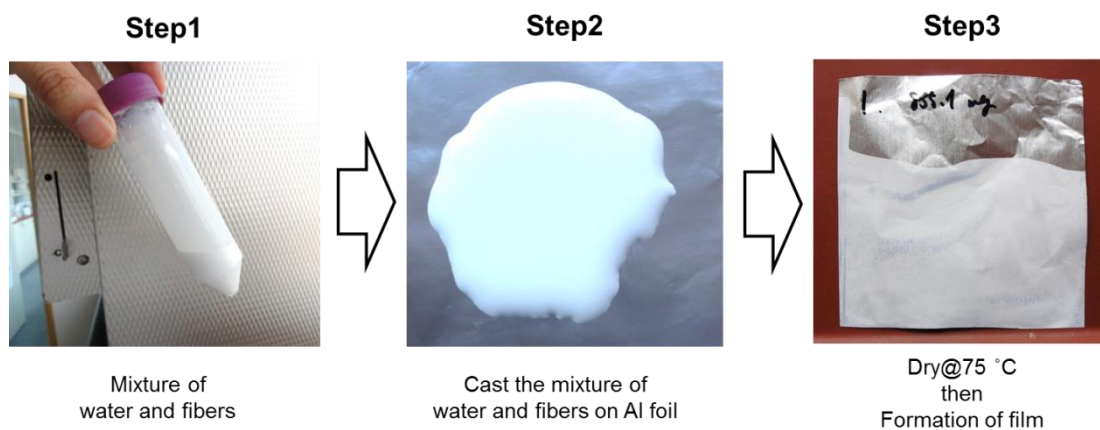


**Figure 4-8 | Schematic illustration of the formation process of macroscopic oxide papers made of 1D MoO<sub>3</sub>.**

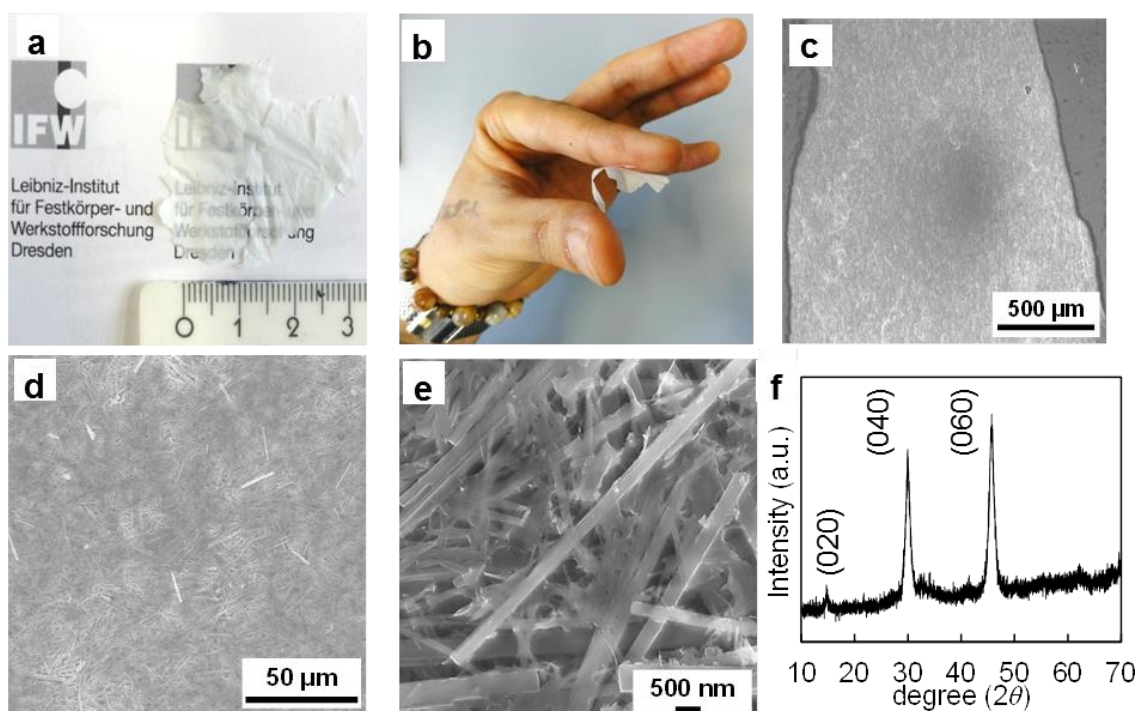


**Figure 4-9 | Characterizations of MoO<sub>3</sub> paper.** (a) Freestanding, semi-transparent MoO<sub>3</sub> paper. (b) Flexibility of macroscopic MoO<sub>3</sub> paper. (c,d,e) FESEM images of MoO<sub>3</sub> paper. (f) XRD pattern of MoO<sub>3</sub> paper.

The freestanding semi-transparent films made of 1D MoO<sub>3</sub> (3–5 cm in width) were obtained after drying the mixture of water and 1D MoO<sub>3</sub> (Fig. 4-9a). The semi-transparent feature suggests a dense packed assembly of suspensions. The oxide freestanding-film shows a bendable character as shown in Fig. 4-9b. The morphological observations by the FE-SEM indicate the smooth surface of the film (Fig. 4-9c,d) and a paper like a structure, which is a random stacking of fiber materials, in a micro scale (Fig. 4-9e). However, the XRD pattern of the film selectively shows the diffraction from the (010) face, which means the preferred *b* axis orientation of 1D MoO<sub>3</sub> (Fig. 4-9f). From the FE-SEM observation and the XRD pattern of freestanding films, we confirm that the 1D MoO<sub>3</sub> was assembled randomly in the *c* axis but showed an oriented assembly in the *b* axis.

The formation process of the freestanding oxide papers made of the 1D MoO<sub>3</sub>, which have the preferred *b* axis orientation and the thickness of ca. 10 μm, could be explained by the homogenous distribution of suspended 1D MoO<sub>3</sub> due to suppression of coffee-ring effect for an anisotropic material.<sup>127</sup> The coffee-ring effect is a phenomenon that occurs in a drying process of a liquid drop on a solid surface<sup>128–131</sup>: The suspended materials in a drop are brought to the edge due to the capillary flow from the center of the drop, and after the evaporation, the suspended materials form a shape along with an original form of the drop edge. Due to this effect, it is difficult to make a uniform coating by using only water as a solvent.<sup>133</sup> The recent report by Yunker *et al.* showed that anisotropic suspensions can suppress the coffee-ring effect and can lead to form a uniform coating on substrates without any assistance from organic compounds.<sup>127</sup> Based on their findings and other reports on the self-assembly processes, the formation process of the oxide freestanding film consisting of 1D MoO<sub>3</sub> can be described as following: 1) the 1D MoO<sub>3</sub> forms a packed structure at the air-water interface at the edge of a drying drop with a preference orientation; 2) the self-assembly of the 1D MoO<sub>3</sub> causes growth

of the packed structure at the air-water interface; and 3) a film is formed by further supplying 1D  $\text{MoO}_3$  to the interface and we can obtain macroscopic films after the evaporation of water. The freestanding film formation can be applied for the mixture of 0D and 1D materials as a suspension. We used a spherical Super-P as a 0D material and the 1D  $\text{MoO}_3$  as a 1D material. Normally, 0D materials cannot form the uniform film due to a coffee-ring effect. However, by mixing with anisotropic suspended materials with 0D materials, it is suggested that one can achieve a uniform film.<sup>127</sup> As shown in Fig. 4-10a,b, we successfully obtained a composite film made of carbon black (a 0D material) and 1D  $\text{MoO}_3$  on the substrate. In Fig. 5c, we show the macroscopic structure for composite freestanding film. This film does not show the flexibility like a freestanding film only consisting of 1D  $\text{MoO}_3$  (Fig. 4-9b).

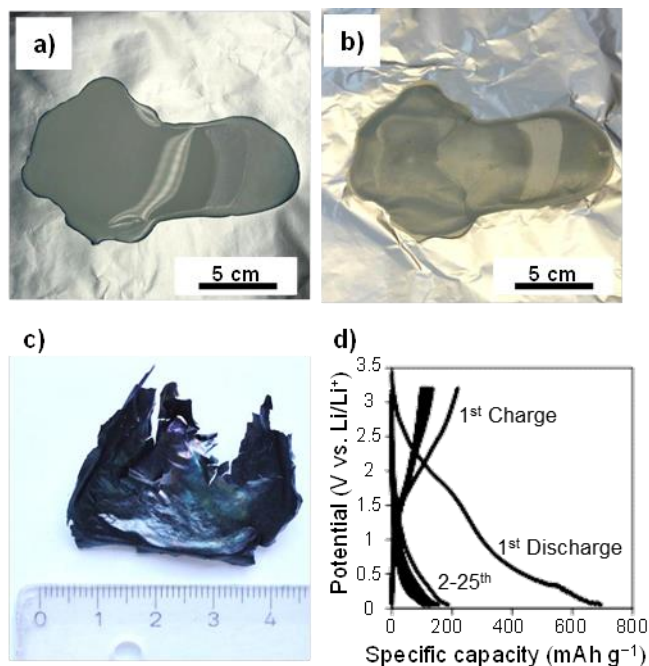
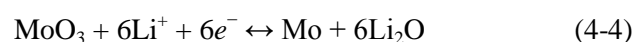


**Figure 4-10 | Characterizations and electrochemical property of composite paper.** (a) Composite of 1D  $\text{MoO}_3$  and 0D carbon material before dry. (b) Dried composite of 1D  $\text{MoO}_3$  and 0D carbon material. (c) Composite paper constituted of 1D  $\text{MoO}_3$  and 0D carbon material. (d) Charge-discharge curves of the composite paper electrode.

This could be because of the less dense packing and a lower degree of orientation of the composite film compared to the film constituted only by 1D MoO<sub>3</sub>. We tested this composite paper as an anode for LIBs. MoO<sub>3</sub> is expected to show following reaction as an anode material, so-called the conversion reaction<sup>55</sup>:



The eq. (4-4) shows the conversion reaction for MoO<sub>3</sub>, which has a theoretical specific capacity of  $\sim 1100 \text{ mAh g}^{-1}$ .

This reaction can show a reversible phase transformation between MX and M + LiM (M = transition metals, such as Fe, Mn, Co, Mo, Ru, Ag, and so on; X is typically H, N, O, and F), therefore this reaction can show a higher theoretical specific capacity due to the incorporation of a large number of Li<sup>+</sup> compared to the intercalation mechanism, which is a topotactical reaction. However, the huge change in crystal structures during the conversion reaction leads to electrode cracking, thus often, cycle performances for the conversion reaction show a fast degradation of a specific capacity. The composite paper electrode shows the first specific discharge capacity of  $\sim 800 \text{ mAh g}^{-1}$ , which is also included in the contribution to the capacity by the decomposition of the electrolyte and the formation of a solid electrolyte interface. For the first specific charge, the composite paper shows  $\sim 200 \text{ mAh g}^{-1}$ . After the first charge-discharge cycle, the composite paper shows a stable cycling with a specific capacity of  $\sim 200 \text{ mAh g}^{-1}$  until 20<sup>th</sup> cycle (Fig. 4-10d). The possible reason for this fast degradation might be due to the cracking as described above. Further improvement of the composite paper as an anode could be obtained by use of carbon nanofibers as conductive additives to fabricate more robust papers<sup>133</sup> or add the water soluble binders.

## 4. 4. SUMMARY FOR THE CHAPTER 4

In this chapter, an aqueous solution process for the eco-efficient synthesis-to-assembly of 1D MoO<sub>3</sub> was shown. By using this process, we obtained a single crystalline 1D MoO<sub>3</sub>, which shows high performance electrochemical properties emerged by a nanostructure control and a lower number of grain boundary. We assembled this 1D MoO<sub>3</sub> by a self-assembly process by suppressing the coffee-ring effect, and successfully obtained uniform freestanding oxide paper having the preferred *b* axis orientation of 1D MoO<sub>3</sub> as building blocks. This self-assembly method can be applied to fabricate a functional composite paper: we fabricated a composite paper made of carbon black (a conductive 0D material) and 1D MoO<sub>3</sub>. This composite paper was tested as an anode for LIBs and was confirmed to work. Further improvement can be achieved by the selection of better conductive materials. Our results indicate that the integration of eco-efficient, affordable, non-toxic synthesis and self-assembly of functional nanomaterials can be achieved by an aqueous solution process.

# CHAPTER 5. AN ENERGY STORAGE PRINCIPLE USING BIPOLAR POROUS POLYMERIC FRAMEWORKS

## 5. 1. INTRODUCTION FOR CHAPTER 5

Following contents are based on the author's publications: refs 134 and 135, and the manuscripts to be publish in *J. Phys. Chem. Lett.* and *J. Power Sources* as “Polymeric Frameworks towards Organic Semiconductors with Tunable Electronic Structures” and “Bipolar Porous Polymeric Frameworks for Low-cost, High-power, Long-life All-organic Energy Storage Devices”, respectively.

Design of new electrode materials is crucial for the improvement of energy storage technology. Finding of  $\text{LiCoO}_2$  led to the development of the nowadays used commercial high-energy rechargeable batteries.<sup>26</sup> precious metal nanoparticles can improve the energy efficiency of rechargeable lithium-air batteries.<sup>15,68</sup> However, considering materials abundance and sustainability, typical materials which can deliver high-performance properties are too expensive because of limited resources and they are often toxic. Redox-active organic materials are becoming important because of their possibility to achieve sustainable and greener Li-based rechargeable batteries, i.e. lithium-organic batteries.<sup>61,62</sup>

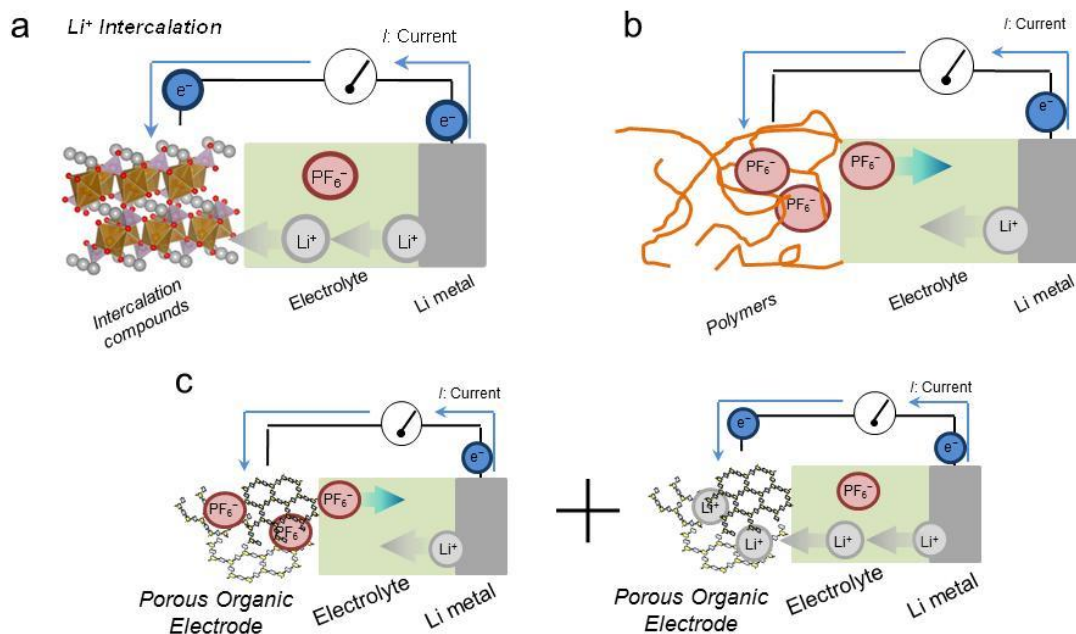


**Figure 5-1 | Schematic illustration of energy storage principles.** (a) The most common electrical energy storage principle which use cations as a charge carrier, such as  $\text{Li}^+$ ,  $\text{Na}^+$ ,  $\text{Mg}^{2+}$ , and  $\text{Al}^{3+}$ . (b) The energy storage principle using anions as a charge carrier. (b) The bipolar energy storage system based on porous organic electrodes using both cations and anions as charge carriers.

Although a lot of efforts are carried out to improve metal-free electrodes, it is still necessary to find new and optimized candidates for improving lithium-organic batteries. One of the most serious issues for organic electrodes is the trade-off between energy and power. Solving this problem is crucial because energy and power versatility of batteries is important for a sustainable society. To tackle this issue, a strategy has been fixed to begin with the consideration of materials properties by bottom-up approach starting from molecular building blocks. At the end of this investigations, the bipolar porous polymeric frameworks (BPPFs) have been utilized in rechargeable energy storage systems and showed their promising electrochemical properties.<sup>134,135</sup> The unique point of BPPFs is that electron can be carried to one direction, for example from anode to cathode, by using both cation and anion as charge

carriers. Lithium batteries use cation ( $\text{Li}^+$ ) as a charge carrier but they do not use anion (Fig. 5-1a). Some polymers use anions as a charge carrier (5-1b). However, BPPFs can use both species as charge carriers (Fig. 5-1c), and therefore, an energy storage principle using this material has a huge potential to improve the specific capacity of energy storage devices.

BPPFs, in case of this thesis as “covalent triazine-based frameworks”, are synthesized on the way of arising graphitic carbon nitrides (*g*-CNs) researches. The first indication on solid-state carbon nitrides was given by J. v. Liebig in 1884.<sup>136</sup> After the huge efforts towards synthesis of highly condensed crystalline *g*-CNs,<sup>137–139</sup> this issue, why and how they are formed, has been solved by M. Bojdys, M. Antonietti, and A. Thomas by using  $sp^2$ -hybridized *g*- $\text{C}_3\text{N}_4$ .<sup>140</sup>

## 5. 2. EXPERIMENT

### 5. 2. 1. Synthesis of Porous Polymeric Frameworks (PPFs)

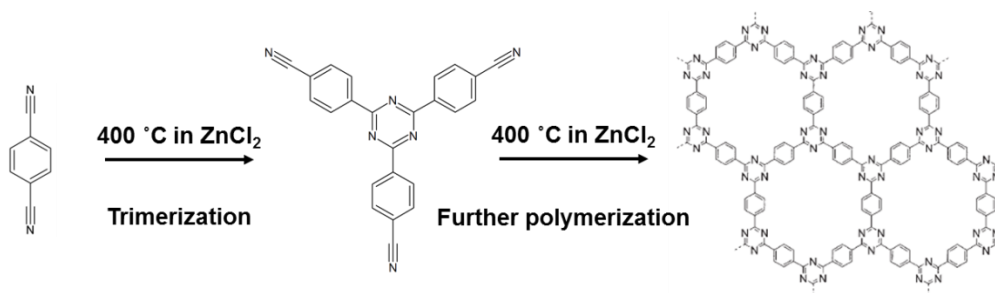


Figure 5-2 | Schematic illustration of ionothermal synthesis of CTF-1.

The porous polymeric frameworks were synthesized by ionothermal synthesis (Fig. 5-2).<sup>141</sup> The synthesis method for covalent triazine-based frameworks is: (CTF-1) heating a mixture of *p*-dicyanobenzene and  $\text{ZnCl}_2$  in quartz ampules at 400 °C for 40 hours. The obtained samples



were washed with 1 M HCl and distilled water for several times. After drying in vacuum oven, this material was used as the electrodes without further treatments.

### 5. 2. 2. Physical characterizations

The electron energy-loss spectroscopy (EELS) measurements were carried out using a Tecnai F30 (FEI company, equipped with a Gatan GIF 200 imaging energy filter) operated at an acceleration voltage of 300 kV by using a special sample holder which can keep the organic specimen cool. The FT-IR measurement was carried out by using a FT-IR-6200 (JASCO) or a Vertex 70 (Bruker) using KBr-IR pellet. The Raman spectroscopy measurements were carried out by using a Ventuno (NSR-1000DT, JASCO) with a laser excitation of 632.8 nm from a He-Ne laser. Samples for the spectroscopic measurements have been prepared by the following method: the electrochemical doping of anions in the PPFs was carried out by using galvanostatic intermittent titration technique (GITT). After the electrochemical doping, the doped PPF was washed by PC and Raman spectra were measured. The powder X-ray diffraction measurement was carried out on a Stadi P (STOE) diffractometer using Cu  $K\alpha_1$  radiation.

### 5. 2. 3. Electrochemical measurements

Electrodes were made by mixing active material (70 wt.%), carbon (carbon black = Super-P, TIMCAL; 20 wt.%), and binder (carboxyl methyl cellulose, DOW Chemicals; 10 wt.%). Al current collectors was used. The loading mass was  $\sim 1.5 \text{ mg cm}^{-2}$  and the electrode thickness was  $\sim 100 \text{ }\mu\text{m}$ . The cells were assembled in a purge-type dry glove box (MIWA MFG or M

Braun) filled with high purity Ar gas (N50 = 99.999 %) and tested them on a multichannel potentiostatic-galvanostatic system (SD-8, Hokuto-denko or VMP-3, Bio-logic) and a frequency response analyzer (SI 1250, Solatron). Alkali metals (lithium or sodium) were used as an anode and a reference electrode in lithium- and sodium-based energy storage device. 1M LiPF<sub>6</sub> in Ethylene Carbonate (EC):Dimethyl Carbonate (DMC) in 1/1 w/w (Kishida Chemicals or Merck) was used as an electrolyte and Swagelok-type cell or beaker-type three electrode cells were used for the lithium-based energy storage device. 1M NaClO<sub>4</sub> in propylene carbonate was used as an electrolyte (Kishida Chemicals) and a three electrode beaker cell was used as the test cell for sodium-energy storage device experiment. 1M NaClO<sub>4</sub> in acetonitrile (Kishida Chemicals) was used as an electrolyte for sodium-based all organic energy storage devices. The charge-discharge properties were recorded in a typical potential range from 4.5 to 1.5 V vs. Li/Li<sup>+</sup> (lithium battery system) or from 4.1 to 1.3 V versus Na/Na<sup>+</sup> (sodium battery system). Electrochemical impedance spectroscopy (EIS) measurements were carried out at specific potentials at *p*-dopable region and *n*-dopable region after achieving each quasi-equilibrium state by taking a rest of 1 hour after the doping. A frequency range from 10 mHz to 10 kHz with an amplitude of 10 mV was applied for the EIS measurements. The fitting was carried out by using Z-View (Scribner Associates). All charge-discharge properties were measured after charging till 4.5 V vs. Li/Li<sup>+</sup> (lithium battery system) or 4.1 V vs. Na/Na<sup>+</sup> (sodium battery system). Specific energy  $E$  (Wh kg<sup>-1</sup>) and specific power  $P$  (W kg<sup>-1</sup>) can be calculated by  $E = 0.5C(\Delta V)^2/3.6$  and  $P = E/(t/3600)$ , respectively, where  $C$  (F g<sup>-1</sup>) is the experimentally determined specific capacitance,  $\Delta V$  (V) is the working voltage range and  $t$  (s) is the discharge time.  $C$  is calculated from potential versus time profiles during the discharge process according to  $C = i/[-(V/t)m]$ , with  $m$  (g) being the mass of the active materials,  $V$  (V) being the discharge voltage, and  $i$  (A) being the applied current.

## 5. 3. LITHIUM-ORGANIC ENERGY STORAGE DEVICE

### 5. 3. 1. Introduction

The aim of this chapter is to develop an energy storage principle, which can deliver a 2–3 times higher specific energy than current batteries having a high rate capability. In the present work, it was demonstrated that covalent triazine-based frameworks (CTFs) can be successfully used as a cathode material. It exhibits a unique Faradaic reaction since it can be present in a *p*-doped and an *n*-doped state. During charging and discharging the polymeric cathode changes its charge state through a continuous, linear bipolar redox mechanism. The outcome is a remarkably high specific energy of 1084 Wh kg<sup>-1</sup> combined with a high specific power of 13238 W kg<sup>-1</sup> based on the mass of the framework. The present finding could mark a new route how to improve the performance of lithium-based energy storage devices by employing artificial porous polymeric frameworks as electrode materials.

Porous polymeric frameworks are synthesized from the rational assembly of organic monomers.<sup>141,148-151</sup> Their properties are tunable by choosing various combination of monomers to create artificial purely organic frameworks with a high potential for emerging applications through the porous properties,<sup>149,150,151</sup> such as catalysts,<sup>153,154</sup> gas adsorption,<sup>148</sup> and electric double layer capacitors (EDLCs).<sup>155</sup> The advantages for the use of these functional polymeric frameworks are 1) non-toxicity, 2) no use of expensive rare earth elements, 3) high stability of the frameworks and, most importantly, 4) the possibility to change the electronic properties by changing the structure.<sup>149</sup> These features make this class of polymers an interesting candidate for the electrode material in rechargeable electrical energy storage devices.

Inspired by these considerations, covalent triazine-based frameworks (CTFs), synthesized from *p*-dicyanobenzene, CTF-1 was investigated. It provides 1) a high specific capacity and power which are delivered by a unique energy storage mechanism using both p- and n-doped states for the cathode, and consequently shows a capacity-like bipolar redox reaction with a linear transition from each doped state in the energy storing process, 2) a large working potential because of the high stability of C-N bonds in the framework,<sup>141,151</sup> 3) rapid ion transport by the electrolyte-filled porous network<sup>146</sup> and 4) a large electrode surface area. The combined characteristics of a porous polymeric framework cathode which consists of triazine rings result in a remarkably high specific energy and high specific power.

### 5. 3. 2. Results and discussion

Physical characterization of PPFs was carried out by following procedures. The covalent triazine-based frameworks were synthesized in both a disordered (ACTF-1) and a crystalline state (Figure 5-3).<sup>141</sup>

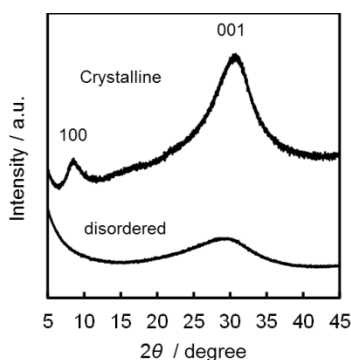
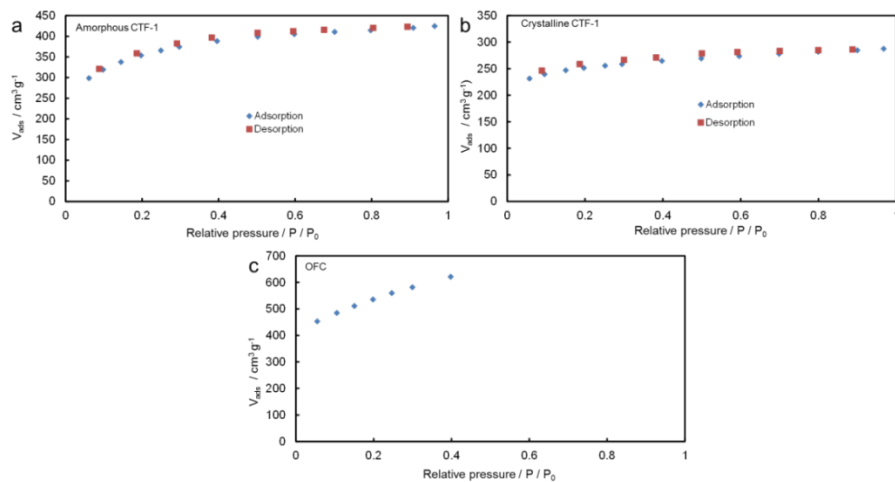
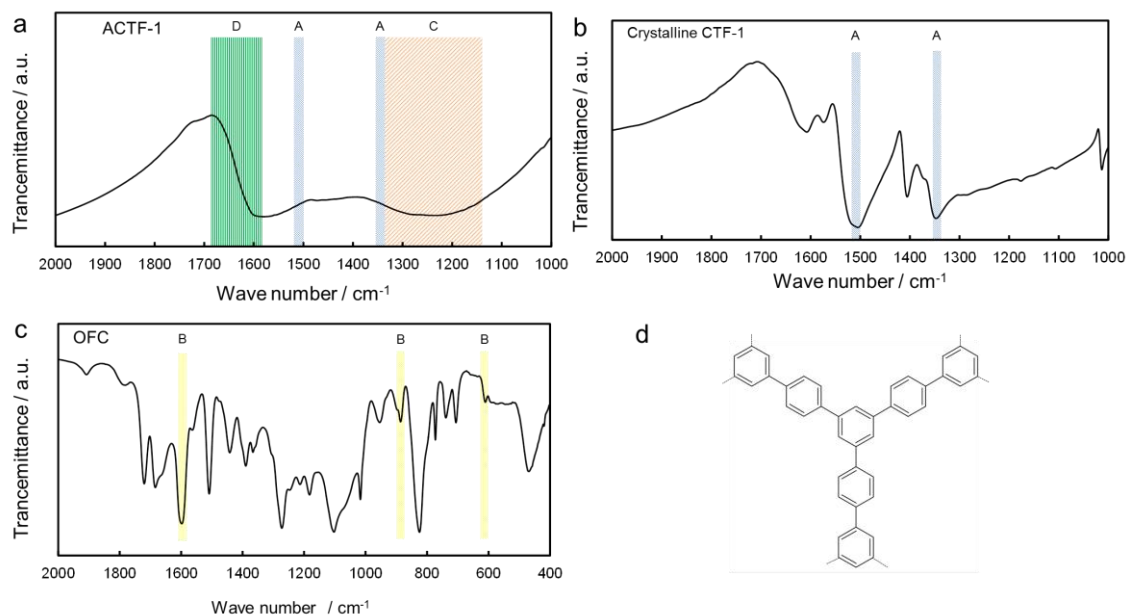


Figure 5-3 | XRD patterns for disordered and ordered CTF-1.



**Figure 5-4 | Nitrogen physisorption for porous organic frameworks at 77 K.** (a) N<sub>2</sub> isotherms on ACTF-1. (b) N<sub>2</sub> isotherms on crystalline CTF-1. (c) N<sub>2</sub> isotherms on OFC. The surface areas were calculated by Brunauer-Emmett-Teller method at a relative pressure of 0.3 and the total pore volume at a relative pressure of 0.97. The measurements were carried out at a Quantachrome Quadrasorb apparatus.



**Figure 5-5 | FT-IR measurements for porous organic frameworks.** (a) Spectrum of ACTF-1. (b) Spectrum of crystalline CTF-1. (c) Spectrum of OFC. (d) Structure of OFC.

As measured by the nitrogen physisorption experiments (Fig. 5-4), the ACTF-1 shows a surface area of  $1,140 \text{ m}^2 \text{ g}^{-1}$  with a total pore volume of  $0.656 \text{ cm}^3 \text{ g}^{-1}$ . The crystalline CTF-1 shows a surface area of  $792 \text{ m}^2 \text{ g}^{-1}$  with a total pore volume of  $0.445 \text{ cm}^3 \text{ g}^{-1}$ . The OFC (ref. 156 and Fig. 5-5d) shows a surface area of  $1,770 \text{ m}^2 \text{ g}^{-1}$ . The Fourier transform infrared (FT-IR) spectroscopy measurements (Fig. 5-5a-c) showed following structure of organic frameworks: Absorption peaks A (at  $1,352 \text{ cm}^{-1}$  and  $1,507 \text{ cm}^{-1}$ ) indicate the triazine rings<sup>157</sup>. Absorption peaks B (at  $610 \text{ cm}^{-1}$ ,  $890 \text{ cm}^{-1}$  and  $1,595 \text{ cm}^{-1}$ ) indicate the 1,3,5-trisubstituted benzene rings<sup>156-158</sup>. ACTF-1 shows strong absorption peaks indicating the C-N stretch (C;  $1,150 \text{ cm}^{-1}$  –  $1,360 \text{ cm}^{-1}$ ) and open-chain imino (D;  $1,690 \text{ cm}^{-1}$  –  $1,590 \text{ cm}^{-1}$ ) because of ring fragmentation. These results of the nitrogen physisorption experiments and the FT-IR spectroscopy measurements for CTFs and other synthesized porous polymeric frameworks confirm the high specific surface area and high purity of the materials.

Electrochemical characterization of PPFs was carried out by following procedures. Cyclic voltammetry (CV) measurements were carried out to investigate the fundamental electrochemical properties of the porous polymeric electrodes by using  $1 \text{ M LiPF}_6$  in ethylene carbonate (EC): dimethyl carbonate (DMC) (1:1 in w/w) as the electrolyte. ACTF-1 shows a significantly improved electrochemical reaction compared to the crystalline CTF-1 (Figure 5-6a). The enhancement of electrochemical properties could be explained as follows. Earlier studies on carbonaceous materials have shown an improvement of specific capacity by amorphization of graphite resulting in a carbon consisting of small non-coplanar graphene.<sup>159-161</sup> There, the adsorption of  $\text{Li}^+$  ions on the surface of single sheets was proposed to explain the increase of the specific capacity of carbon.

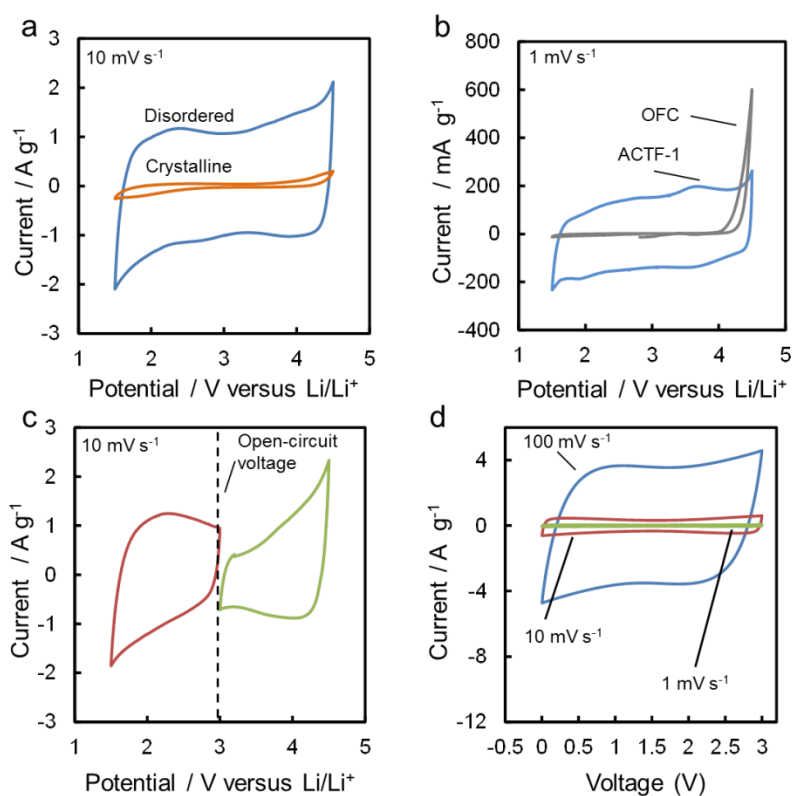


**Figure 5-6 | Cyclic voltammograms for a various porous polymeric frameworks.** (a) Comparison of cyclic voltammogram data of ACTF-1 and crystalline CTF-1. (b) Comparison of cyclic voltammogram data of the ACTF-1 and the benzene-based organic framework (OFC). (c) Cyclic voltammogram data for an ACTF-1 electrode obtained above and below open-circuit voltage (3 V vs. Li/Li<sup>+</sup>). (d) Cyclic voltammogram data for a polymer/polymer cell. The scan speed applied ranges from 1.0 mV s<sup>-1</sup> to 100 mV s<sup>-1</sup>.

**Table 5-1.** Relationships between specific surface area and specific capacitance on PPFs

Sample	ACTF-1	Crystalline CTF-1	OFC
Specific Surface Area (m <sup>2</sup> g <sup>-1</sup> )	1140	792	1770
Specific Capacitance (F g <sup>-1</sup> )	~137	~8	~19

ACTF-1 is also suggested to be formed by rather well-defined networks based on the sheet-like structure, however, without a long-3D-regular arrangement.<sup>162</sup> Pores with a size of 0.7–0.9 nm surrounded by small graphite stacking blocks are assumed to enable to trap Li as small clusters.<sup>163</sup> Ordered mesoporous carbons (CMK-3) with a pore size of 3 nm also have shown improved electrochemical properties.<sup>164</sup> CTF-1 has 1–2 nm pores even in amorphous structure.<sup>162</sup> From this point of view, the amorphous structure and micropores of CTF-1 could facilitate the electrochemical reaction, as indicated by the cyclic voltammetry measurements. The performance of the benzene-based polymeric framework (OFC, ref. 156) indicates that the triazine rings are involved in the electrochemical reaction of ACTF-1 and responsible for the stability in the potential range of 1.5–4.5 V vs. Li/Li<sup>+</sup> because the main difference between the two polymeric frameworks is the presence of triazine rings (Figure 5-6b). Moreover, crystalline CTF-1 and OFC show low specific capacitances even in their high surface areas as well as the specific surface of ACTF-1 (Table 5-1). This result indicates that energy storage mechanism of ACTF-1 is different from EDLCs because the electrochemical property of EDLCs is depended on the specific surface area of porous materials. The cyclic voltammogram of ACTF-1 electrodes below and above the open-circuit voltage of 3 V vs. Li/Li<sup>+</sup> (Figure 5-6c) suggests that ACTF-1 has a reduced (*n*-doped) state below 3 V vs. Li/Li<sup>+</sup> and an oxidized (*p*-doped) state above 3 V vs. Li/Li<sup>+</sup>.



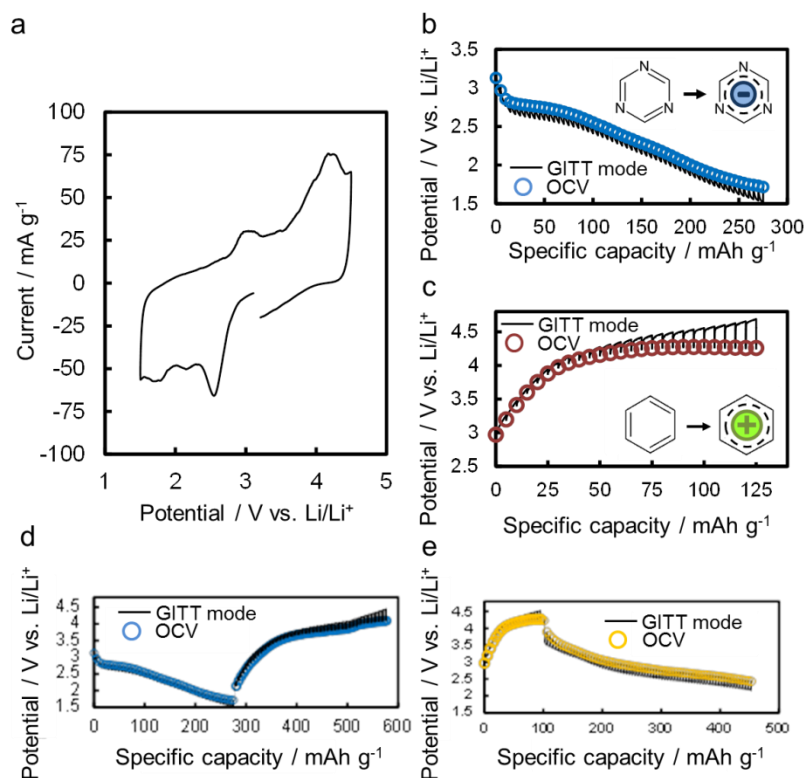


**Figure 5-7 | Electrochemical characterization of ACTF-1.** (a) Cyclic voltammogram data of ACTF-1 at  $0.1 \text{ mV s}^{-1}$ , (b) Open Circuit Voltage (OCV) curve from initial OCV to the *n*-doping region ( $1.5 \text{ V vs. Li/Li}^+$ ), and (c) OCV curve from initial OCV to the *p*-doping region ( $4.7 \text{ V vs. Li/Li}^+$ ). (d) OCV curve for ACTF-1 in the *n*-doping region (from initial OCV to  $1.5 \text{ V vs. Li/Li}^+$ ) and the continuous charging from  $1.5$  to  $4.5 \text{ V vs. Li/Li}^+$ . (e) OCV curve for ACTF-1 in the *p*-doping region (from initial OCV to  $4.5 \text{ V vs. Li/Li}^+$ ) and continuous discharging from  $4.5$  to  $2.0 \text{ V vs. Li/Li}^+$ . Solid lines show the voltage change during GITT experiments.

CV measurements were carried out at various scan rates for a symmetrical polymer/polymer cell using ACTF-1 as a cathode and an anode to check the bipolarity of ACTF-1 (Figure 5-6d).<sup>156</sup> The existence of reduced and oxidized states is indispensable for this material to be used as the electrode in a rechargeable energy storage device. Such polymer electrodes take up or give off ions in order to maintain electroneutrality, during their oxidation and reduction.<sup>61,62,166</sup> A CV measurement at a very slow scan rate of  $0.1 \text{ mV s}^{-1}$  shows several redox peaks in both *p*- and *n*-doping regions (Figure 5-7a). These peaks are confirmed by open-circuit voltage (OCV) curves (Figure 5-7b-e) which were taken by the galvanostatic

intermittent titration technique (GITT). Both OCV curves were measured from initial OCV (3 V vs. Li/Li<sup>+</sup>) of ACTF-1 from *n*- or *p*-doping region, respectively, since it needs to take only the information about *n*- or *p*-doping process. Clear redox peaks at 2.8 and 4.2 V vs. Li/Li<sup>+</sup> were observed in CV data (Figure 5-7a). And these redox peaks were confirmed by the plateaus in OCV curves: the plateau for *n*-doping process is at 2.8 V vs. Li/Li<sup>+</sup> in Figure 2b and *p*-doping is at 4.2 V vs. Li/Li<sup>+</sup> in Figure 5-7c. In Figure 5-7a, several redox peaks are shown by CV measurement. OCV curves were measured to find out peaks which can be attributed to *p*-doping and *n*-doping, respectively. In Figure 5-7b or Figure 5-7d, the clear plateau can be found at 2.8 V vs. Li/Li<sup>+</sup>, which can also be found by the CV measurement (Figure 5-7a). Below 2.8 V vs. Li/Li<sup>+</sup>, there is no clear plateau but a sloping curve was found which suggests that *n*-doping also was continued below 2.8 V vs. Li/Li<sup>+</sup>. After *n*-doping until 1.5 V vs. Li/Li<sup>+</sup>, the OCV curve for ACTF-1 from 1.5 to 4.5 V vs. Li/Li<sup>+</sup> was measured (Figure 5-7d). The measurement for Figure 5-7d was taken continuously. Two plateaus at 3.8 and 4.2 V vs. Li/Li<sup>+</sup> were observed until 4.5 V vs. Li/Li<sup>+</sup> after the *n*-doping (Figure 5-7d). Then, if one carries out *p*-doping for ACTF-1 without *n*-doping, only one plateau at 4.2 V vs. Li/Li<sup>+</sup> can be observed (Figure 5-7c or Figure 5-7e). The result of Figure 5-7e reveals that the two plateaus in Figure 5-7d are attributed to that: (I) 3.8 V vs. Li/Li<sup>+</sup> shows giving off Li<sup>+</sup> from ACTF-1 which was doped below 3 V vs. Li/Li<sup>+</sup> (Figure 5-7a, Figure 5-7d), and (II) the plateau at 4.2 V vs. Li/Li<sup>+</sup> can be attributed to the electrochemical *p*-doping of PF<sub>6</sub><sup>-</sup> into ACTF-1 (Figure 5-7b and Figure 5-7e). The plateau at 4.2 V vs. Li/Li<sup>+</sup>, which suggests *p*-doping, can be clearly found if the GITT measurement is carried out until 4.7 V vs. Li/Li<sup>+</sup> (Figure 5-7c). Finally, after *p*-doping until 4.5 V vs. Li/Li<sup>+</sup>, OCV curve for ACTF-1 from 4.5 to 2.0 V vs. Li/Li<sup>+</sup> was taken (Figure 5-7e). The measurement for Figure 5-7e was taken continuously. No clear plateau can be found in Figure 5-7e. This result

suggests that  $\text{PF}_6^-$  was given off from ACTF-1 in the broad potential region below 4.5 vs.  $\text{Li}/\text{Li}^+$ . This feature confirms the result of the CV measurement (Figure 5-7a).

In conclusion, the bipolar character of ACTF-1 was confirmed: (I) *n*-doping (the electrochemical doping of  $\text{Li}^+$ ) for ACTF-1 occurs in the broad potential region below 3 V vs.  $\text{Li}/\text{Li}^+$ . A peak for the *n*-doping was found at 2.8 V vs.  $\text{Li}/\text{Li}^+$ , and the release of  $\text{Li}^+$  from ACTF-1 also occurs in the broad potential region. The peak for the release of  $\text{Li}^+$  was found at 3.8 V vs.  $\text{Li}/\text{Li}^+$ ; and (II) following *p*-doping (the electrochemical doping of  $\text{PF}_6^-$  into ACTF-1) after extraction of  $\text{Li}^+$  occurs at 4.2 V vs.  $\text{Li}/\text{Li}^+$  and the release of  $\text{PF}_6^-$  occurs in the broad potential region. In the section 5.6., the detailed electrochemical features of PPFs considering electronic structures and possible hosts for the ion coordination are discussed for further understanding of the electrochemical reaction of PPFs.

In-situ electrochemical impedance spectroscopy (EIS) measurements were performed to study the electrochemical energy storage mechanism of ACTF-1 in more detail. A frequency range from 10 mHz to 10 kHz with an amplitude of 5 mV was applied for ACTF-1 in the *p*-doping and *n*-doping region, respectively (Figure 5-8). The Nyquist plots in both the *n*-doping and *p*-doping region show a semicircle which suggests the existence of charge transfer at the ACTF-1/electrolyte interface and Warburg impedance tilt angles near  $45^\circ$  show a typical redox electrochemical reaction (Figure 5-8b,e).<sup>167,168</sup> Indeed, in-situ EIS measurement for activated carbon (specific surface area =  $1950 \text{ m}^2 \text{ g}^{-1}$ , Kansai Coke and Chemicals Co., Ltd.) was carried out in the potential range of above and below OCV to compare with electrochemical reaction of ACTF-1 (Figure 5-9). Activated carbon electrodes interact with  $\text{PF}_6^-$  above OCV (Figure 5-9a) and with  $\text{Li}^+$  below OCV (Figure 5-9b). Each Nyquist plot for the activated carbon electrodes (mixture of activated carbon 70 wt.%, Super-P 20 wt. %, and the binder 10 wt. %).

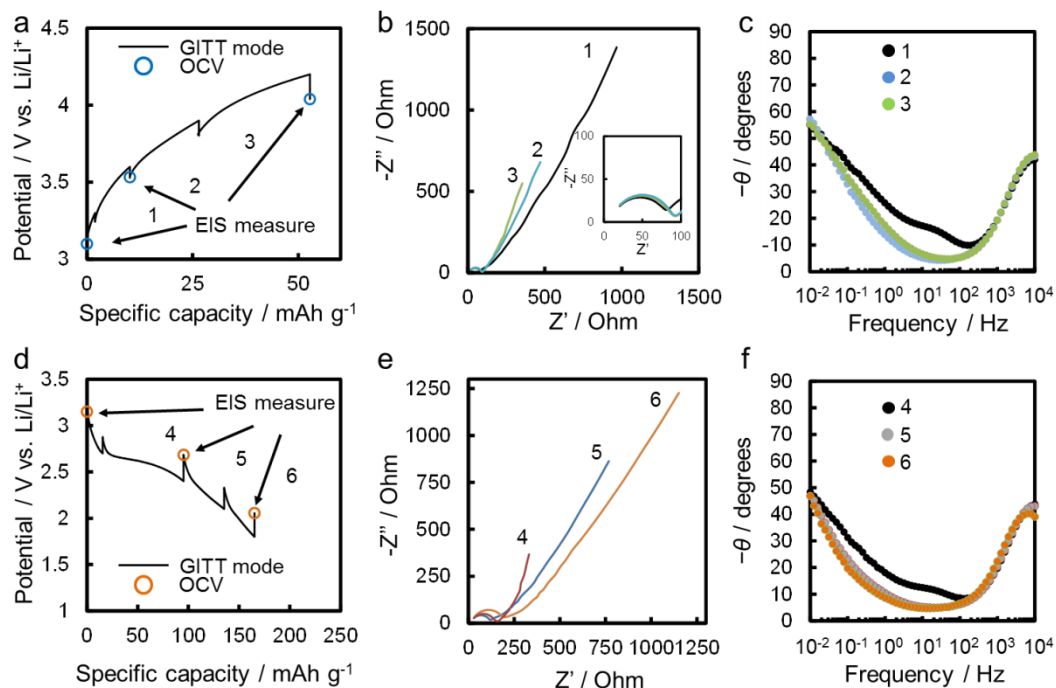


**Figure 5-8 | In-situ electrochemical impedance spectroscopy (EIS) measurements for ACTF-1.** (a) Open-circuit voltage (OCV) curve for ACTF-1 in the *p*-doping region. (b) Nyquist plots for ACTF-1 in the *p*-doping region. (c) Bode plots related to (b). (d) OCV curve for ACTF-1 in the *n*-doping region. (e) Nyquist plots for ACTF-1 in the *n*-doping region. (f) Bode plots related to (e). Insets show the plots in high frequency region. Solid lines in (a) and (d) are voltage changes during GITT experiments.

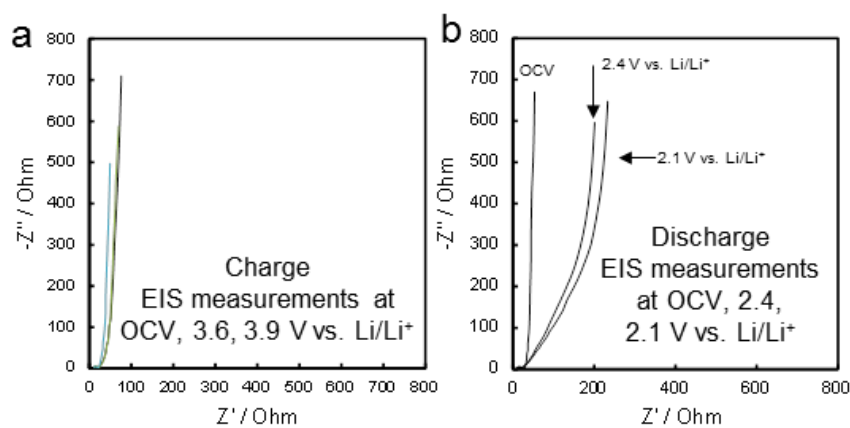


**Figure 5-9 | In-situ electrochemical impedance spectroscopy (EIS) measurements for activated carbon.** (a) Nyquist plots for activated carbon in the potential region above OCV. (b) Nyquist plots for activated carbon in the potential region below OCV.

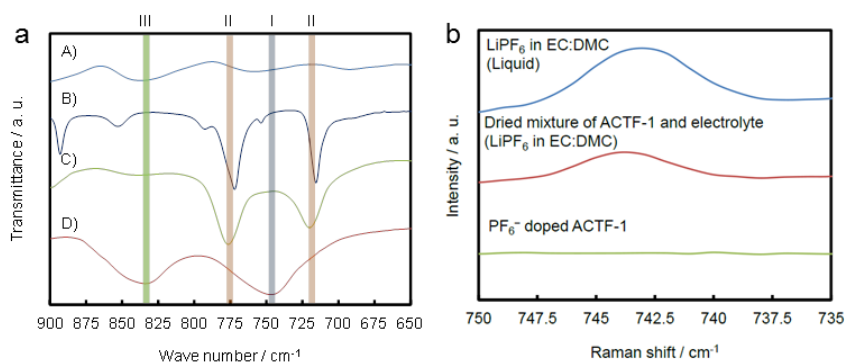


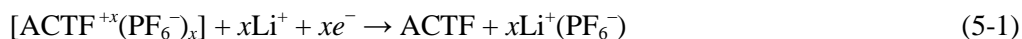
**Figure 5-10 | Spectroscopic measurements for *p*-doped ACTF-1.** (a) Fourier transform infrared spectroscopy measurements for A) as prepared ACTF-1, B) organic solvents (EC:DEC), C) dried mixture of ACTF-1 and the electrolyte (LiPF<sub>6</sub> in EC:DMC), and D) electrochemically PF<sub>6</sub><sup>-</sup> doped ACTF-1 (= the *p*-doped ACTF-1). (b) Raman spectroscopy measurements for LiPF<sub>6</sub> in EC:DMC (Liquid), the dried mixture of ACTF-1 and the electrolyte, and PF<sub>6</sub><sup>-</sup> doped ACTF-1.

The counter electrode is Li metal. The electrolyte is 1 M LiPF<sub>6</sub> in EC:DMC) shows a signal typical for electric double layer capacitors (EDLCs) in both region 1 and 2 by Warburg tilt angle near to 90°. These results clearly reveal the difference in the energy storage mechanism between ACTF-1 (Faradaic reaction) and activated carbons (non-Faradaic reaction).

Hexafluorophosphate (PF<sub>6</sub><sup>-</sup>), which was electrochemically doped in ACTF-1, was detected by FT-IR (Fig. 5-10a) and Raman spectroscopy measurements (Fig. 5-10b). The peak I (743 cm<sup>-1</sup>) in D) is the infrared-inactive  $\nu_1$  mode for free PF<sub>6</sub><sup>-</sup> (Fig. 5-10a), that becomes active by the destruction of the octahedral symmetry of PF<sub>6</sub><sup>-</sup> due to the coordination to ACTF-1.<sup>169,170</sup> The peak II (775 cm<sup>-1</sup> and 717 cm<sup>-1</sup>) in B) and C) can be attributed to EC. The peak III (around 830 cm<sup>-1</sup>) in C) and D) is attributed to the infrared-active  $\nu_3$  mode for compounds consisting of PF<sub>6</sub><sup>-</sup>. These results reveal that the peak I, which was observed in D), is not from the free PF<sub>6</sub><sup>-</sup> originated from the residual electrolyte. The weak three peaks in A) can be assigned to aromatic C-H out-of-plane bend and 1,4-disubstituted benzene rings in ACTF-1, respectively.<sup>157</sup> Raman spectroscopy measurements (Fig. 5-10b) support the results of the FT-IR measurements. The peak for the dried mixture of ACTF-1 and electrolyte at 743 cm<sup>-1</sup> suggests the existence of free

PF<sub>6</sub><sup>-</sup>. On the other hand, the PF<sub>6</sub><sup>-</sup> doped ACTF-1 does not show any peaks at the position for free PF<sub>6</sub><sup>-</sup>. In conclusion, the doped PF<sub>6</sub><sup>-</sup> state in ACTF-1 was observed. Since those, the results of the FT-IR and Raman spectroscopy measurements clearly reveal the *p*-dopable nature of ACTF-1, the results suggest that the energy storage mechanism of ACTF-1 is processed by both *p*- and *n*-doping mechanism. Hence, it is suggested that the energy storage principle of ACTF-1 is based on a bipolar Faradaic reaction. Former investigations on triazine-based molecules showed reversible redox reactions.<sup>171,172</sup> This fact also supports our findings that triazine-based polymeric frameworks show reversible Faradaic reaction.

From our investigations, possible electrochemical reaction mechanism for the ACTF-1 is shown in Fig. 5-11: The ACTF-1 constituted of aromatic rings, indicated as ACTF, in the potential range below 3 V vs. Li/Li<sup>+</sup> (initial open-circuit voltage) can be reduced and oxidized according to ACTF + *x*e<sup>-</sup> ↔ ACTF<sup>-*x*</sup>. In the potential range above 3 V vs. Li/Li<sup>+</sup>, using LiPF<sub>6</sub> as a Li salt in the electrolyte, the redox reaction of C<sub>3</sub>N<sub>3</sub> involved with anion (PF<sub>6</sub><sup>-</sup>) is expected to occur<sup>61,62,166</sup>: ACTF + *x*PF<sub>6</sub><sup>-</sup> ↔ [ACTF<sup>+*x*</sup>(PF<sub>6</sub><sup>-</sup>)<sub>*x*</sub>] + *x*e<sup>-</sup>. Considering these two reactions with the reaction at the anode (Li metal): *x*Li ↔ *x*Li<sup>+</sup> + *x*e<sup>-</sup>, the charge and the discharge processes of benzene and triazine rings occur in two continuous linear redox reactions. For example, the discharge process from 4.5 to 1.5 V vs. Li/Li<sup>+</sup>, the first reaction (4.5–3.0 V vs. Li/Li<sup>+</sup>) can be described as:



The continuous and linear transition from *p*-doped state (oxidized state) to the *n*-doped state (reduced state) leads below 3.0 V vs. Li/Li<sup>+</sup>:



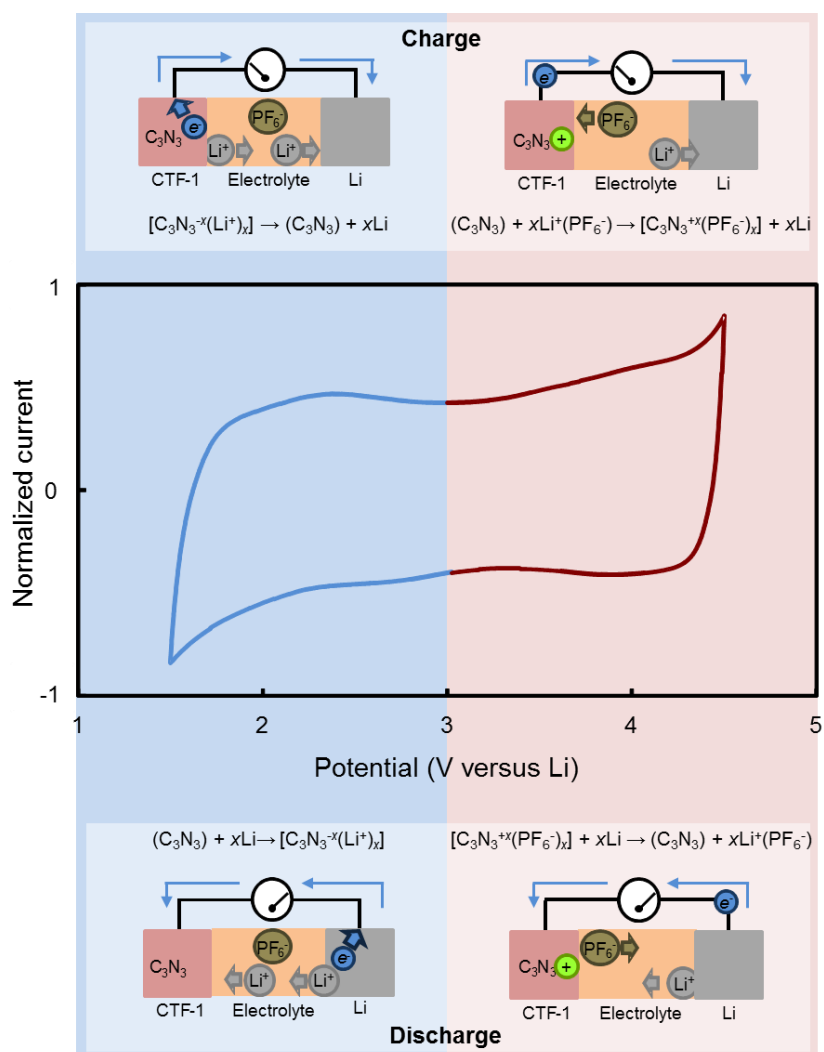


Figure 5-11 | Schematic illustration for the electrical energy storage mechanism of ACTF-1.

In this energy storage principle,  $\text{PF}_6^-$  is supplied from the electrolyte but  $\text{Li}^+$  is supplied from the anode. This energy storage system is different from current rechargeable lithium batteries using the intercalation mechanism and it is different from organic batteries including all-organic batteries which use bipolar redox active polymers for a *p*-dopable polymer cathode and *n*-dopable polymer anode<sup>1-3,24,25,26,61,62,173-174</sup>. The neutral state of the aromatic rings linearly and continuously bridges its oxidized state eq. (5-1) and reduced state eq. (5-2) by the continuous linear transition bipolar redox mechanism associated with  $\text{PF}_6^-$  and  $\text{Li}^+$ , respectively

(Fig. 5-11). This unique mechanism of ACTF-1 delivers the high-performance electrochemical properties.

The electrical energy storage characteristics of ACTF-1 electrodes were measured in two working potentials of 1.5–4.5 V vs. Li/Li<sup>+</sup> (Fig. 5-12) and 1.0–5.0 V vs. Li/Li<sup>+</sup> (Fig. 5-13). The charge-discharge profiles at various current densities from 0.05 A g<sup>-1</sup> to 20 A g<sup>-1</sup> in the working potential of 1.5–4.5 V vs. Li/Li<sup>+</sup> are shown in Fig. 5-12a. At a constant current density of 0.05 A g<sup>-1</sup>, the ACTF-1 electrode shows a specific capacity of ~160 mA h g<sup>-1</sup> based on the mass of ACTF-1 with a sloping voltage profile. Even for the remarkably high current density of 20 A g<sup>-1</sup>, ACTF-1 can provide a specific capacity of 60 mA h g<sup>-1</sup>. This is equivalent to a 125C rate, if one assume 160 mA h g<sup>-1</sup> as the specific capacity of ACTF-1 in the working potential of 1.5–4.5 V vs. Li/Li<sup>+</sup>. The rate of *n*C corresponds to a full discharge in 1/*n* h. The cycle performance of ACTF-1 electrodes was checked for at various current densities (Fig. 5-12b), revealing quite good cycle stability. Even under rather harsh conditions (25 cycles at different current densities from 0.1 A g<sup>-1</sup> to 20 A g<sup>-1</sup> without relaxation between the cycles), ACTF-1 reproduces the stable specific capacity of ~150 mAh g<sup>-1</sup> at 0.1 A g<sup>-1</sup>, thus retaining the same specific capacity as in the first 25 cycles at 0.1 A g<sup>-1</sup>. Moreover, ACTF-1 electrodes can be tested up to 1000 cycles with 84 % capacity retention at the high current density of 5.0 A g<sup>-1</sup> (Fig. 5-12c).

In Fig. 5-13a, the cyclic voltammogram for ACTF-1 in the potential range of 1.0–5.0 vs. Li/Li<sup>+</sup> is shown. In this working potential, the ACTF-1 electrode shows a high specific capacity of 542 mA h g<sup>-1</sup> at a constant current density of 0.05 A g<sup>-1</sup> and 164 mA h g<sup>-1</sup> at a constant current density of 5.0 A g<sup>-1</sup> (Fig. 5-13b). After cycling up to 50 times at 5.0 A g<sup>-1</sup>, the capacity retention of 70 % was observed (Fig. 5-13c). ACTF-1 electrodes show a high specific energy of 340 Wh kg<sup>-1</sup> combined with a high specific power of 50085 W kg<sup>-1</sup> based on the mass of ACTF-1 in the working potential of 1.5–4.5 V vs. Li/Li<sup>+</sup>.



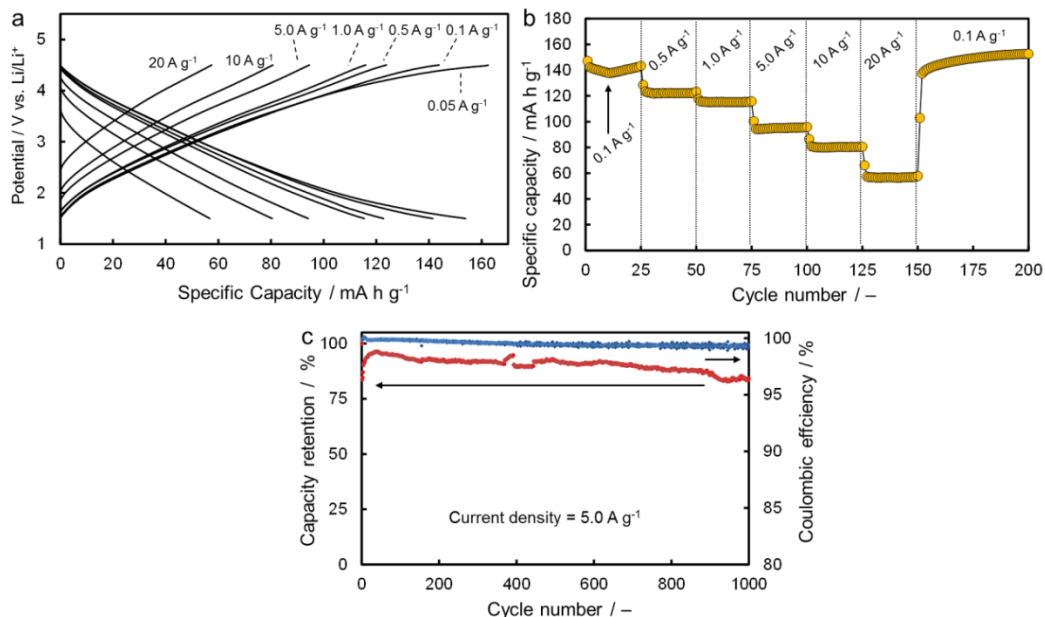


**Figure 5-12 | Electrochemical characterization of ACTF-1 in a potential range of 1.5-4.5 V vs. Li/Li<sup>+</sup>.** (a) Charge-discharge profiles of ACTF-1 with various current densities. (b) Cycle performance with various current densities. (c) Cycle performance of ACTF-1 up to 1000 cycles with a current density of 5.0 A g<sup>-1</sup>.

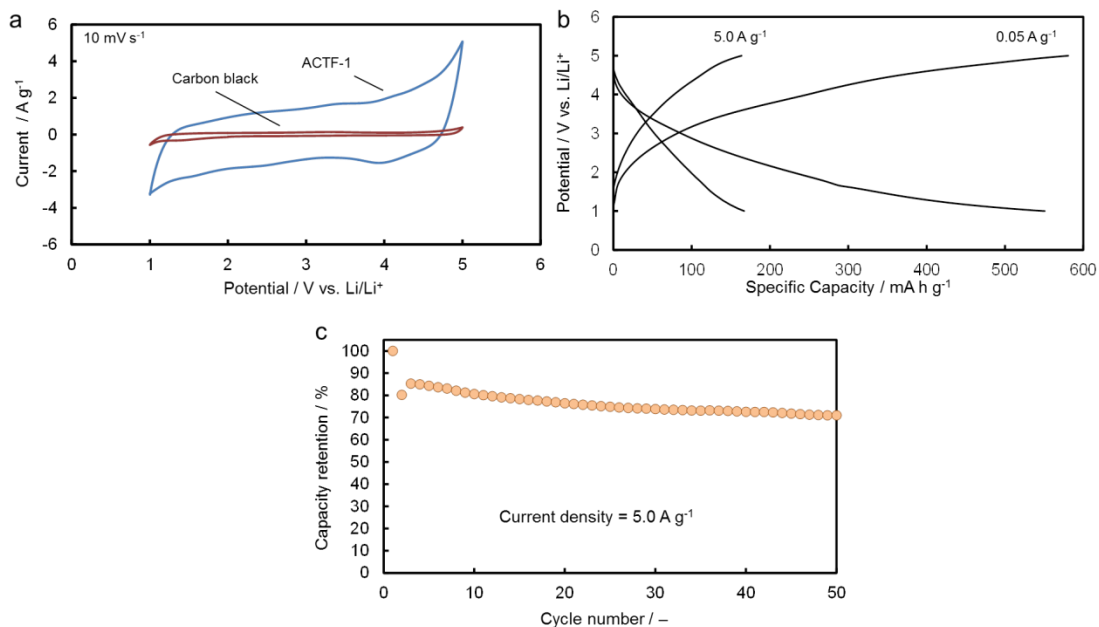


**Figure 5-13 | Electrochemical characterization of ACTF-1 in a potential range of 1.0-5.0 V vs. Li/Li<sup>+</sup>.** (a) CV for ACTF-1 electrode and carbon black electrode. The CVs show that the electrochemical reaction of carbon black is negligible in this potential range. (b) charge-discharge profiles of the ACTF-1 electrode at current densities of 0.05 A g<sup>-1</sup> and 5.0 A g<sup>-1</sup>. (c) Cycle property of ACTF-1 at the current density of 5.0 A g<sup>-1</sup>.

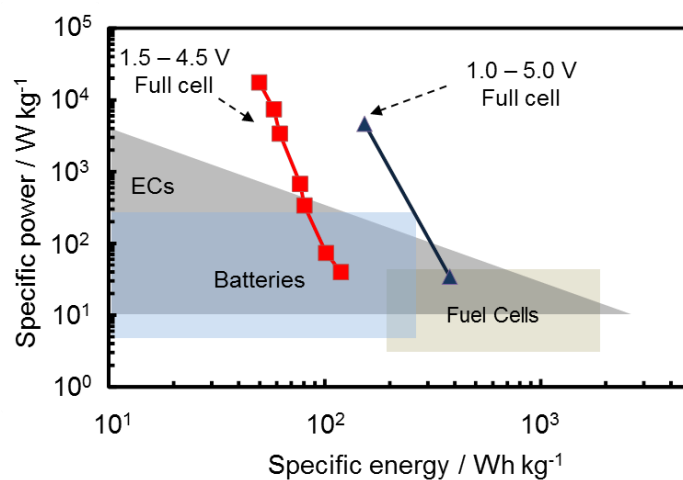


**Figure 5-14 | Ragone plot for lithium-organic energy storage device and a various electrical energy storage devices.** ACTF-1/Li full cells at a working potential of 1.5–4.5 V vs. Li/Li<sup>+</sup> are indicated by red, and at a working potential of 1.0–5.0 V vs. Li/Li<sup>+</sup> by blue. ECs = Electrochemical Capacitors. A full cell is estimated based on the assumption that the ACTF-1 constitutes 35 % of the total mass of the active materials in a cell.

In the working potential of 1.0–5.0 V vs. Li/Li<sup>+</sup>, ACTF-1 can deliver a remarkably high specific energy of 1084 Wh kg<sup>-1</sup> while also delivering a specific power of 13238 W kg<sup>-1</sup> based on the mass of ACTF-1. These results reveal the high electrochemical performances of ACTF-1 compare to typical specific energy and specific power of lithium-ion battery materials, ranged from ~500 Wh kg<sup>-1</sup> (ref. 145) and 500–2000 W kg<sup>-1</sup> (ref. 144), respectively.

Assuming that the ACTF-1 constitutes 35 % of the total mass of active materials in a full cell, this full cell will produce a high specific energy of 119 Wh kg<sub>cell</sub><sup>-1</sup> while showing a high specific power of 17529 W kg<sub>cell</sub><sup>-1</sup> at a working potential of 1.5–4.5 V vs. Li/Li<sup>+</sup> (Fig. 5-14, red). In the case of a working potential of 1.0–5.0 V vs. Li/Li<sup>+</sup> (Fig. 5-14, blue), the specific energy of ACTF-1/Li cells will reach 379 Wh kg<sub>cell</sub><sup>-1</sup> while also having the specific power of 4633 W kg<sub>cell</sub><sup>-1</sup>, which is comparable to the specific energy of fuel cells and the specific power of electrochemical supercapacitors.<sup>1</sup>

### 5.3.3. Conclusion for lithium-organic energy storage device

**I**n summary, our findings imply that ACTF-1 is a promising metal-free porous polymeric framework with a new energy storage principle which uses both p-doping and n-doping as a cathode material. Based on this energy storage concept, unusually high specific energy and specific power were demonstrated. The lithium-organic system based on ACTFs reaches a performance comparable to other possible next-generation energy storage systems, such as lithium-air and lithium-sulphur systems. The ability to increase their specific power and energy further could be possible due to the wide variety of different functional frameworks and starting monomers. This would significantly extend the possibilities of electrical energy storage, while avoiding the use of toxic transition metals or rare earth elements in today's high performance batteries.

## 5. 4. SODIUM-ORGANIC ENERGY STORAGE DEVICE

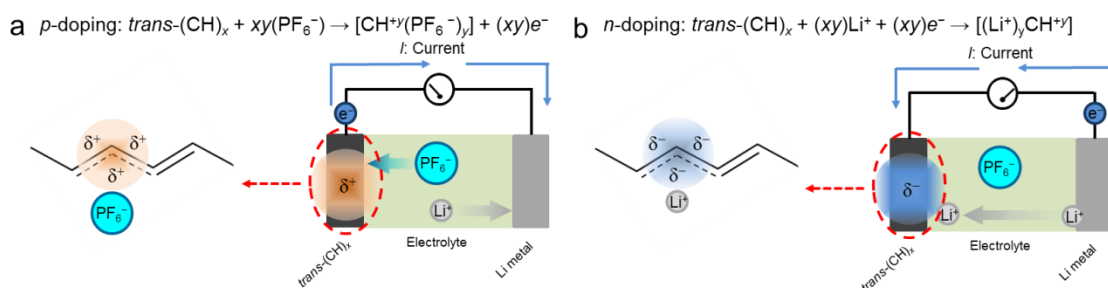


**Figure 5-15 | Typical electrochemical reactions of organic compounds: In case of polyacetylene.**

(a) *p*-dope type electrochemical reaction. (b) *n*-dope type electrochemical reaction.

### 5. 4. 1. Introduction

One possible approach is to use sodium as an alternative charge carrier<sup>177-190</sup> to lithium, as the cost of sodium carbonate ( $Na_2CO_3$ ), for example, is only 3 % of  $Li_2CO_3$  (ref. 179). Another approach which is even more effective for improving affordability is to replace the current metal-based electrodes with organic materials<sup>61,62,191-196</sup> that are more abundant in nature. Since the advent of conductive polymers<sup>59,60</sup> and reversible redox polymers<sup>192</sup> (Fig. 5-15), a large number of *p*-, *n*-, and bipolar organic electrodes have been investigated for energy storage devices due to their low-cost and possible applications in flexible plastic batteries<sup>191</sup>. While there is a long history of research in sodium-based energy storage devices, there have been only a few reports on organic materials applied to rechargeable sodium batteries, e.g., polyparaphenylene and sodium terephthalate<sup>193,194,196</sup>, and often they are only suitable as the anode. Finding a new, suitable group of organic materials for the application as cathodes in sodium batteries could stimulate the development of sodium-based energy storage devices and

meet the requirement of next-generation batteries, namely high specific energy and power, and most importantly, affordability.

In this section, a following content is discussed. Bipolar porous polymeric frameworks were found as a new class of affordable organic electrodes for a sodium-based energy storage device: An aromatic porous-honeycomb cathode, which shows a long cycle life of over 7,000 cycles and performances comparable to lithium-ion batteries, which are a high specific power of  $10 \text{ kW kg}^{-1}$  and a specific energy of  $500 \text{ Wh kg}^{-1}$  based on the weight of the organic electrode in half-cells.

#### 5. 4. 2. Results and discussion

**P**hysical characterization of the porous organic electrodes was carried out by the following procedures. The bipolar porous organic electrode (BPOE) is a porous-honeycomb, polymeric framework consisting of benzene rings and triazine rings in two-dimensional (2D) structure as already mentioned in the last section (Fig. 5-16a)<sup>134,141</sup>. Using a high resolution transmission electron microscopy, it has been confirmed that the BPOE has a sheet-like morphology which is with  $\sim 300 \text{ nm}$  wide (Fig. 5-16b and Appendix A-1) and typically less than 10 stacking layers, giving a thickness of  $\sim 4 \text{ nm}$ , were observed (Fig. 5-16b inset).

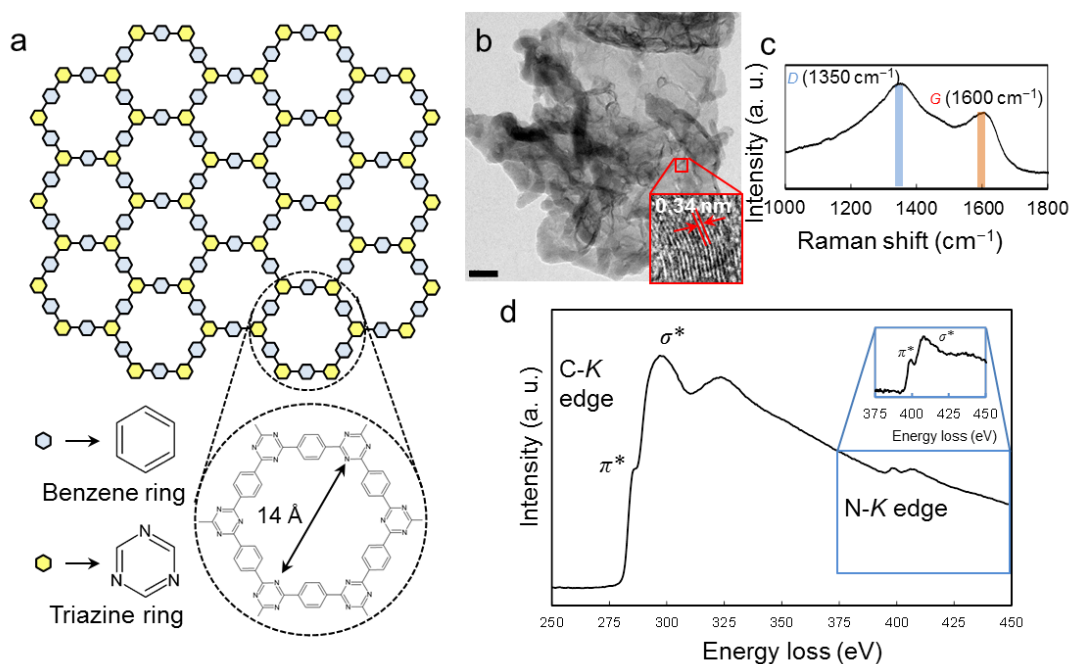


**Figure 5-16 | Structure and spectroscopy measurements for bipolar porous organic electrode (BPOE).** (a) Schematic illustration of the ideal BPOE having a porous-honeycomb structure with a pore diameter of 14 Å. The two-dimensional (2D) structure of the BPOE is constituted by triazine rings and benzene rings. (b) Transmission electron microscopy image of the BPOE showing a sheet-like morphology. The scale bar indicates 100 nm. The inset shows a cross-section of a multilayer BPOE, stacking of about 10 layers. See Appendix A-1 for the large image. (c) Raman spectrum of the BPOE at a laser excitation of 632.8 nm. The existence of the *G* peak reveals the graphene-like 2D structure. (d) Electron energy-loss spectrum of the carbon and nitrogen *K* edges recorded in the BPOE. The inset shows the N-*K* edge with subtraction of the background. The existence of  $sp^2$ -hybridized carbon and nitrogen atoms reveals the formation of graphitic network constituted by triazine and benzene rings.

Raman spectroscopy measurements (RSMs) allow to reveal the electronic structure of materials (= information about a structural periodicity of a material)<sup>197–199</sup>. Especially, graphite and graphene have been extensively researched concerning their electronic structure by RSMs<sup>197–201</sup>. The *G* peak is produced by the doubly degenerated zone center  $E_{2g}$  mode which is a motion of atoms in the 2D honeycomb structure<sup>197–199</sup>. This *G* peak also appears in the porous-graphene at same position as well as graphene. Furthermore, carbon nitride formed in 2D honeycomb structure shows the *G* peak at  $\sim 1600\text{ cm}^{-1}$  (refs. 198, 199).

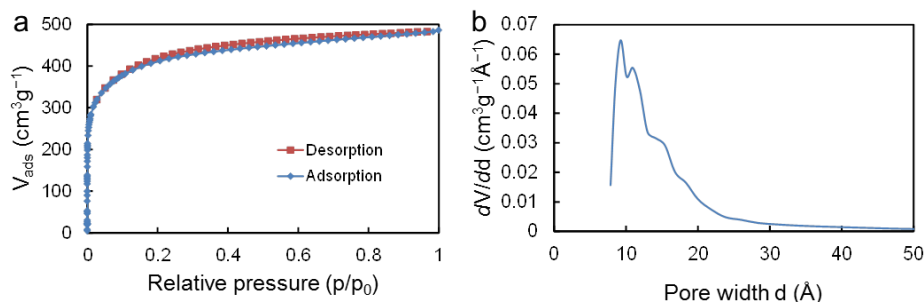


**Figure 5-17 | Porous structure of BPOE.** (a) Results of nitrogen physisorption experiments for the BPOE. (b) Pore-size distribution of the BPOE. Fig. 5-17a shows isotherm data for same material for Fig. 5-4a but different measurement to obtain pore-size distribution data.

Therefore, the  $G$  peak at  $\sim 1600\text{ cm}^{-1}$  in Fig. 5-16c reveals the existence of a 2D porous honeycomb structure which is constituted by benzene and triazine rings. However indeed, this framework is formed as a short-range-ordered 2D structure with the stacking of each 2D unit (Fig. 5-16a) in a non-coplanar fashion<sup>134,141,162</sup> as the global structure. This structure, which is revealed by Raman spectroscopy and XRD (Fig. 5-3), is comparable to a hard carbon, which is a disordered carbon consisting of single graphene sheets stacked at random angles<sup>160,202</sup>, and this confirms the reason of sloping charge-discharge curve described in the section 5.3. Electron energy-loss spectroscopy (EELS) measurements show a  $1s \rightarrow \pi^*$  transition which reveals the  $sp^2$ -hybridization for carbon and nitrogen at 285 eV and 400 eV, respectively (Fig. 5-16d) and the fine structure of the C- $K$  and N- $K$  edges also suggest a graphitic network with  $sp^2$ -bonding<sup>203</sup>. Indeed, the porous structure of the BPOE was investigated by nitrogen physisorption experiments (Fig. 5-17a). Its pore-size distribution confirmed the existence of micropores of ca.1.4 nm (Fig. 5-17b) which was observed by previous reports<sup>134,141,162</sup>. From these measurements, the formation of a short-range-ordered 2D polymeric framework constituted by aromatic rings was confirmed. Thus, the BPOE shows adjustable electronic properties and controllable semiconducting features emerging from their structural periodicity comparable to 2D atomic crystals, such as multilayer graphene, and a choice of monomer as a building

block<sup>138,204-208</sup>. Here it has been demonstrated that the bipolar characters of the BPOE required for high performance electrochemical properties are preserved even in a sodium battery system.

Electrochemical characterization of the porous organic electrodes was carried out by the following procedures. Electrochemical impedance spectroscopy (EIS) measurements were carried out at 3.3 V versus Na/Na<sup>+</sup> (*p*-doping process, Fig. 5-18a,b) and 2.3 V versus Na/Na<sup>+</sup> (*n*-doping process, Fig. 5-18c,d) after achieving each quasi-equilibrium state<sup>209</sup> in order to probe the physical and/or chemical phenomena at the interface between the BPOE and the electrolyte solution. A frequency range of 10 mHz to 10 kHz with an amplitude of 10 mV was applied in all EIS measurements. The Nyquist plots obtained by the EIS measurements were fitted using an equivalent circuit based on the Randels model<sup>210</sup> showing in Fig. 5-18a,c, where  $R$  is the electrolyte resistance,  $CPE = \{T_{CPE}(j\omega)^\alpha\}^{-1}$  is a constant phase element with  $\omega$  being the angular frequency and  $\alpha$  an empirical electrode roughness parameter, and where  $Z_w$  is the Warburg impedance indicating a diffusion-limited electrochemical reaction. Each Nyquist plot above and below 2.8 V versus Na/Na<sup>+</sup> shows a semicircle at high frequencies suggesting charge transfer at the polymeric framework/electrolyte (1 M NaClO<sub>4</sub> in propylene carbonate) interface. It also shows a characteristic linear diffusion-limited response at a tilt angle of close to 45° at low frequencies indicating incorporation of the ion in the electrode materials<sup>188,210</sup>. The FT-IR and Raman spectroscopy measurements (Fig. 5-18e,f) confirmed the coordination of the anion (ClO<sub>4</sub><sup>-</sup>) in the polymeric framework which was electrochemically incorporated. The ClO<sub>4</sub><sup>-</sup> doped bipolar porous organic electrode is indicated as I; 1M NaClO<sub>4</sub> in propylene carbonate is indicated as II; and propylene carbonate is indicated as III. In Fig. 5-18e, which shows the Raman spectra, the peaks assigned as 1 originates from propylene carbonate (PC). The peak 2A in II (935 cm<sup>-1</sup>) is the infrared-inactive, but it is Raman-active  $\nu_1$  mode for free ClO<sub>4</sub><sup>-</sup> (refs. 211–214).



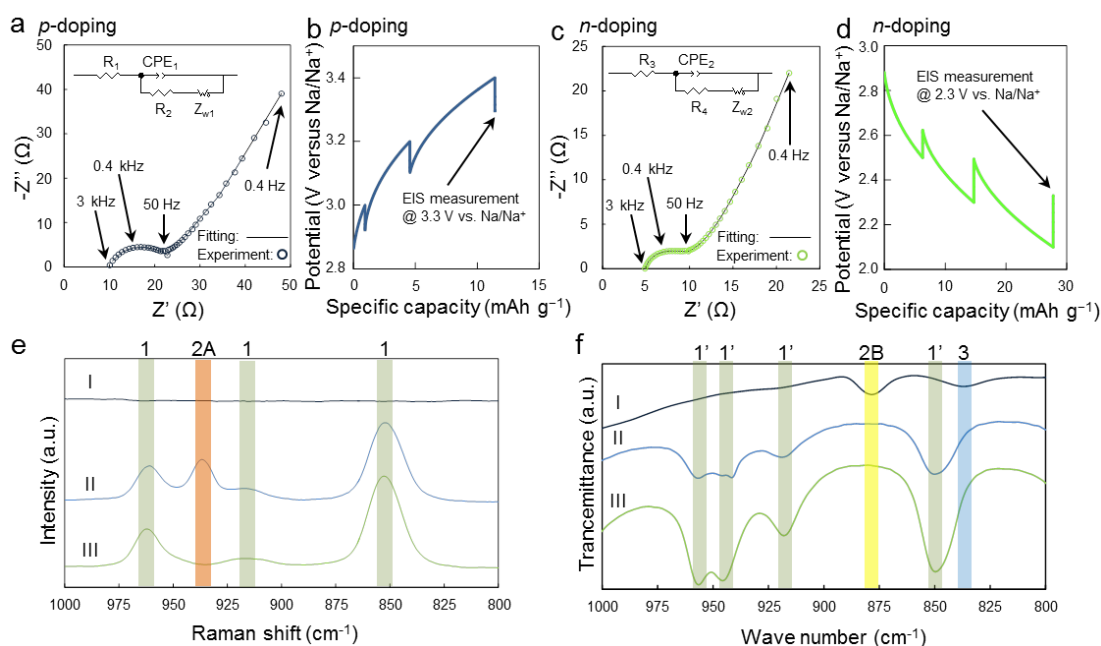


**Figure 5-18 | Electrochemical characterization of BPOE.** (a) Typical Nyquist plot in the *p*-dopable region and its equivalent circuit.  $R_1 = 10.53 \Omega$ ,  $R_2 = 8.51 \Omega$ ,  $T_{CPE1} = 437.16 \mu\text{F}$ , and  $\alpha = 0.91$ . (b) Potential value at the quasi-equilibrium state for the EIS measurement in the *p*-dopable region. (c) Typical Nyquist plot in the *n*-dopable region and its equivalent circuit.  $R_3 = 4.82 \Omega$ ,  $R_4 = 3.15 \Omega$ ,  $T_{CPE2} = 154.13 \mu\text{F}$ , and  $\alpha = 0.92$ . (d) Potential value at the quasi-equilibrium state for the EIS measurement in the *n*-dopable region. (e) Raman spectroscopy measurements for the  $\text{ClO}_4^-$  doped bipolar porous organic electrode (indicated as I), 1M  $\text{NaClO}_4$  in propylene carbonate (indicated as II), and propylene carbonate (indicated as III). (f) FT-IR measurements for I, II, and III.

This Raman-active  $\nu_1$  mode and the signals from PC were not detected in I which means that there is no residual electrolyte in I. In Fig. 5-18f, which shows the FT-IR spectra, the peak 2B in I ( $881 \text{ cm}^{-1}$ ) is the infrared-active  $\nu_1$  mode for  $\text{ClO}_4^-$  (Ref. 211 and 214). The infrared-inactive  $\nu_1$  mode becomes infrared-active due to destruction of the symmetry by the co-ordination to host compounds. In our case, the destruction of the symmetry is induced by the electrochemical *p*-doping, which creates a coordination of  $\text{ClO}_4^-$  to the BPOE. The peaks assigned as 1' in II and III (Fig. 5-18f) originates from propylene carbonate (PC). The peak 3 in I (Fig. 5-18f) can be assigned to aromatic C–H out-of-plane bend or 1,4-disubstituted benzene rings in the BPOE (Ref. 134). From these spectroscopy measurements, the doped  $\text{ClO}_4^-$  state in

the BPOE was observed. Thus, the results of the FT-IR and Raman spectroscopy measurements clearly reveal the successful *p*-doping of ClO<sub>4</sub><sup>-</sup> in the BPOE. Based on this bipolar feature of the BPOE, one can achieve a large working potential window (4.1–1.3 V versus Na/Na<sup>+</sup>) which can increase the energy density by giving a high specific capacity. Moreover, its porous morphology results in a high rate capability due to fast ion-transport by the electrolyte filled porous framework (Fig. 5-17a,b).

In Fig. 5-19a, the charge-discharge curves for the BPOE in a rechargeable sodium battery system are shown at various current densities ranging from 0.01 A g<sup>-1</sup> to 5.0 A g<sup>-1</sup> in a working potential of 1.3–4.1 V versus Na/Na<sup>+</sup>. This sloping nature of the charge-discharge curves could be related to the 2D structure and defects in the structure due to the short-range-ordered structure of the BPOE which results in a different electronic structure compared to the bulk material and affects the electrochemical properties<sup>215–217</sup>. The initial OCV is ~2.8 V versus Na/Na<sup>+</sup>, and hence, the *p*-dopable and *n*-dopable regions are above and below 2.8 V versus Na/Na<sup>+</sup>, respectively. 1M NaClO<sub>4</sub> in propylene carbonate (PC) was used as an electrolyte due to its high stability in the Na-ion battery system<sup>187</sup>. For a high current density of 5 A g<sup>-1</sup>, the BPOE can provide a specific capacity of ~50 mAh g<sup>-1</sup>. To calculate the approximate values for the doping of Na<sup>+</sup> and ClO<sub>4</sub><sup>-</sup>, C<sub>24</sub>N<sub>6</sub>H<sub>12</sub> (molecular weight of 384.09 g mol<sup>-1</sup>, here referred to as BPOE) was referred as the unit cell of the BPOE. The two redox reactions can then be defined as:



for a potential range of 4.1–2.8 V versus Na/Na<sup>+</sup>: i.e. the *p*-dopable region, and:

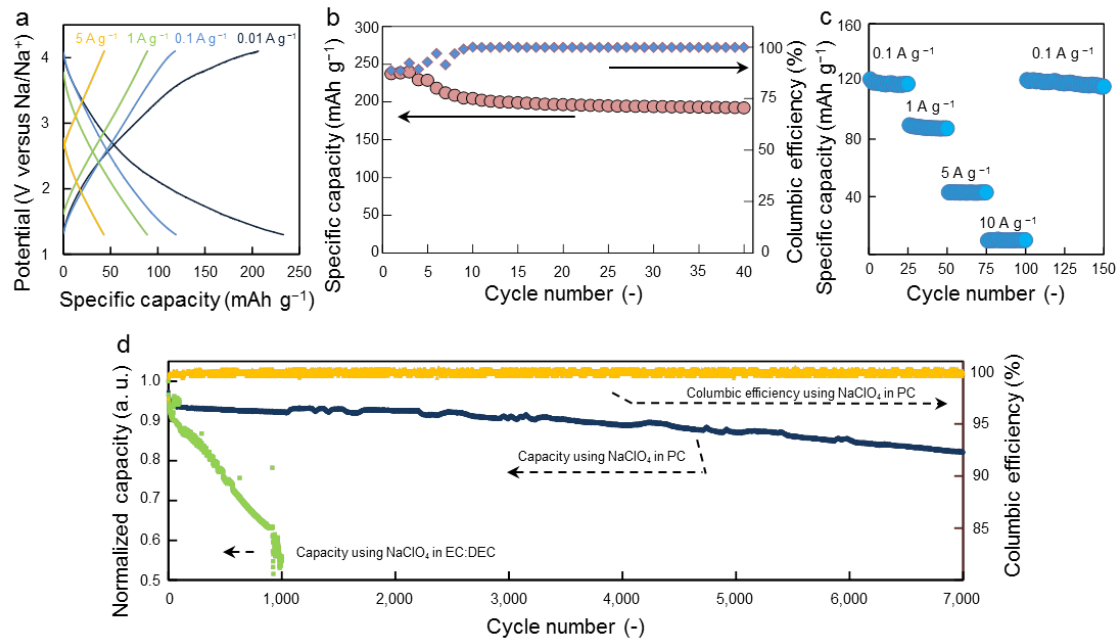
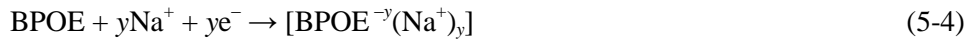


**Figure 5-19 | Cycle and rate performance of BPOE.** (a) Charge-discharge curves of a sodium-organic energy storage device at various current densities. (b) Cycle performance of a sodium-organic energy storage device at a current density of  $0.01 \text{ A g}^{-1}$ . (c) Cycle performance of a sodium-organic energy storage device under harsh conditions. (d) Cycle performance of a sodium-organic energy storage device up to 7,000 cycles with comparing the effect of electrolytes.



for the potential range of 2.8–1.3 V versus  $\text{Na}/\text{Na}^+$ : i.e. *n*-dopable region

A discharge capacity of  $55 \text{ mAh g}^{-1}$  (*p*-undoping) was obtained at a very low current density of  $0.01 \text{ A g}^{-1}$  (Fig. 5-19a) for equation (1) in the *p*-dopable region ( $> 2.8 \text{ V}$  versus  $\text{Na}/\text{Na}^+$ ), resulting in  $x = 0.79$  from equation (1) and a specific discharge capacity of  $185 \text{ mAh g}^{-1}$  (*n*-doping) was obtained (Fig. 5-19a) for equation (2) in *n*-dopable region ( $< 2.8 \text{ V}$  versus  $\text{Na}/\text{Na}^+$ ), yielding  $y = 2.65$  from equation (2).

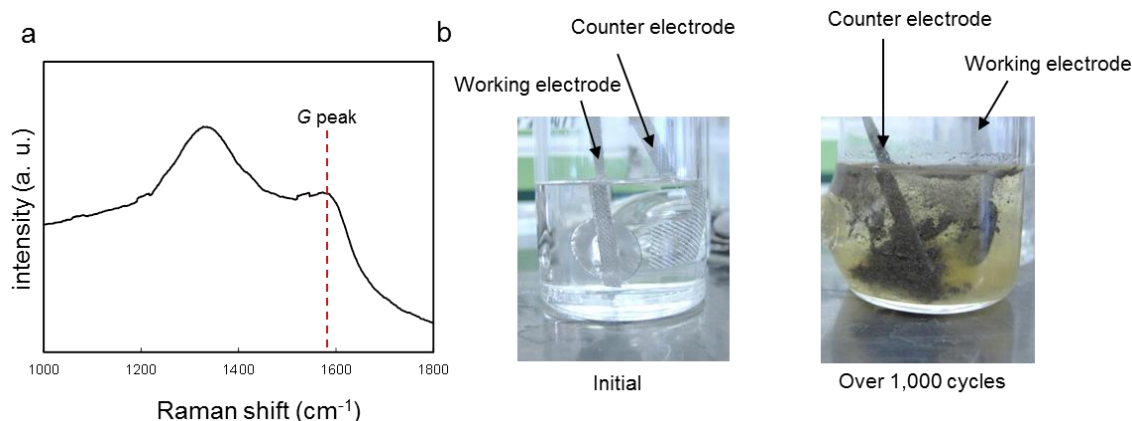


**Figure 5-20 | Characterization of BPOE after electrochemical measurements.** (a) Raman spectrum of the BPOE after 7,400 cycles. The existence of G peak even after 7,400 charge-discharge cycling reveals the high stability of the 2D framework of the BPOE. (b) Picture of the sodium-organic energy storage device after 1,000 cycles using 1M NaClO<sub>4</sub> in EC:DEC as an electrolyte. Initial (left) and after over 1,000 cycles (right).

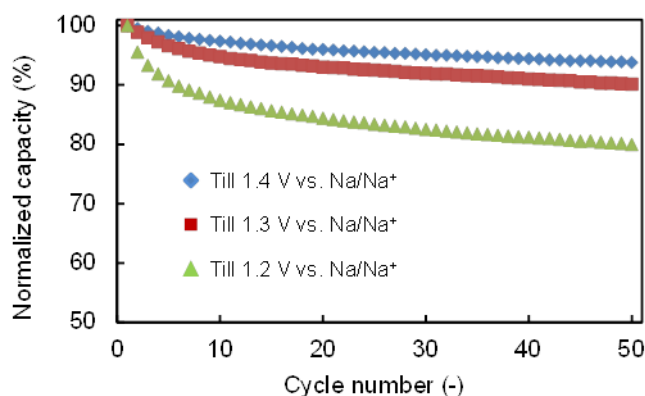


**Figure 5-21 | Comparison of electrochemical properties of Na/1M NaClO<sub>4</sub> in PC/BPOE cells in different discharge depth.**

The cycle performance of the BPOE was checked at a range current densities, from a very low current density of 0.01 A g<sup>-1</sup> up to a high current density of 5.0 A g<sup>-1</sup> revealing quite good cycle stability (Fig. 5-19a-c): at a current density of 0.01 A g<sup>-1</sup>, the BPOE shows a specific capacity of ~200 mAh g<sup>-1</sup> based on the mass of the BPOE and a stable cycle performance (Fig. 5-19b). Even under harsh conditions (25 cycles at different current densities

from 0.1 A g<sup>-1</sup> to 5.0 A g<sup>-1</sup> without relaxation between the cycles), the BPOE reproduces a stable specific capacity of ~120 mAh g<sup>-1</sup> at 0.1 A g<sup>-1</sup>, retaining the same specific capacity as in the first 25 cycles at 0.1 A g<sup>-1</sup> (Fig. 5-19c). Moreover, BPOE has been tested over 7,000 cycles with 80 % capacity retention at a high current density of 1.0 A g<sup>-1</sup> (Fig. 5-19d). Raman spectra of the electrode after 7,400 charge-discharge cycles provide further evidence of the stability of the 2D framework by showing the *G* peak (Fig. 5-20a).

The importance of the selection of the electrolyte is evident by comparing two different electrolytes for the cycle stability test. Both 1M NaClO<sub>4</sub> in ethylene carbonate (EC): diethylene carbonate (DEC) (1:1) and 1M NaClO<sub>4</sub> in PC were reported as stable electrolytes for the Na-ion battery system up to 100 cycles<sup>187</sup>. In contrast to 1 M NaClO<sub>4</sub> in PC, the cell with 1M NaClO<sub>4</sub> in EC:DEC begins to show a degradation from about 200 cycles. The reason for the performance degradation may be due to a reaction of the BPOE with the organic solvents and Na<sup>+</sup>; solid products which were observed to form on the counter electrode (Na metal) for the cells which used 1 M NaClO<sub>4</sub> in EC:DEC as electrolyte (Fig. 5-20b). This dramatic difference in cycling stability suggests that PC is one of the most stable organic solvents for Na-ion battery systems of this configuration.

The main difference between Na//BPOE (this section) and Li//BPOE (section 5.3.) cells is the cycling stability in the *n*-doping process (Fig. 5-21). In case of Li//BPOE, this cell shows a stable cycling even in a low potential until 1.0 V vs. Li/Li<sup>+</sup> (= 0.7 V vs. Na/Na<sup>+</sup>). However, in case of Na//BPOE, this cell shows stable cycling until a lower potential of 1.3 V vs. Na/Na<sup>+</sup> (= 1.6 V vs. Li/Li<sup>+</sup>), but a fast degradation of the specific capacity if one apply a potential window until 1.2 V vs. Na/Na<sup>+</sup> (= 1.5 V vs. Li/Li<sup>+</sup>) as shown below (a current density is 0.1 A g<sup>-1</sup>). This result suggests that Li<sup>+</sup> could show a better cycle property in wider working potential compared to the application of Na<sup>+</sup>.

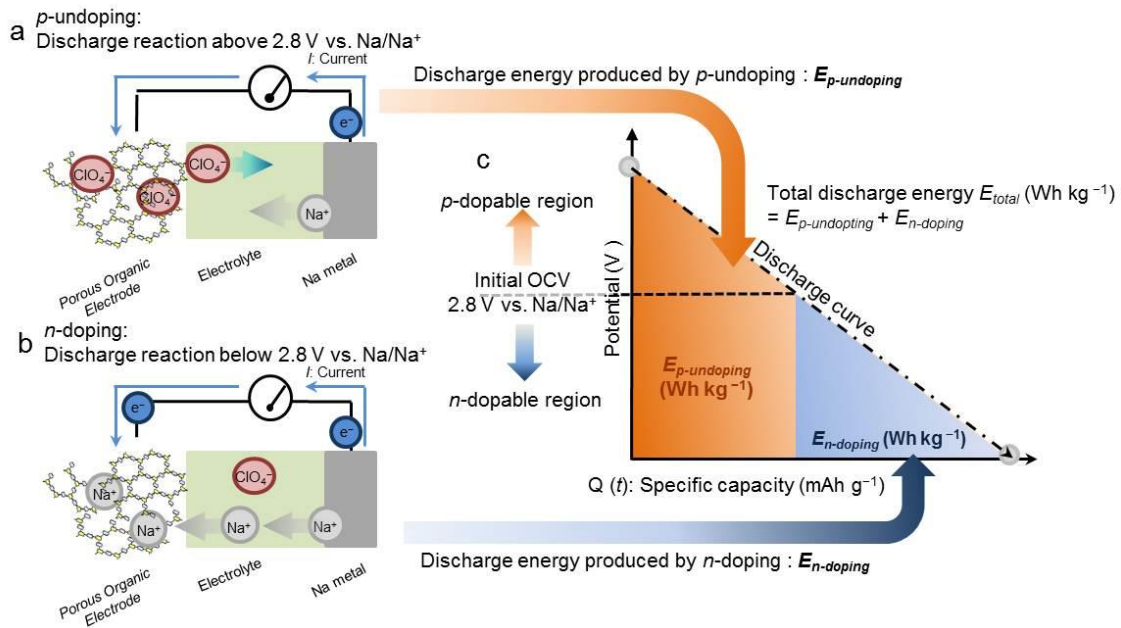


**Figure 5-22 | Energy storage principle of the BPOE at discharge process.** (a) *p*-undoping for the discharge process (at the potential above the initial open-circuit voltage (OCV)) of the BPOE. Electrons are extracted from the anode and are injected into the BPOE. Both anion ( $\text{ClO}_4^-$ ) and cation ( $\text{Na}^+$ ) will travel back to the electrolyte during the *p*-undoping discharge process to maintain electrical neutrality. (b) *n*-doping for the discharge process (at the potential below the initial OCV) of the BPOE. Electrons are extracted from the anode and are injected into the BPOE.  $\text{Na}^+$  will be doped into the BPOE during the *n*-doping discharge process to maintain electrical neutrality. (c) Summary of the discharge process of energy storage device using a BPOE which is linearly, continuously connected *p*-dopable and *n*-dopable region. The total specific energy  $E_{total}$  ( $\text{Wh kg}^{-1}$ ) can be calculated by summing the specific energy obtained during *p*-undoping  $E_{p-undoping}$  ( $\text{Wh kg}^{-1}$ ), indicated by the red area, and the specific energy obtained during *n*-doping  $E_{n-doping}$  ( $\text{Wh kg}^{-1}$ ), indicated by the blue area.  $E_{total} = E_{p-undoping} + E_{n-doping}$  can be calculated by:  $E_{total} = \int Q(t)V(t)dt$  where  $Q(t)$  ( $\text{mAh g}^{-1}$ ) = constant current density  $I_0$  ( $\text{mA g}^{-1}$ )  $\times t$  (h), is the specific capacity,  $t$  (h) is the discharge time, and  $V(t)$  is the potential.

In Fig. 5-22a-c, the discharge process based on the energy storage principle of a bipolar porous organic electrode (BPOE) are shown. The unique points of the BPOE are: 1) this material can be used as a cathode, 2) BPOE is a bipolar material which has a *p*-dopable region above the initial open-circuit voltage (OCV) and a *n*-dopable region below the initial OCV, and 3) its *p*-undoping process (Fig. 5-22a) and *n*-doping process (Fig. 5-22b) can be continuously

and linearly connected<sup>134</sup> (Fig. 5-22c). Therefore, one can expect a higher energy density from the BPOE due to a wide working potential compared to a material having only the *p*- or *n*-dopable property.

The electrochemical property of the porous organic electrode in half-cells is compared to other proposed electrode materials in a Ragone plot (Figure 5-23a) and the round-trip energy efficiency (Figure 5-23b). Our porous organic electrode exhibits a specific energy of ~500 Wh kg<sup>-1</sup> and a specific power of 10 kW kg<sup>-1</sup> (Figure 5-23a) where the weight is based on the mass of BPOE. Promisingly, the volumetric energy is ~250 Wh L<sup>-1</sup> (the calculated crystal density of the BPOE is 0.5108 g cm<sup>-3</sup>), which may be favorably compared to Lead–acid or Ni–Cd batteries with a specific volumetric energy of ~100 Wh L<sub>cell</sub><sup>-1</sup> in full cells. The volumetric energy (Wh L<sup>-1</sup>) of Lead–acid and Ni–Cd in full cells is distributed around 100 Wh L<sub>cell</sub><sup>-1</sup>. Here, the volumetric energy of the BPOE is ~250 Wh L<sup>-1</sup> considering only the mass of the BPOE. If one assume that the volume of BPOE constitutes 40 % of total volume of a sodium–organic energy storage device, this full cell will provide ~100 Wh L<sub>cell</sub><sup>-1</sup> which is as good as for other rechargeable batteries, such as Lead–acid and Ni–Cd batteries. This result is highly promising. For example, sodium-sulphur (NAS) batteries (indicated as a yellow region in Figure 5-23a) are a promising energy storage device for stationary electricity storage uses<sup>176,178</sup>. NAS batteries have a theoretical specific energy of 975 Wh kg<sup>-1</sup> for the following reactions (equation (5-5), a theoretical specific capacity of 487 mAh g<sup>-1</sup> with an average cell voltage of ~2 V):



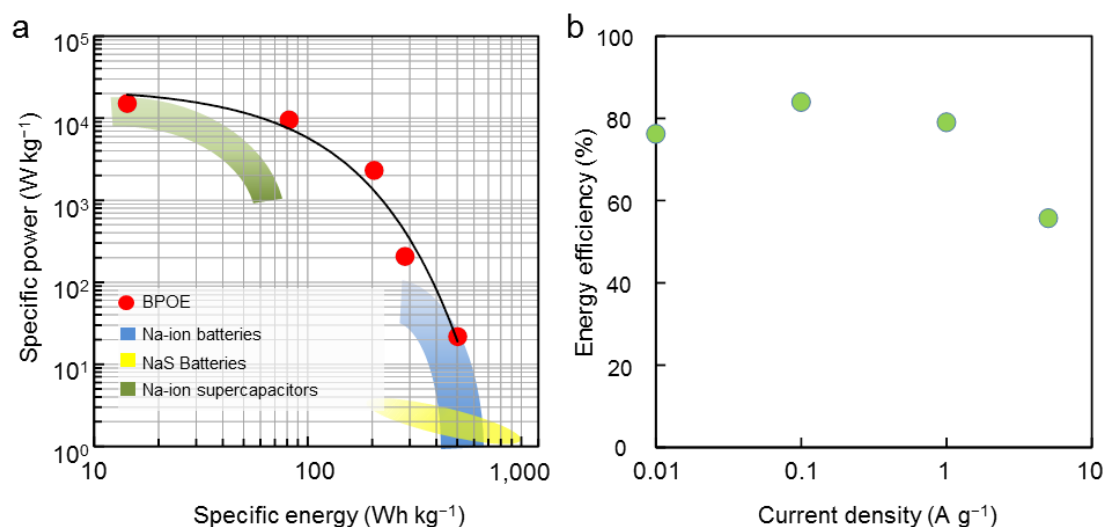


**Figure 5-23 | Ragone plots and round-trip energy efficiency of sodium-organic energy storage**

**device.** (a) Ragone plots for a sodium-organic energy storage device using a BPOE and various sodium-based energy storage devices in half-cells. The specific energy was calculated on the basis of the half-cells using sodium metal as an anode. (b) Round-trip energy efficiency of the sodium-organic energy storage device.

However, this system has safety problems due to its high operation temperature of 300–350 °C (ref. 176). Indeed, full cells can provide much less specific energy due to limited practical cell configurations related to this safety problem. In contrast, the porous organic electrode at room-temperature can be operated with a specific energy comparable to NAS batteries. Also, this system shows a longer cycle life of 7,000 cycles compared to 4,500 cycles for NAS batteries and the energy efficiency of the BPOE is ~80 % (Fig. 5-23b) which is comparable to 85 % of NAS batteries (Ref. 176), and higher than ~70 % of redox-flow batteries<sup>218</sup>. However, the self-discharge characteristic of the NAS and Sodium-ion batteries based on the intercalation mechanism are better than those of the BPOE electrodes (Fig. 5-23a). These issues could be improved by optimization of electrode assembly processes and further fundamental investigations of the BPOE, especially on the energy storage mechanism. The key point is that the porous organic electrode has a remarkably high specific power of 10 kW kg<sup>-1</sup>; a



performance which is not yet reached by Na-ion batteries. These properties of the BPOE are comparable to O3-type  $\text{NaNi}_{0.5}\text{Mn}_{0.5}\text{O}_2$  (ref. 187) and P2-type  $\text{Na}_x[\text{Fe}_{1/2}\text{Mn}_{1/2}]\text{O}_2$  (ref. 189), which are performed as state-of-the-art high performance cathodes for Na-ion batteries, and are much higher than for other intercalation compounds such as fluorophosphates<sup>181,182</sup>, NASICONs<sup>185</sup>, and olivines<sup>186</sup>. By combining state-of-the-arts anodes<sup>196,219,220</sup>, and electrolytes, such as ionic liquids<sup>221</sup> or  $\text{NaPF}_6$  in EC: PC (ref. 222), the safety problem, which is one of the most important points for any practical technology, of a sodium-organic energy storage device could be improved.

#### 5. 4. 3. Conclusion for sodium-organic energy storage device

**I**n summary, the excellent electrochemical performance of a porous organic electrode for sodium-based energy storage devices has been demonstrated with even having compared with other sodium battery systems, and it is, therefore, a promising material for next-generation energy storage devices. This is, to the best of our knowledge, the first report of a high-performance sodium-based energy storage device using an organic cathode. Bipolar porous polymeric frameworks are a new material platform to develop alternative, high-performance rechargeable energy storage devices by using cost-effective and abundant organic materials.

## 5. 5. ALL-ORGANIC ENERGY STORAGE DEVICE

### 5. 5. 1. Introduction

BPOEs, porous polymeric frameworks constituted of benzene, as an electron donor, and triazine rings, as an electron acceptor, have been used in a new energy storage principle in last sections. Redox active organic materials are often categorized in carbonyl, radical, or organosulfur compounds.<sup>62</sup> However, BPOE is an aromatic compound comparable to porous graphene.<sup>134</sup> The further study on the redox-active aromatic compounds<sup>149,195</sup> could pave the way for the further development of organic energy storage devices. From the perspective of the industry, BPOE has a potential to become an affordable and high-performance battery since they show both high specific power and energy. Suga *et al.* demonstrated a simple, symmetric all-organic battery with an intercalation mechanism by using a new bipolar radical polymer<sup>195</sup>, and most recently all-organic batteries using bipolar polyparaphenylene were reported<sup>223</sup>. The features of BPPFs would be a promising strategy for the further improvement of all-organic batteries. The BPPFs have the following advantages for use as an electrode material and a cell fabrication procedure: (I) a high specific power due to rapid ion transport by a porous nature, (II) a long battery life due to the high stability of the framework, (III), a simple, safety and low-cost configuration by using same organic materials for a cathode and an anode. Hence, the BPPFs both in cathode and anode provide a safety, high-performance and long-life all-organic battery.

Here, affordable all-organic batteries using BPOEs are shown. They can provide a specific energy of 34 Wh kg<sup>-1</sup> and a specific power of 1 kW kg<sup>-1</sup> based on total mass of the BPOE with a cycle-life of over 1000 times.

### 5. 5. 2. Results and discussion

Fundamental electrochemical characteristics of all-organic lithium batteries using the BPOEs are studied by investigating charge-discharge properties. The electrodes were prepared and were characterized as same as previous sections (see 5.2. for the details.). The weight of active materials in each electrode was fixed to be equal. Charge-discharge profiles at various current densities from  $0.05 \text{ A g}^{-1}$  to  $2 \text{ A g}^{-1}$  in the working potential of  $0.0 - 3.5 \text{ V}$  are shown in Fig. 5-24a. At a constant current density of  $0.05 \text{ A g}^{-1}$ , the all-polymer system shows a specific capacity of  $\sim 65 \text{ mA h g}^{-1}$  based on the total mass of BPOE with a sloping voltage profile. If one calculate the amount of the adsorbed  $\text{Li}^+$  into the BPOE ( $= x$  in eq. (5-6), (5-7) and (5-8)),  $x$  is  $\sim 1.86 \text{ mol}$ . The unit cell was defined by  $\text{C}_{24}\text{N}_6\text{H}_{12}$ , which has a molecular weight of  $384.09 \text{ g mol}^{-1}$ ). This result also suggests that our battery system uses  $1.86 \text{ mol}$  of the electrolyte for  $1 \text{ mol}$  of the CTF-1 at the current density of  $0.05 \text{ A g}^{-1}$  (eq. (5-8)). Under high rate condition of  $2.0 \text{ A g}^{-1}$ , our system shows a specific capacity of  $\sim 17 \text{ mA h g}^{-1}$ . The stability of the battery in high rates and a long charge-discharge cycle are shown in Fig. 5-24b and Fig. 5-24c, respectively. Even after the cycling at high rate condition, the all-organic battery using the BPPF shows again the stable cycling (Fig. 5-24b). Moreover, this battery system shows excellent cycle performance up to 1000 cycles at the current density of  $1.0 \text{ A g}^{-1}$  (Fig. 5-24c). These two results reveal the remarkable property of BPOE-based battery both in rate performance and long cycle life.

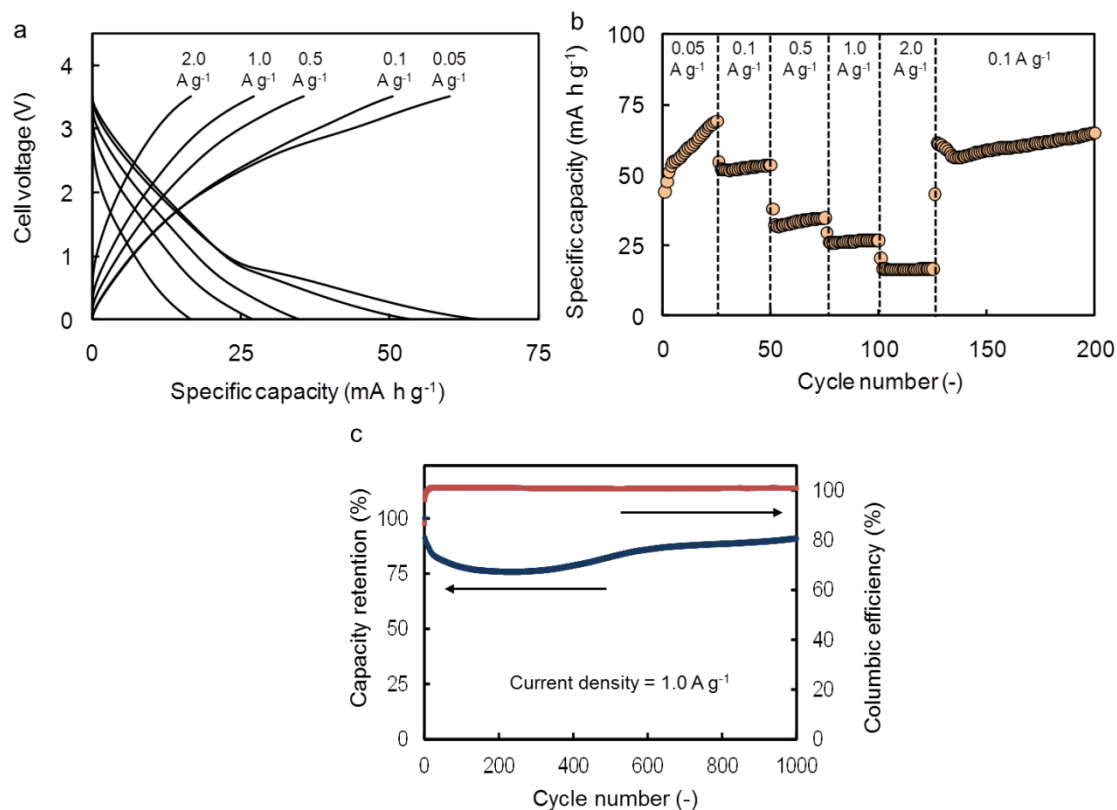


**Figure 5-24 | Electrochemical characterization of all-organic batteries.** (a) Charge-discharge profiles of all polymer batteries, (b) cycle performance of all-organic batteries, and (c) cycle life and coulombic efficiency of all-organic batteries.

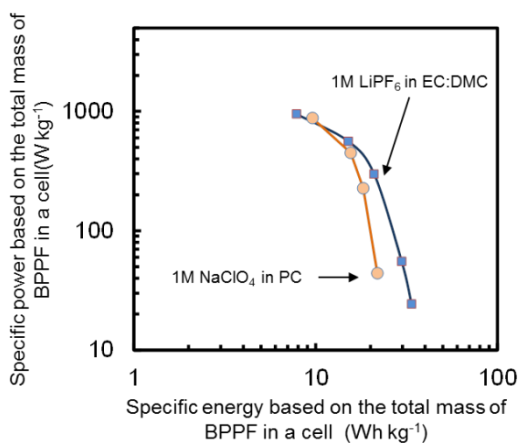


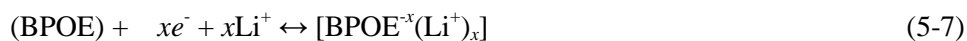
**Figure 5-25 | Ragone plots of all-organic batteries.**

The comparison of specific power and specific energy (Ragone plot) of the BPOE based all-polymer battery is shown in Fig. 5-25. For instance, other organic battery systems, such as Poly(3-methylthiophene)-based polymer supercapacitor showed a specific energy of 13 Wh kg<sup>-1</sup> and specific power of 1.4 kW kg<sup>-1</sup> based on the total mass of the polymer.<sup>224</sup> The poly(nitronylnitroxylstyrene)-based bipolar polymer battery,<sup>175</sup> which works with an intercalation mechanism, exhibited a specific energy of 57.2 Wh kg<sup>-1</sup> based on the total mass of the polymer. Our energy storage device shows comparable electrochemical properties to these all-polymer energy storage devices using already sophisticated redox-active polymers. Our all-polymer battery will provide a specific energy of 34 Wh kg<sup>-1</sup> and a specific power of 1 kW kg<sup>-1</sup> based on total mass of the BPOE, which is both high specific power and energy as all-organic energy storage device (Fig. 5-25).

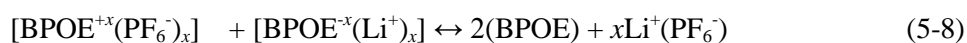
Based on our former study, the electrical energy storage reaction of BPOE is shown below. The reaction at the electrodes is expected to be based on the oxidized (*p*-doped) state of benzene rings (electron donor) in BPOE which is formed by C<sub>24</sub>N<sub>6</sub>H<sub>12</sub> (= 384.09 g mol<sup>-1</sup>):



and to be based on the reduced (*n*-doped) state of triazine rings (electron acceptor):



Therefore, from eq. (5-6) and eq. (5-7), the net reaction could be:



To describe the electrochemical reaction at the all-organic energy storage device, a cell constituting of two organic electrodes A and B is considered. First of all, the cell was charged up to 1.75 V, then an organic electrode A underwent the reaction eq. (5-6), which is *p*-doping reaction, and the other organic electrode B underwent the reaction eq. (5-7), which is *n*-doping reaction. During the discharge reaction, from 1.75 to 0 V, the electrochemical reaction at the electrode A is based on eq. (5-6), however, from 0 to -1.75 V, the electrochemical reaction at the electrode A becomes eq. (5-7), which is *n*-doping reaction. Thus, the cells show a cell voltage ranging from 0-3.5 V as described in Fig. 5-24a. By applying this energy storage mechanism, a stable cycle performance could be achieved due to a low doping state which gives a less stress compared to being a deep doping state in general.

Indeed, sodium can be applied for all-organic battery using BPOEs as charge carriers. Few researches have reported organic materials used in next-generation batteries, such as lithium-air batteries.<sup>225</sup> To best our knowledge, this is the first report about all-organic batteries using sodium as charge carriers. 1M Na(ClO<sub>4</sub>) in PC was used as an electrolyte for all-organic sodium batteries in a cell voltage region of 3 V. The electrochemical properties of all-organic batteries using sodium are as good as properties using lithium (Fig. 5-25). This could be explained that the *p*-doping reaction dominates the total electrochemical reaction due to less specific *p*-doping capacity compare to *n*-doping reaction. This lower capacity in *p*-doping reaction may result from larger anion compared to cations, such as Li<sup>+</sup> and Na<sup>+</sup>. Our sodium-based all-polymer batteries will provide a specific energy of 22 Wh kg<sup>-1</sup> and a specific power of 0.9 kW kg<sup>-1</sup> based on total mass of the BPPF. Recently, sodium-based batteries are of great interest due to its excellent affordability compared to lithium-based batteries. From this point of view, our result indicates that all-organic batteries using sodium as a charge carrier can be a serious candidate for an affordable energy storage device.

### 5. 5. 3. Conclusion for all-organic energy storage device

In conclusion, the BPOE-based all-organic battery demonstrated high-performance electrochemical properties with a simple configuration. These performances were achieved by the combination of the porous structure and unique electronic properties of the BPPFs. Moreover, the BPOE can be applied for sodium-based energy storage device. The study on BPPF will initiate a new strategy towards an extremely affordable, safety, high-performance all-organic energy storage device.

## **5. 6. ELECTRONIC STRUCTURES AND ELECTROCHEMICAL PROPERTIES OF POROUS POLYMERIC FRAMEWORKS**

### 5. 6. 1. Introduction

One of the most interesting properties pursued in organic electronics is bipolarity: existence of both *p*- and *n*-type semiconductors in the same material<sup>234</sup>. This feature is not only important from fundamental science but also for its possible industrial applications. Since the discovery of conductive polymers<sup>226,59,60</sup>, semiconducting conjugated polymers have been of great interest in organic electronics<sup>227,228</sup> applications, such as organic electro-luminescent diodes<sup>229–232</sup>, photovoltaic-cells<sup>233,234</sup>, photocatalyst polymers<sup>139</sup> and organic batteries<sup>61,62,166</sup>. The improvement of organic electronics is necessary towards a low-carbon society, thus reducing the risks associated to the present electronic technology based on rare metals<sup>235</sup>. Hence bipolar organic compounds are promising candidates to promote further development in the field of

organic electronics<sup>237</sup>. The discovery of bipolarity from a new class of organic material would foster future developments of the above mentioned technologies<sup>238</sup>. Indeed, recent works on  $\pi$ -conjugated microporous polymers show that polymeric frameworks are promising materials for organic electronics<sup>149,207</sup> and even for organic spintronics<sup>239</sup>. The experimental control of structural periodicities by choosing a monomer as the building block of the framework can lead to semiconducting systems with unique electronic properties, such as two-dimensional (2D) atomic crystals<sup>204</sup>. The possibility of controlling bipolar organic semiconductors electronic properties can give rise to new electronic system-level design<sup>238</sup> based on artificial semiconducting polymeric frameworks, resulting in a giant leap in the development of organic electronic devices.

Here, in this section, the electronic properties of covalent triazine-based frameworks<sup>141</sup> (CTFs) was studied by performing electrochemical measurements and comparing with first principle calculations. The CTFs are porous polymeric frameworks formed by cyclotrimerization of nitrile monomers, which have been applied in the implementation of catalyst materials<sup>154,241</sup>, and most recently for lithium- and sodium-based energy storage devices<sup>134,135</sup>. They have a conjugated structure in nature, consisting of benzene ring as electron donors and triazine rings as electron acceptors (Fig. 5-16a), with controllable photoluminescent properties<sup>242</sup>. Despite the above mentioned properties, to the best of our knowledge, little work has been done in the study of CTFs towards an efficient implementation in organic electronics. In our previous work, several electrochemical measurements were carried out to test the electrochemical properties of electrode materials, such as CTFs<sup>134,135</sup>. From these experiments, important information about the electronic structure of materials<sup>215-217</sup> can be obtained.



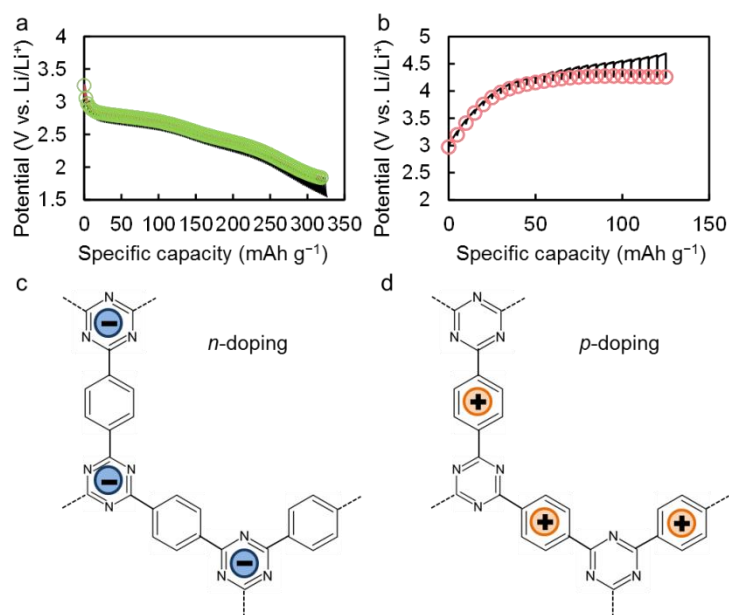


**Figure 5-26** | (a) OCV curve at *n*-doping. (b) OCV curve at *p*-doping. (c) Schematic illustration of *n*-doping at triazine rings (acceptor). (d) Schematic illustration of *p*-doping at benzene rings (donor). (a) and (b) were measured by same material, method and condition to Fig. 5-7b,c. Thus results are same if we compare these figures. However, the author carried out same experiments and shows again these figures to make readers understand this section easier.

Thus, electrochemical techniques were applied in the present work electrochemical techniques to observe tunable electronic properties of porous polymeric frameworks as an organic semiconductor, combined with a theoretical study of the density of states for two CTF compounds.

## 5. 6. 2. Results and discussion

Open-circuit voltage (OCV) ( $=E_{OCV}$ ) curves were measured through galvanostatic intermittent titration technique (GITT) to investigate the quasi-equilibrium states<sup>32,243</sup> of CTF-1 (Fig. 5-26a,b and see the 5.2. for the experimental procedures).

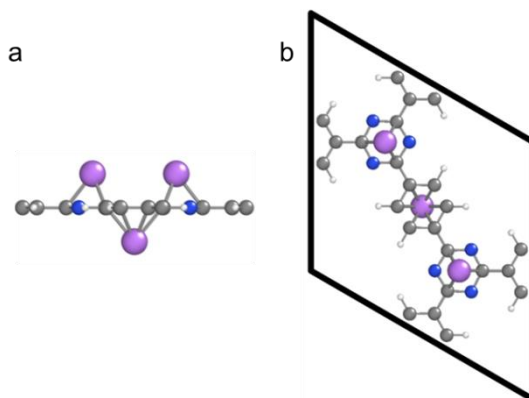


**Figure 5-27 | Simulation on the coordination of  $\text{Li}^+$  on CTF-1.** (a) Side view, and (b) Top view showing the unit cell of CTF-1,  $\text{C}_{24}\text{N}_6\text{H}_{12}$ .

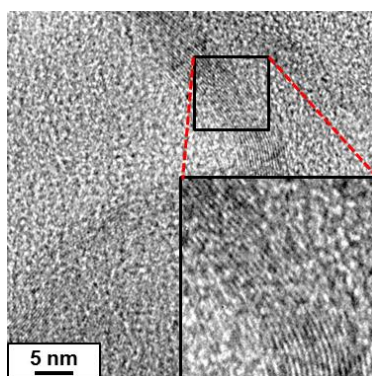


**Figure 5-28 | HRTEM image of CTF-1.**

The bipolarity observed in this material is derived from the electron-donor and electron-acceptor character of the benzene and triazine rings, respectively<sup>134,141</sup>. Thus, CTF-1 can have both a *n*-doped state (negatively charged state; Fig. 5-26c) and a *p*-doped state (positively charged state; Fig. 5-26d). It has been suggested in previous electrochemical measurements on the porous polymeric frameworks as electrodes with  $\text{LiPF}_6$  in ethylene carbonate/dimethyl carbonate (1:1) as the electrolyte that  $\text{Li}^+$  and  $\text{PF}_6^-$  are coordinated with CTFs based on a redox mechanism<sup>134</sup>.

Electrochemical properties of polymeric frameworks as electrodes are directly connected with their electronic structures<sup>244,245</sup>. For the *n*-doping process ( $\text{Li}^+$  reaction), a plateau at  $\sim 2.7$  V vs.  $\text{Li}/\text{Li}^+$  and following sloping curve in a discharge curve were found (Fig. 5-26a). The slope of this OCV curve is different from the ones obtained for typical intercalation compounds, which show a plateau followed by a sharp drop in the potential<sup>216</sup>. In the *p*-doping process ( $\text{PF}_6^-$  reaction), a plateau at  $\sim 4.2$  V vs.  $\text{Li}/\text{Li}^+$  was observed (Fig. 5-26b). Although the details of the energy storage mechanism of porous polymeric frameworks are still unclear, previous works on the adatom of both cations and anions into graphite<sup>108,160,202,246,247</sup>, graphene<sup>160,202,246-248</sup>, and related materials suggest that the ions could be coordinated on the top of the aromatic rings, which serve as hosts (Fig. 5-27). This unique electrochemical reaction should correspond to the electronic structure of CTF-1. Based on the above discussion, the relation between the OCV measurements and the electronic structure of CTF-1 was described, by means of thermodynamics and statistical mechanics<sup>249</sup>. The potential given by OCV depends on the chemical potential,  $\mu$ , of the guest ( $\text{Li}^+$  and  $\text{PF}_6^-$ ), and it is described by Nernst equation as follows

$$E_{ocv} = \frac{-\mu}{e} \quad (5-9)$$

The lattice-gas model, in which each site of the lattice has two states, was considered: full or empty. Then, the occupancy of the guest sites,  $f(\varepsilon)$ , as a function of energy,  $\varepsilon$ , through the Fermi distribution can be defined<sup>217</sup>:

$$f(\varepsilon) = \frac{n(\varepsilon)}{N(\varepsilon)} = \frac{1}{1 + \exp\left(\frac{\varepsilon - \mu}{k_b T}\right)} \quad (5-10)$$

where  $N(\varepsilon)$  is the number of sites with energy  $\varepsilon$ , and  $n(\varepsilon)$  is the number of occupying Li ions.

From eq. 5-9 and eq. 5-10, the relation between  $n(\varepsilon)$  and  $E_{OCV}$  is derived:

$$n(\varepsilon) = \frac{N(\varepsilon)}{1 + \exp\left(\frac{\varepsilon + eE_{OCV}}{k_B T}\right)} \quad (5-11)$$

eq. 5-12 shows the integration of  $n(\varepsilon)$  over the entire energy range, giving us the number of intercalated Li ions in the polymeric framework,  $n$ .

$$n = \int_{-\infty}^{+\infty} \frac{g(\varepsilon)}{1 + \exp\left(\frac{\varepsilon + eE_{OCV}}{k_B T}\right)} d\varepsilon \quad (5-12)$$

Here, the distribution of the site energy as  $g(\varepsilon) = dN(\varepsilon)/d\varepsilon$  has been defined.

For ideal bulk electrodes, one finds a flat plateau in the OCV potential curves, due to the fact that all sites have a specific energy,  $\varepsilon_i$ , thus corresponding  $g(\varepsilon)$  to a delta function  $\delta(\varepsilon - \varepsilon_i)$  in eq. 5-12. In the case of anisotropic and/or disordered electrode materials, the value for the occupation energy is broadened:  $\Delta\varepsilon$ . This energy distribution for the sites of the guest is reflected on the change in the slope of OCV curves, where the steepness that is observed for ideal electrodes is reduced, resulting in smoother slopes. Thus, if one assumes a monolayer or completely disordered CTF-1, following eq. 5-12, one would expect a smooth slope OCV curve without any plateau. This can be understood from the modification of the electronic structure of CTF-1, due to both anisotropy and the existence of defects<sup>215-217</sup>. However, CTF-1 shows a plateau, which confirms that this polymeric framework is partially formed by an ordered multilayer structure (Fig. 5-28).

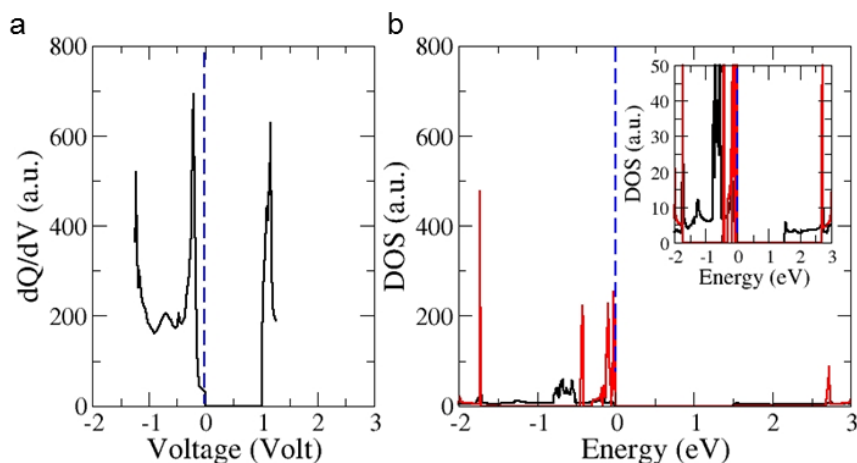


**Figure 5-29** | (a) Measurement of the DOS as a function of Voltage for the CTF-1. (b) Theoretical DOS for the ideal CTF-1 for the single layer (red) and the bulk case (black) obtained from ab initio calculation. The inset in (b) shows the enlarged part for bulk CTF-1 DOS. The Voltage (a) and Energy (b) are given respect to the Fermi Level (dashed blue line).

The distribution of the site energy can be obtained from the charge and discharge curves in the OCV measurements, giving us the density of states (DOS):  $g(\varepsilon)$ . From GITT technique, the DOS from the relation  $dQ/dE_{OCV}$ , where the capacity  $Q$  ( $\text{mAh g}^{-1}$ ) is the total quantity of electrons involved in the electrochemical reaction per unit cell, is obtained and  $dE_{OCV}$  (V) is determined by the number of sites with energy  $\varepsilon$ .

The experimental DOS (Fig. 5-29a) was calculated by analyzing the OCV curves (Fig. 5-26a,b and see Appendix A-2) for the CTF-1, which is formed by multilayer sheets (up to ~10 layers) of 2D polymeric frameworks (Fig. 5-27). Then, CTF-1 was studied through first principles calculations on a monolayer and a multilayer system, obtaining the theoretical density of states (Fig. 5-29b) for the 2D (red) and 3D (black) case. Due to the quasi-two dimensional character of CTF-1 multi-layered system, a direct comparison of the experimental band gap, ~1.4 eV, with the monolayer ~2.7 eV, and the multilayer gap, ~1.5 eV, is not relevant.

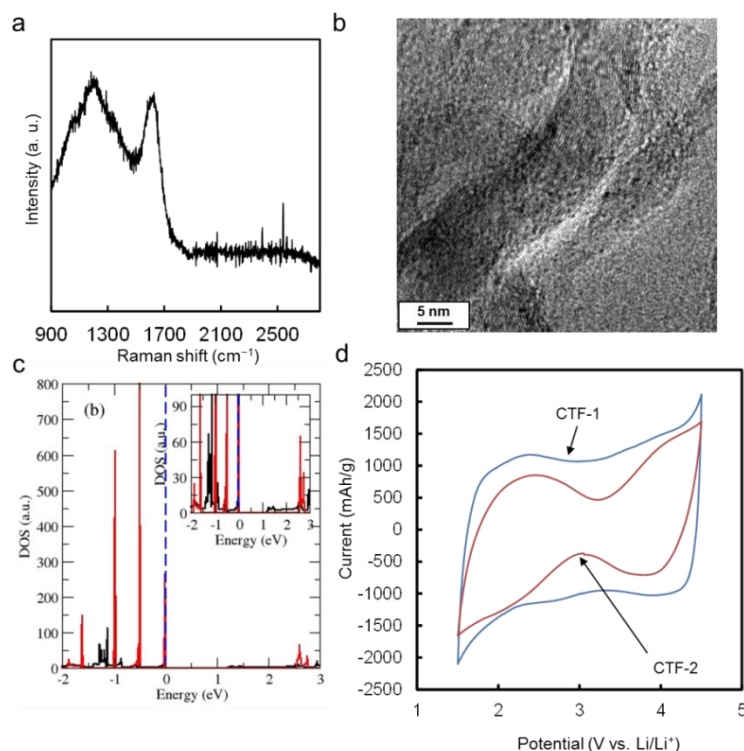


**Figure 5-30 | Characterization of CTF-2.** (a) Raman spectrum for CTF-2, (b) HRTEM image of CTF-2, (c) Theoretical DOS for the ideal CTF-2 for the single layer (red) and the bulk case (black), obtained from *ab initio* calculation. The inset shows the enlarged part for the bulk CTF-2 DOS. The Voltage and Energy are given respect to the Fermi Level (dashed blue line), and (d) Cycling voltammogram of CTF-1 and CTF-2.

Besides, one can analyze the main features in both DOS, noticing the existence of a large peak close to the Fermi level, which can indicate the existence of flat bands and charge localization.

One of the most important aspects in the study of CTFs is the ratio of the aromatic rings used in the synthesis process and how the electrochemical properties are affected by this. Then, a polymeric framework in which triazine and benzene rings have the ratio of 1:2 was synthesized (Fig. 5-30a,b: here, it is called as CTF-2, which was synthesized by polymerization of tris(4-cyanophenyl)benzene through an ionothermal synthesis method. See the ref. 141 for more details on CTF-2.). Also, the theoretical DOS from *ab initio* technique was calculated and

it was compared the results with the case of CTF-1. From (Fig. 5-30c) and (Fig. 5-29b), several peaks were observed in the density of states right below the Fermi level for CTF-1, while in the case of CTF-2, the peaks are shifted to lower energies. This indicates a more conducting behavior for CTF-1 when doping the system (holes) than for that of CTF-2. Indeed, the cyclic voltammetry (CV) measurements for CTF-1 and CTF-2 confirmed this result (Fig. 5-30d). While CTF-1 exhibited a continuous CV due to the larger peak-density in the DOS, CTF-2 clearly showed two separated redox reactions, due to its different electronic structure. From the latest comparison, it is concluded that tuning the electronic structure properties of CTFs is possible by either changing the periodicity of the frameworks or the aromatic rings in these systems.

### 5. 6. 3. Conclusion for electronic structures and electrochemical properties of PPFs

**I**n summary, the electronic structures of CTFs were investigated, by combining electrochemical experimental techniques and theoretical studies. These results revealed that the particular electronic structure of CTFs emerges from their structural periodicity and that their electronic properties can be controllable by changing the number of layers and the ratio of benzene and triazine aromatic rings. Therefore, covalent-triazine polymeric frameworks can lead to further development of organic semiconductors with tunable electronic properties, where band-gaps and doping properties can be controlled by combining the donor/acceptor character of the starting monomers in the synthesis of these frameworks.

## **5. 7. SUMMARY FOR THE CAPTER 5**

**I**n this chapter, the energy storage principle using polymeric frameworks were shown. The principle shows promising features towards energy storage based on Faradaic reactions. This principle enabled to use organic compounds in sodium-based energy storage devices even though almost organic compounds cannot use in the sodium cells in general. All-organic battery based on the polymeric framework suggested a possibility for extremely affordable energy storage devices. Finally, the study on polymeric frameworks' electronics structure showed indication towards further development of both polymeric framework as a new solid-state material and a group of energy storage material.



# CHAPTER 6. POROUS CARBON/SULFUR COMPOSITES TOWARDS HIGH-POWER LITHIUM-SULFUR CATHODES

## 6. 1. INTRODUCTION

Following contents are based on the ref. 250, which is one of the authors publication related to the PhD project. As already discussed, affordable batteries are key devices in the 21<sup>st</sup> century world where an efficient use of energy resources will be extremely important. The energy storage systems having high-energy and -power density were shown in previous chapters. Here, lithium-sulfur batteries (LSBs), an energy storage device having a super-large energy density, are focused.

The origin of LSBs can be found in a patent taken in 1962 by D. Herbert and J. Ulam,<sup>69</sup> and the basic configurations were suggested by M. L. B. Rao in 1968,<sup>70</sup> and D. Nole and V. Moss in 1970.<sup>250</sup> Compared to lithium-oxygen battery system, LSBs have lower energy density. However, since the finding of a practical approach to improve the electrochemical properties by L. F. Nazar and her co-workers in 2009,<sup>251</sup> LSBs attracted a lot of attention due to an easy configuration of cells and the abundance of sulfur as a natural resource. These advantages could push LSBs as a practical candidate for a battery having an energy density comparable to internal combustion engines.

Further improvements on LSBs from point of materials could be given by synthetic routes and morphological control of porous carbons. Especially, in spite of intense focus on the cycle performance, investigations on the development of power density have received less interest in the preceding studies. Hence, here a study on the improvement of LSBs' power density was carried out by using nanostructured hollow spheres delivered by biomass-precursors with hydrothermal synthesis.

## 6. 2. EXPERIMENT

### 6.2.1. Fabrication of carbon/sulfur composites

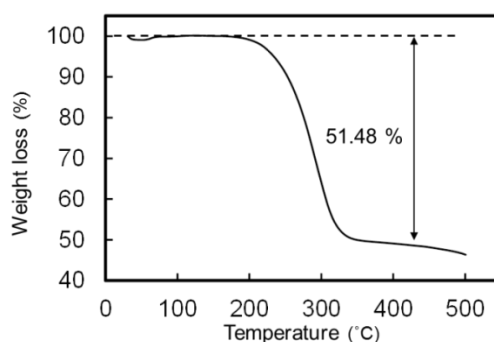


**Figure 6-1 | Thermal gravimetric analysis (TGA) for HSs/S composite.** TGA was carried out by using NETZSCH STA 409C/CD with heating ratio of 5 K min<sup>-1</sup>. [Ref. 252] Reproduced by permission of the PCCP Owner Societies.

Hydrothermal carbon-based hollow spheres were produced by Dr. N. Brun, L. Yu, and Dr. M.-M. Titirici at Max-Planck-Institute of colloids and interfaces. Two different samples, 950-CarbHS-G and 950-CarbHS-X, were prepared. The details about materials synthesis and characterizations are available in ref. 252. Carbon-based hollow nanospheres/sulfur composites (with a fixed carbon : sulfur weight ratio of 1:1, Fig. 6-1) were prepared by a melt diffusion

method. Carbon and sulfur were ground together and heated to 155 °C with heating rate of 20 °C h<sup>-1</sup> in Ar atmosphere.

#### 6.2.2. Electrochemical measurements for Li-S batteries

The electrodes were made by the C/S composite (90 wt%) and binder (polyvinylidene difluoride; 10 wt%). The two-electrode Swagelok-type cells were assembled in an argon-filled glove box and tested them on a multichannel potentiostatic-galvanostatic system (VMP-3, Bio-Logic) at 25 °C. Lithium metal was used as an anode and 1M LiTFSI in DOL:DME (1:1) was used as an electrolyte. Specific energy  $E$  (Wh kg<sup>-1</sup>) and specific power  $P$  (W kg<sup>-1</sup>) were calculated by the following method:  $E$  (Wh kg<sup>-1</sup>) can be calculated from  $E = \int_0^{t_{cut}} \frac{I_0}{m} V(t) dt$  where  $t_{cut}$  (hour) is the discharge time,  $I_0$  (A) is the constant current,  $m$  (kg) is the mass of active materials, and  $V(t)$  is the time-dependent voltage in the dimension of V. Specific power  $P$  (W kg<sup>-1</sup>) can be calculated by  $P = E / t_{cut}$ . To describe the Ragone plot, the mass of Li<sub>2</sub>S was adopted and was assumed that the mass of Li<sub>2</sub>S will comprise 25 wt% of the total device weight. The charge-discharge performances were measured in the potential range of 1.2–3.2 V versus Li/Li<sup>+</sup>.

## 6. 3. RESULTS AND DISCUSSION

Two main issues have to be overcome for the design of sustainable LSBs: (I) a low power density due to the bad electronic transport properties of the cathode because of the insulating nature of sulfur; and (II) the dissolution of intermediate polysulfides into electrolytes and the following shuttle-effect, involving a capacity fading and a worse coulombic efficiency<sup>71,251–256</sup>.

**Table 6-1** | Elemental analysis<sup>a</sup> and thermogravimetric measurements<sup>b</sup> performed on amino-functionalized silica templates, silica/carbon nanocomposites (950-Carb-X and -G) and carbon-based hollow spheres (550-CarbHS-X, 950-CarbHS-X and -G) after washing the composites twice overnight in a solution of ammonium hydrogen difluoride at 4 mol.%. [Ref. 252] Reproduced by permission of the PCCP Owner Societies.

Entry	Sample	C <sup>a</sup>	H <sup>a</sup>	N <sup>a</sup>	SiO <sub>2</sub> <sup>b</sup> (wt.%)
1	NH <sub>2</sub> -SiO <sub>2</sub> -90nm	3.15	1.84	1.74	89.34
2	550-CarbHS-X	86.88	3.38	0.49	3.15
3	950-Carb-X	-	-	-	71.69
4	<b>950-CarbHS-X</b>	<b>93.25</b>	<b>1.56</b>	<b>0.71</b>	<b>3.98</b>
5	950-Carb-G	-	-	-	74.06
6	<b>950-CarbHS-G</b>	<b>84.76</b>	<b>1.74</b>	<b>3.77</b>	<b>7.13</b>

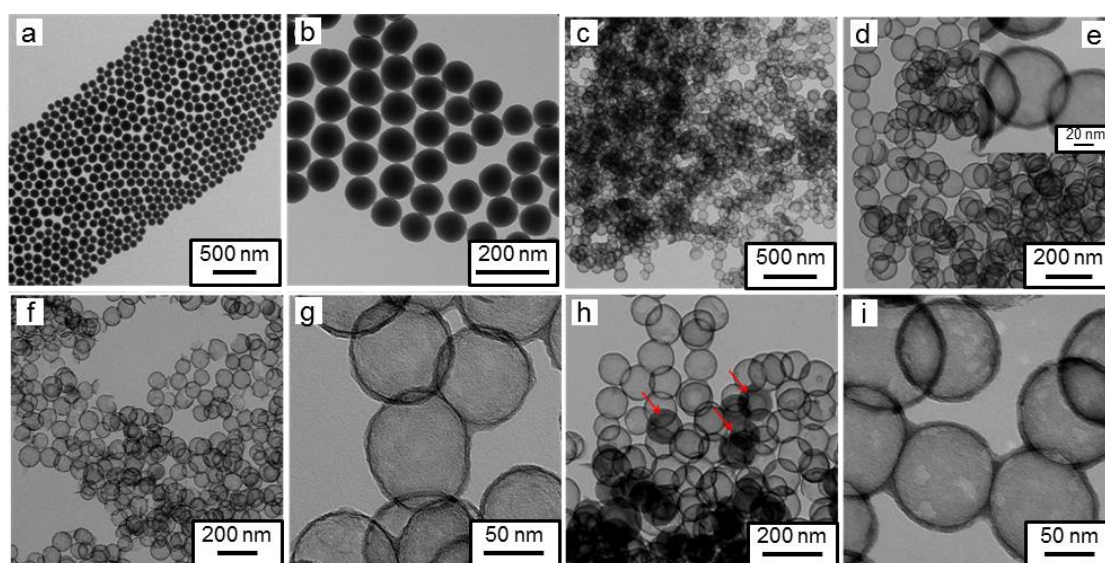


**Figure 6-2** | Micrographs obtained by transmission electron microscopy of (a-b) silica nanoparticles synthesized via a Stöber process, (c-e) carbon-based hollow spheres obtained after hydrothermal treatment at 180 °C in presence of xylose, pyrolysis at 550 °C and silica removal, 550-CarbHS-X and (f-g) carbon-based hollow spheres obtained after hydrothermal treatment at 180 °C in presence of xylose, pyrolysis at 950 °C and silica removal, 950-CarbHS-X. (h-i) Carbon-based hollow spheres obtained after hydrothermal treatment at 180 °C in presence of glucose, pyrolysis at 950 °C and silica removal, 950-CarbHS-G. Red arrows highlight the presence of residual silica within the carbon hollow spheres. [Ref. 252] Reproduced by permission of the PCCP Owner Societies.

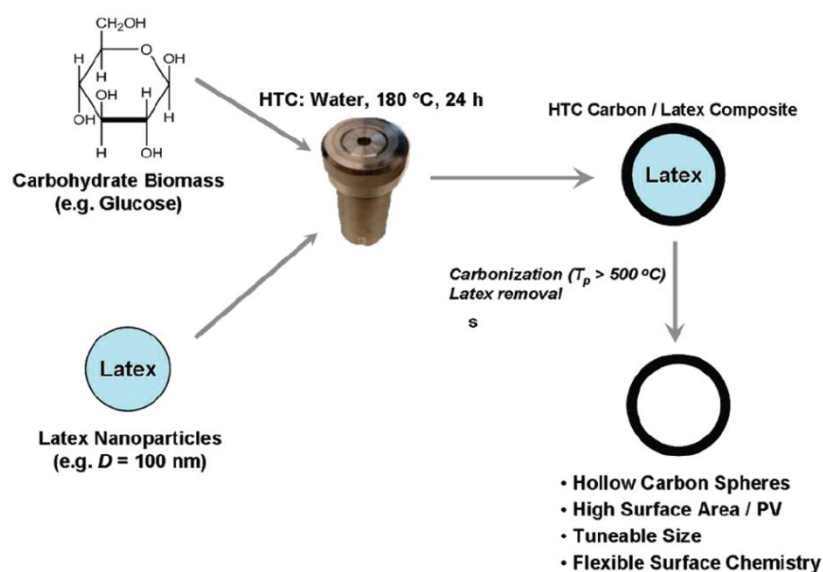


**Figure 6-3** | Schematic illustration for the example of synthesis of biomass-delivered carbon hollow sphere using templates. Reprinted with permission from (R. J. White *et al.*, *J. Am. Chem. Soc.* **2010**, 132, 17360). Copyright (2010) American Chemical Society.

The strategy developed in this work is to use the porous carbon hollow spheres (HS), which were suggested that one of the most promising porous carbons to be applied to LSBs,<sup>256,257</sup> presented beforehand to design nanostructured carbon HS/sulfur composites *via* a melt diffusion method, in such a way that: (i) the nanostructured conductive shells enhance the electronic transport properties due to a better electronic contact with sulfur,<sup>251,256</sup> increasing both the specific capacity and the rate capability; (ii) the HS having a porous-network prevents the dissolution of intermediate polysulfides into electrolytes, improving the charge-discharge cycle property and the coulombic efficiency. These two main features are expected to work co-operatively and lead to LIBs with high-performance electrochemical properties. First of all, two series of nanospheres exhibiting different shell nanostructures, depending on the monosaccharide used, have been prepared. The study presented herein focuses on the design of carbon-based hollow spheres through the use of 90 nm diameter Stöber silica nanoparticles (NPs) as hard-template and hydrothermally carbonized monosaccharides (i.e., glucose or

xylose) as carbon precursor (Fig. 6-3). After hydrothermal treatment for 20 h at 180 °C and further carbonization at 950 °C under inert atmosphere, thermogravimetric measurements emphasized Silica@Carbon composites made up of 83-85 wt% of NH<sub>2</sub>-SiO<sub>2</sub> and 15-17 wt% of carbon coating (Table 6-1 (Entries 1, 3 and 5)). After silica removal by etching, homogeneous carbon-based HS were obtained (Fig. 6-2c-i). The as-synthesized HS have an external diameter of 90-95 nm and an average carbon-shell thickness from 5 up to 8 nm, depending on the synthetic pathway. It appears that by using xylose as a carbon precursor, an increase in the further carbonization temperature from 550 to 950 °C leads to a decrease in the shell thickness from 7-8 (Fig. 6-2e) to 5 nm (Fig. 6-2g). At the same time, the internal diameter did not change (i.e., 80 nm), which is based on the fact that the silica template is thermally stable at 550 °C, thus the associated thermal shrinkage is negligible. Depending on the monosaccharide in use (glucose vs. xylose), a difference can be also observed (Fig. 6-2f-i). Indeed, considering the same experimental procedure and after further carbonization at 950 °C, it seems that hollow spheres made from glucose, 950-CarbHS-G, present a thicker carbon shell (about 7-8 nm, Fig. 6-2i) than their analogues made from xylose, 950-CarbHS-X (Fig. 6-2g).

All electrochemical properties were measured using cathodes with a fixed carbon:sulfur weight ratio of 1 : 1 and the specific capacities were calculated based on the mass of sulfur for the fundamental investigations. The assumed full-cell electrochemical properties of LSBs are shown in Figure 6-5b. Figures 6-4a and b show the 1st and 5th charge-discharge curves at a low current density of 0.1C (= 167.5 mA g<sup>-1</sup>) for the electrodes using 950-CarbHS-X and 950-CarbHS-G, respectively. Both carbon nanospheres showed a specific capacity of ~1300 mAh g<sup>-1</sup> at the 1st discharge which suggests an electrically well conductive carbon/sulfur network in the cathode.

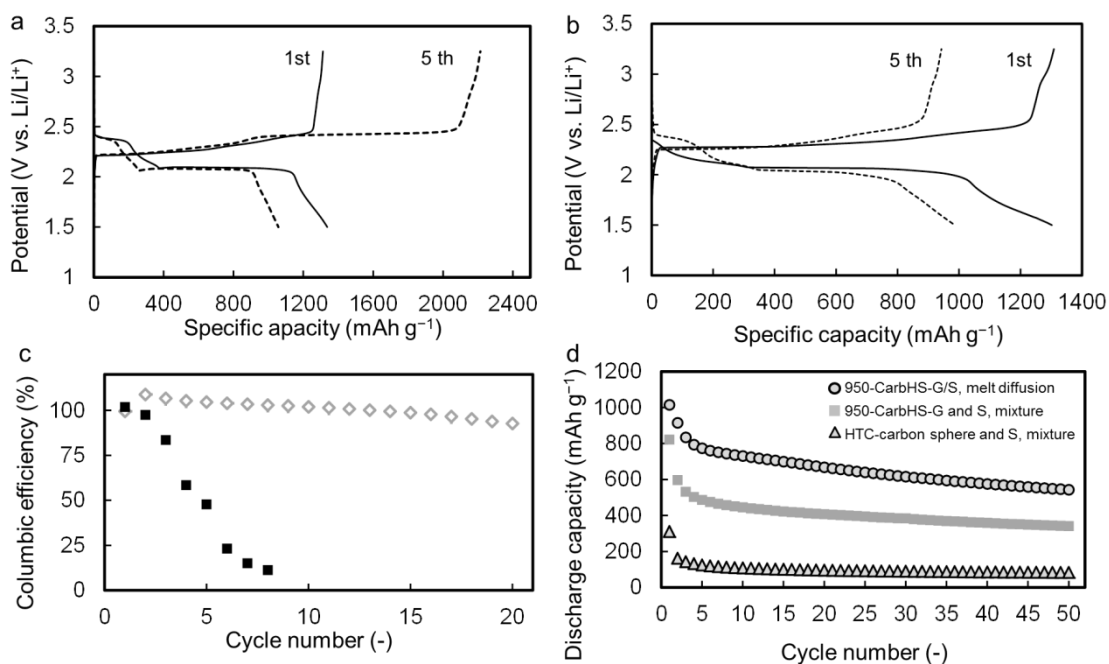


**Figure 6-4 | Electrochemical characterization of the two different carbon nanospheres.** (a)

Charge-discharge curves for electrodes using 950-CarbHS-X at a current density of  $0.1C$  ( $= 167.5 \text{ mA}\cdot\text{g}^{-1}$ ). (b) Charge-discharge curves for electrodes using 950-CarbHS-G at a current density of  $0.1C$  ( $= 167.5 \text{ mA}\cdot\text{g}^{-1}$ ). (c) Coulombic efficiency for electrodes using 950-CarbHS-X (indicated by filled squares) and 950-CarbHS-G (indicated by hollow diamonds), respectively. Each specific capacity in (a) and (b) was calculated based on the mass of sulfur. The assumed full-cell properties are shown in Fig. 6-5b. [Ref. 252] Reproduced by permission of the PCCP Owner Societies.

The first plateau at around  $2.4 \text{ V vs. Li/Li}^+$  is attributed to the conversion of solid sulfur to soluble polysulfides. The next plateau at around  $2.1 \text{ V vs. Li/Li}^+$  suggests the conversion of polysulfides to solid  $\text{Li}_x\text{S}$ .<sup>15,71</sup> The main difference occurred after the 1st cycle. The 950-CarbHS-X showed a shuttle-effect which suggests the dissolution of polysulfide species into the electrolyte (Fig. 6-4a).<sup>71</sup> In contrast, the 950-CarbHS-G showed a coulombic efficiency (CE) of almost 100 % until the 20th cycle (Fig. 6-4b,c). To explain this significant difference in electrochemical behavior, various parameters can be considered. Firstly, former research has suggested that even a small amount of  $\text{SiO}_x$  (i.e. 2 wt%) can improve the cycle ability by avoiding the shuttle-effect.<sup>257</sup>

**Table 6-2** | Nitrogen adsorption data. <sup>a</sup>Values extracted from the Quenched Solid Density Functional Theory. [Ref. 252] Reproduced by permission of the PCCP Owner Societies.

Sample	BET surface area (m <sup>2</sup> g <sup>-1</sup> )	Total pore volume (cm <sup>3</sup> g <sup>-1</sup> ) <sup>a</sup>
550-CarbHS-X	534	1.60
<b>950-CarbHS-X</b>	<b>996</b>	<b>2.88</b>
550-CarbHS-G	529	0.58
<b>950-CarbHS-G</b>	<b>296</b>	<b>0.65</b>

In our case, both HS contain residual SiO<sub>2</sub> (Table 6-1), especially the 950-CarbHS-G nanospheres, which depict a silica loading almost twice higher than 950-CarbHS-X. Therefore, it can be concluded that residual SiO<sub>2</sub> is probably partially responsible for the difference in electrochemical properties between 950-CarbHS-X and 950-CarbHS-G samples. Secondly, the porous characteristics of the carbon shells (Table 6-2) were focused on. Although it has been suggested that both high surface areas and large pore volumes enhance the loading of sulfur into porous materials,<sup>71,251,257,258</sup> it remains delicate to consider an eventual influence on cycle performances.<sup>259,260</sup> Nevertheless, it can be assumed that, while enhancing the carbon/sulfur interface, an increase in the specific surface area of the conductive host concomitantly involves a significant rise in the sulfur/electrolyte interface, favoring henceforth the dissolution of intermediate polysulfides and the following shuttle-effect. At last, carbon hollow spheres with shells thicker than 50 nm have shown very stable charge-discharge properties.<sup>257</sup> From those reports and these results, it can be concluded that the 950-CarbHS-G displays better charge-discharge properties compared to 950-CarbHS-X also due to a thicker shell.

As 950-CarbHS-G nanospheres present the most promising results to prevent dissolution of polysulfides within the electrolyte, was focused on this material in the following study. Figure 6-4d shows cycling properties at 1C (= 1675 mA g<sup>-1</sup>) up to the 50th cycle of the 950-CarbHS-G/S composite made by a melt diffusion method, the mixture of 950-CarbHS-G



and S, and the mixture of HTC microspheres made from glucose without templates and S. These HTC non-hollow microspheres have been previously described by Yu et al.,<sup>261</sup> and were used here as Li-S cathodes after further thermal treatment at 950 °C under inert atmosphere, following the same pathway as described for HS. Contrary to the composite, the mixtures were made by mechanically mixing powdered sulfur and carbon compounds without further treatments. By using these three different carbon/sulfur materials, improvements in electrochemical properties related to the nanostructure of the carbon spheres were investigated. As shown in Figure 6-4d, the stable cycling properties by using nanostructured HS were obtained. This result clearly reveals that the highly porous shells of HS work as an adsorbent for soluble polysulfides. The higher specific capacity obtained *via* a melt diffusion method reveals the formation of a better conductive contact in the HS/S composite<sup>71,251,256,257</sup> compared to the mixture of HS and S. The results obtained for non-hollow microspheres underlined two benefits related to the use of HS in Li-S cells : (i) the nanosized spheres improve the specific capacity by ensuring formation of a conductive network in the cathode made by a composite consisting of carbon spheres, sulfur and binders. If it is compared that the specific capacity at the 1st cycle of the mixtures made by HS and non-hollow microspheres, the hollow spheres show a capacity of more than 800 mAh g<sup>-1</sup> while it remains at only 300 mAh g<sup>-1</sup> for non-hollow HTC microspheres; (ii) while the capacity decreases rapidly for the non-hollow microspheres, the HS/S composite, which displays a discharge capacity of 1000 mAh g<sup>-1</sup> at the 1st cycle, maintains a discharge capacity of 600 mAh g<sup>-1</sup> at the 50th cycle. The drop in specific capacity during the first few cycles can be explained by the formation of S layers on the surface of HS due to the strong affinity of sulfur for carbon.<sup>257,262</sup> This result reveals that the unique nanostructure of the hollow nanospheres is the essence of the high-performance electrochemical properties.

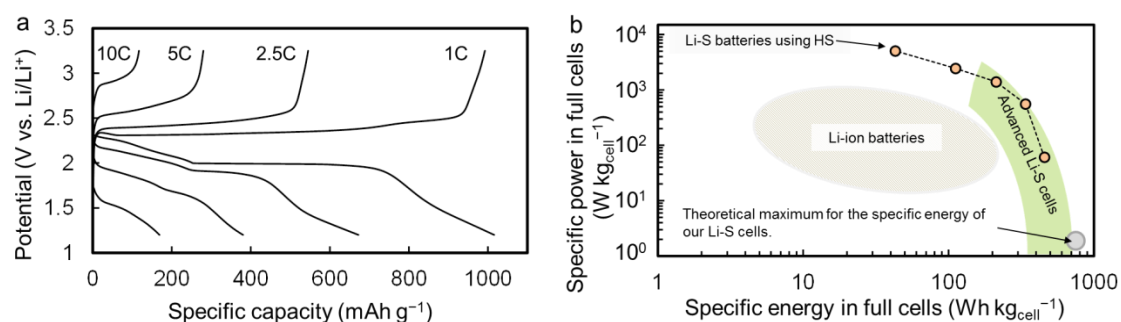


**Figure 6-5** | (a) Rate performance for 950-CarbHS-G/sulfur electrodes. The specific capacity was calculated based on the mass of sulfur. (b) Ragone plot for Li-S cells using the 950-CarbHS-G/sulfur composite electrode. We estimated that a full Li-S cell using 950-CarbHS-G contains 25 wt% of  $\text{Li}_2\text{S}$  for the total device weight. Details are available in the experimental procedures and Fig. S2. The theoretical maximum of the specific energy for our full cells was calculated as follows:  $2567 \text{ Wh kg}^{-1} \times 0.25 = 641 \text{ Wh kg}^{-1}$ . The properties of Li-ion batteries were taken from ref. 44. The references for the specific energy and the specific power of advanced the LSBs were taken from refs. 71 and 263. [Ref. 252] Reproduced by permission of the PCCP Owner Societies.

Finally, the rate capability of the HS/S composite cathode was investigated and was observed a remarkably high specific power of our Li-S systems. The HS/S composite cathode showed an initial discharge capacity of  $1000 \text{ mAh g}^{-1}$ ,  $700 \text{ mAh g}^{-1}$ , and  $400 \text{ mAh g}^{-1}$  at 1C ( $= 1675 \text{ mA g}^{-1}$ ), 2.5C ( $= 4187.5 \text{ mA g}^{-1}$ ), and 5C ( $= 8375 \text{ mA g}^{-1}$ ), respectively (Fig. 6-5a). Even at a very high current density of 10C ( $= 16750 \text{ mA g}^{-1}$ ), our cathode showed a discharge capacity of  $170 \text{ mAh g}^{-1}$ . The high rate capability of HS/S composite cathode is excellent if it is compared to other reports.<sup>71,263</sup> If it is assumed that a full Li-S cell using HS contains 25 wt% of  $\text{Li}_2\text{S}$ , this full cell will provide a specific energy of  $460 \text{ Wh kg}^{-1}$  and a specific power of  $5000 \text{ W kg}^{-1}$  (Fig. 6-5b). These exceptional results are based on the unique features of HS: (i) the highly porous nanostructured shells provide a stable cycle performance and a high rate capability by adsorbing polysulfides and improving the  $\text{Li}^+$  transportation, allowing the diffusion/filling of the electrolyte within the carbon-based framework; and (ii) the partially graphitized nanosized HS ensure a good conductive network within the cathode. These results suggest that the HS/S

composite cathode could be a promising electrode for Li-S systems, providing a specific energy for the full cell more than 2 times higher than the one typically describes for Li-ion batteries in full cells<sup>44</sup> (i.e., about 200 Wh kg<sub>cell</sub><sup>-1</sup>), and also, approaching the expected maximum specific energy for full Li-S battery cells of 700 Wh kg<sub>cell</sub><sup>-1</sup>.<sup>71</sup> Last but not least, a high specific power by using HS was successfully achieved, which is a major challenge for Li-S systems.

## 6. 4. SUMMARY FOR THE CHAPTER 6

Two different biomass-derived molecules were employed as a carbon source during the hydrothermal carbonization process, i.e. glucose and xylose. The resulting carbon hollow spheres from glucose exhibited thicker carbon walls as compared to the ones from xylose. Following further heat treatment at 950°C to improve the conductivity and infiltration with sulfur *via* a melt diffusion method, the two hollow carbon spheres-sulfur composites were tested as a cathode in Li-S batteries. The xylose-derived material showed a shuttle-effect which suggests the dissolution of polysulfide species into the electrolyte. In contrast, the glucose hollow spheres showed a coulombic efficiency (CE) of almost 100 % until the 20th cycle. These results are attributed to a higher amount of residual silica present in this material, known to improve the cycle performance where it becomes in good agreement with previous literature data. On the other hand, the smaller surface area and the thicker carbon shells in the case of glucose derived material might also play also an important role.

By comparing the performance of the hollow spheres with micrometer-sized full spheres obtained under exactly the same conditions from the hydrothermal carbonization of glucose without the use of silica templates, it was shown: (1) the highly porous shells of HS work as an absorbent for soluble polysulfides; (2) the infiltration of sulfur using the melt

diffusion method reveals the formation of a better conductive contact in the HS/S composite compared to the simple mixture of HS and S.

# CHAPTER 7. SUMMARY AND FUTURE PROSPECTS

In this thesis, diverse strategic designs of energy storage materials were explored. The main aims were: affordability and high-performances.

In the chapter 4, on eco-efficient synthesis of 1D intercalation compounds was described; a low-temperature aqueous solution synthesis of nanostructured 1D (molybdenum trioxide)  $\text{MoO}_3$  was developed. The subsequent self-assembly of the fibers to form large-scale freestanding films in paper-like structure was achieved without any assistance of organic compounds. Indeed, the whole processes, from synthesis to assembly, do not require toxic organic solvents. As an example of the application of our synthesized materials, 1D  $\text{MoO}_3$ , having the width in 50–100 nm, with the length in micro scale, and with thickness in  $\sim 10$  nm, and the macroscopic oxide papers consisting of 1D  $\text{MoO}_3$  and carbon materials were applied as the cathode and anode to lithium-ion batteries, respectively. As a cathode material, the 1D  $\text{MoO}_3$  showed a high rate capability with a stable cycle performance up to  $20 \text{ A g}^{-1}$  due to a short  $\text{Li}^+$  diffusion path along the [101] direction and less grain boundaries which were achieved by the precise nanostructure control. As an anode material, the composite paper showed the first specific discharge capacity of  $800 \text{ mAh g}^{-1}$ . These findings above indicate not only an affordable, eco-efficient synthesis and assembly of nanomaterials but also show a new attractive

strategy towards a possible whole aqueous process for a large-scale fabrication of freestanding oxide papers without any toxic organic solvent.

In the chapter 5, a new energy storage principle using polymeric frameworks was investigated. The new energy storage concept can deliver both high power and high energy. This is because of the novel energy storage nature of designed artificial polymeric frameworks which is different from classical energy storage mechanisms. The main novel discovery was as follows; since CTF-1 is linear stepwise *p*- and *n*-dopable polymer, therefore, this framework can storage energy as a cathode in the wide working potential with both cation below 3 V versus Li/Li<sup>+</sup> and anion above 3 V versus Li/Li<sup>+</sup> by the Faradaic reaction. Due to this feature, CTF-1 can storage high specific capacity of 540 mAh g<sup>-1</sup>. As the result the new energy storage concept which can deliver both high power and high energy was discovered by using a novel polymeric cathode. Unlike typical organic electrodes in sodium battery systems, the CTF-1 has a high specific power of 10 kW kg<sup>-1</sup>, specific energy of 500 Wh kg<sup>-1</sup>, and over 7,000 cycle life retaining 80 % of its initial capacity in half-cells. Indeed, all-organic energy storage devices based on CTF-1 suggested a possibility towards an extremely affordable energy storage device. Recent research on such artificial polymeric frameworks suggests their huge variability to utilize different functional structures which could even further increase power and energy even further when using different starting monomers. This would significantly extend the possibilities of electrical energy storage devices for a sustainable society based on our result. From this point of view, our research strategy which combined the experimental and theoretical study would be a model for further development of this field.

In the chapter 6, synthesizing new nanostructured carbons through the hydrothermal carbonization of biomass-derived precursors, according to an eco-efficient and cost-effective synthetic route, was focused on and these eco-efficient carbons were applied to lithium-sulfur

batteries. Porous carbon hollow spheres (HSs) exhibiting ~80 nm internal diameters and less than 10 nm thick nanostructured shells have been synthesized through a hydrothermal route. A fine control of the shell thickness and porosity allowed a simultaneous optimization in the achieved specific powers, specific energies and cycling properties of the carbon-sulfur composite electrodes. Our cell shows a remarkable high specific power of 5 kW kg<sup>-1</sup> in a full-cell.

These strategies based on building electrode materials considering from atomic scale would boost the further development of current energy storage devices, where electrochemical properties are actually hampering. New ideas and new sights based on deep understandings in fundamental science and in history of energy storage devices, in terms of technology's history, are expected to enable a bright future not only for our generation but also for our children. Up to now, we, human beings, are dependent on our “*Mother Nature*”: our past successes, such as the Industrial Revolution, are the great mankind's victories, however, still, they were given by the legacy from the Earth such as fossil fuels. Now, this is the time to shift from this old concept and to find a harmony, which could be called “*Aufheben*” as Hegel thought, between nature and us towards a sustainable system. This would be a fundamental common philosophy to bridge people who are standing at different positions, however, who are living in the 21<sup>st</sup> century together, to heritage current improved quality of life to our next-generations. Beyond the harmony, we will find the triumph.

*On ne fait rien de grand sans de grands hommes, et ceux-ci le sont pour  
l'avoir voulu.*

*Le Fil de l'épée* **1932**, Charles de Gaulle (1890 – 1970 A. D.)

# CHAPTER 8. SCIENTIFIC ACHIEVEMENTS RELATED TO THE PROJECTS

## PUBLICATIONS

9. “Hydrothermal carbohydrate-derived carbonaceous nano-architectures: on a synergistic effect towards improved performances as electrode materials for lithium-sulfur batteries”

N. Brun, **K. Sakaushi**(corresponding author), J. Eckert, M.-M. Titirici  
*ACS Sustainable Chem. Eng.*, DOI: 10.1021/sc4002966.

8. “Bipolar Porous Polymeric Frameworks for Low-cost, High-power, Long-life All-organic Energy Storage Devices”

**K. Sakaushi**(corresponding author), E. Hosono, G. Nickerl, H.S. Zhou, S. Kaskel, J. Eckert  
*J. Power Sources*, 245, 553 (2014).

7. “Aqueous Solution Process for the Synthesis and Assembly of nanostructured 1D  $\alpha$ -MoO<sub>3</sub> electrode materials”

**K. Sakaushi**(corresponding author), J. Thomas, S. Kaskel, J. Eckert  
*Chem. Mater.*, 25, 2557 (2013).

6. “Polymeric Frameworks towards Organic Semiconductors with Tunable Electronic Structures”

**K. Sakaushi**(corresponding author), H. Kandapal, L. Cano-Cortes, T. Gemming, G. Nickerl, J. Eckert, S. Kaskel, J. van den Brink  
*J. Phys. Chem. Lett.*, 4, 2977 (2013).



5. “Hydrothermal Nanocasting for the Synthesis of Hierarchically Porous Carbon-based Monoliths and Their Application in Lithium-Sulfur Batteries”

N. Brun, L. Yu, **K. Sakaushi**(corresponding author), J. Eckert, M.-M. Titirici  
*Carbon*, 61, 245 (2013).

4. “Hydrothermal carbon-based nanostructured hollow spheres for high-performance lithium-sulphur battery cathodes”

N. Brun, **K. Sakaushi**(corresponding author), L. Yu, L. Giebeler, J. Eckert, M.-M. Titirici  
*Phys. Chem. Chem. Phys.*, 15, 6080 (2013).

3. “Aromatic Porous-honeycomb Electrodes for a Sodium-organic Energy Storage Device”

**K. Sakaushi**(corresponding author), E. Hosono, G. Nickerl, T. Gemming, H.S. Zhou, S. Kaskel, J. Eckert  
*Nat. Commun.*, 4, 1485 (2013).

2. “Vergleich der Strategien und Aktivitäten in Deutschland und Japan auf dem Gebiet der Lithium-Ionen-Batterie Forschung „

**K. Sakaushi**(corresponding author), H. Ehrenberg, S. Kaskel, J. Eckert  
*5. Deutsch-japanisch-koreanisches Stipendiatenseminar. Veröffentlichungen des Japanisches-Deutschen Zentrums Berlin*, Band 63, 176-186 (2012).

1. “An Energy Storage Principle using Bipolar Porous Polymeric Frameworks”  
(Highlighted by Chemistry World, Royal Society of Chemistry)

**K. Sakaushi** (corresponding author), G. Nickerl, F. M. Wissler, D. Nishio-Hamane, E. Hosono, H.S. Zhou, S. Kaskel, J. Eckert  
*Angew. Chem. Int. Ed.*, 51, 7580-7584 (2012).

## PRESENTATIONS

5. “Porous Polymeric Frameworks as a cathode material: The Emergence of Electronic Properties and its Application in Energy Storage Devices”

**K. Sakaushi**, G. Nickerl, E. Hosono, H. Kandpal, L. Cano-Cortes, J. van den Brink, H.S. Zhou, S. Kaskel, J. Eckert  
The 9<sup>th</sup> SPSJ International Polymer Conference (Kobe, Japan)

13. Dec. 2012

4. “Porous Polymeric Framework Cathodes towards a Lithium-organic Energy Storage Device”

**K. Sakaushi**, G. Nickerl, E. Hosono, H. Kandpal, L. Cano-Cortes, J. van den Brink, H.S. Zhou, S. Kaskel, J. Eckert

2012 MRS Fall Meeting (Boston, USA)

28. Nov. 2012

3. “An Energy Storage Principle delivered by Bipolar Porous Polymeric Frameworks”

**K. Sakaushi**, G. Nickerl, F. M. Wisser, E. Hosono, H.S. Zhou, S. Kaskel, J. Eckert

4<sup>th</sup> PRiME (Hawaii, USA)

10. Oct. 2012

2. “Aqueous solution routes as an eco-efficient synthesis process for electrode materials of Li-ion batteries”

**K. Sakaushi**, J. Thomas, H. Ehrenberg, S. Kaskel, J. Eckert

62nd Annual Meeting of the International Society of Electrochemistry (Niigata, Japan)

11. Sept. 2011

1. “Eco-efficient synthesis of electrode materials via an aqueous solution process”

**K. Sakaushi**, Y. Oaki, H. Uchiyama, E. Hosono, H. Ehrenberg, S. Kaskel, H.S. Zhou, H. Imai, J. Eckert

LiBD-5 (Arcachon, France)

15. June 2011

## PATENTS

2. “Verwendung eines polymernetzwerkes als kathodenmaterial für wiederaufladbare batterien”

**K. Sakaushi** (50 %), G. Nickerl (30 %), S. Kaskel (10 %), J. Eckert (10%).

German patent: DE 10 2012 200 827.6 IFW-Akte 11117 DE.

1. “Verwendung eines polymernetzwerkes als kathodenmaterial für wiederaufladbare batterien”

**K. Sakaushi** (50 %), G. Nickerl (30 %), S. Kaskel (10 %), J. Eckert (10%). Filed in U. S. patent office.

## **A**WARDS AND INVITED TALKS

### **AWARD**

German Academic Exchange Office (DAAD) Research Grant (2010-2013: Grant No. A/09/74990)

### **INVITED TALKS**

6. “Polymeric Frameworks towards Energy Storage Materials”

**K. Sakaushi**

Max-Planck-Institute for Colloids and Interfaces, Colloid Chemistry Department Seminar (Invited by Dr. Tim Fellingner), (Potsdam, Germany)

14. Sept. 2012

5. “Energiespeicherstrategie in Japan: Eine wichtige Technologie für regenerative Energien”

**K. Sakaushi**

Tag der offenen Tür

Japanisch-Deutsches Zentrum Berlin, (Berlin, Germany)

9. June 2012

4. “Porous Organic Frameworks towards Energy Storage Materials”

**K. Sakaushi**

National Institute of Advanced Industrial Science and Technology (AIST), Energy Technology Research Institute, Energy Interface Technology Group, Group Seminar (Invited by Prof. Haoshen Zhou) (Tsukuba, Japan)

1. February 2012

3. “Synthesis, Morphological Control and Assembly of Nanomaterials via an Aqueous Solution Process and their Applications”

**K. Sakaushi**

Max-Planck-Institute for Colloids and Interfaces, Colloid Chemistry Department  
Seminar (Invited by Dr. Shiori Kubo), (Potsdam, Germany)

29. June 2011

2. „Societies in Changes“(Panel discussion)

**K. Sakaushi**

DAAD scholarship holders meeting (Dresden, Germany)

30. Nov. 2011

1. “Vergleich der Strategien und Aktivitäten in Deutschland und Japan auf dem  
Gebiet der Lithium-Ionen-Batterie Forschung”

**K. Sakaushi**

Fünfte Deutsch-Japanisch-Koreanische Stipendiatenseminar at  
Japanisch-Deutsches Zentrum Berlin, (Berlin, Germany)

23. Mai 2011

# ACKNOWLEDGEMENT

I am deeply indebted to German Academic Exchange Service (DAAD) for giving me an opportunity to build own research project in Germany. Prof. Jürgen Eckert (IFW Dresden, ICM) and Prof. Stefan Kaskel (TU Dresden, Dept. Inorg. Chem.) are acknowledged for the cooperation and great supports on the project at IFW Dresden and TU Dresden, respectively. Also, I would like to thank Prof. Tetsuichi Kudo (Univ. Tokyo / AIST), Prof. Haoshen Zhou, Dr. Eiji Hosono (AIST), Georg Nickerl, Florian M. Wisser (TU Dresden, Dept. Inorg. Chem.), Dr. Nicolas Brun, Linghui Yu, Dr. Maria-Magdalena Titirici (MPI Colloids and Interfaces), Dr. Peter Dunne, Dr. Simon Pauly, Dr. Jürgen Thomas, Dr. Thomas Gemming (IFW Dresden, ICM), Dr. Hemchandra Kandpal, Dr. Laura Cano-Cortes, and Prof. Jeroen van den Brink (IFW Dresden, ITF) and my brother Ryo for their kind supports and giving chance to work together. Ken Sakaushi acknowledges to Prof. Markus Antonietti (MPI Collides and Interfaces) for being the referee for my PhD thesis and also a committee for my defense, and to Prof. Alexander Eychmüller (TU Dresden, Dept. Phys. Chem.) for being a committee for my defense. I got a lot of supports from my friend Georg Nickerl (TU Dresden, Dept. Inorg. Chem.). Once again, Ken Sakaushi would like to thank him for his great contribution to my work.

The people in IFW Dresden and TU Dresden, especially, Brit, Heike, Andrea, Anne, Ronny, Grit and Gerlind, are also acknowledged for their wonderful supports to me. Here, I would like to thank for my friends who encouraged me; Jörn, Stefanos, Laura, Ganesh, Ioannis, Carmine, Pasquale, Judith, Nikolay, Steve, Peter, Daniel, Martin, Miléna, Fauly, Grzegorz, Thomas, Imad, Aslan, Gerog, Florian and Tim. Especially, Laura, your warm and kind heart

saved me at the difficult time. It was wonderful to meet DAAD scholars at Leipzig, especially, Milića, Lena, Heider, Aaron, Alba, Corentin and Latinos. The artist Shuhei Ise gave me pleasure moments in Germany. Terada-san and Chikako-san, also, the chats with you were so fun. Ken Sakaushi is deeply appreciated to J.T. for the understanding and supports. Indeed, Ken thanks Eriko for giving me precious moments by talking me every week even from Germany to Japan.

It is my great fortune in my life to have friends from my alma mater: Keio Gijuku. Every time, your warm friendship is keeping on supporting me. Finally, I would like to thank my Spanish family, Fernando, Anita and Anna, and my parents.

Ken Sakaushi

# REFERENCES

1. M. S. Whittingham, *Proceedings of the IEEE* **2012**, 0018-9219.
2. M. Armand & J.-M. Tarascon, *Nature* **2008**, *451*, 652.
3. J.-M. Tarascon, *Phil. Trans. R. Soc. A* **2010**, *368*, 3227.
4. New Energy and Industrial Technology Development Organization (NEDO), *Whitebook of NEDO renewable energy technology*, **2010** (Jpn.).
5. F. Schüth, *ChemSusChem* **2010**, *3*, 6.
6. R. Schlögel, *Angew. Chem. Int. Ed.* **2011**, *50*, 6424.
7. M. Kumhof & D. Muil, *IMF Working Paper* **2012**, WP/12/256.
8. J. Murray & D. King, *Nature* **2012**, *481*, 433.
9. T. R. Cook *et al.*, *Chem. Rev.* **2010**, *110*, 6474.
10. Z. Yang *et al.*, *Chem. Rev.* **2011**, *111*, 3577.
11. Office of Electricity Delivery and Energy, *The Smart Grid: An Introduction*, the U. S. Department of Energy **2008**.
12. B. Dunne, H. Kamath & J.-M. Tarascon, *Science* **2011**, *334*, 928.
13. J.-M. Tarascon & M. Armand, *Nature* **2001**, *414*, 359.
14. [http://www.mitsubishi-motors.co.jp/i-miev/spec/spe\\_02.html](http://www.mitsubishi-motors.co.jp/i-miev/spec/spe_02.html) (Jpn.)
15. P. G. Bruce, S. A. Freundberger, L. J. Hardwick & J.-M. Tarascon, *Nat. Mater.* **2012**, *11*, 19.
16. K. Sakaushi, H. Ehrenberg, S. Kaskel & J. Eckert, 5. *Deutsch-japanisch-koreanisches Stipendiatenseminar. Veröffentlichungen des Japanisches-Deutschen Zentrums Berlin* **2012**, Band 63, 176.
17. <http://www.chevrolet.com/volt-electric-car/features-specs/options.html> (on 15.04.2013 visited)
18. <http://www.toyota.com/prius/#!/Welcome> (on 15.04.2013 visited)
19. *Lithium Batteries: Science and Technology* (ed. G.-A. Nazri & G. Pistoia), Springer, U.S.A. **2003**.
20. <http://physics.ucsd.edu/do-the-math/2011/08/nation-sized-battery/>
21. W. F. Pickard, *Energy Policy* **2012**, *45*, 263.
22. G. B. Haxel, J. B. Hedrick & G. J. Orris, *Rareearthelements—Critical resources for hightechnology*. U.S. Geological Survey Fact Sheet 087–02 **2005**:  
<http://pubs.usgs.gov/fs/2002/fs087-02/>

23. *Fast Ion Transport in Solids: Solid State Batteries and Devices* (ed. W. van Gool), Elsevier Science Publishing, U.S.A. **1973**.
24. M. S. Whittingham, *Chalcogenide battery*. US Patent 4009052 **1976**.
25. M. S. Whittingham, *Science* **1976**, 192, 1226.
26. K. Mizushima, P. C. Jones, P. J. Wiseman & J. B. Goodenough, *Mat. Res. Bull.* **1980**, 15, 783.
27. D. W. Murphy, F. J. DiSalvo, J. N. Carides & J. V. Waszczak, *Mat. Res. Bull.* **1978**, 13, 1395.
28. M. Lazzari & B. A. Scrosati, *J. Electrochem. Soc.* **1980**, 127, 773.
29. S. Nishimura *et al.*, *Nat. Mater.* **2008**, 7, 707.
30. A. K. Padhi, K. S. Nanjundaswamy & J. B. Goodenough, *J. Electrochem. Soc.* **1997**, 114, 1188.
31. S. Nishimura, M. Nakamura, R. Natsui & A. Yamada, *J. Am. Chem. Soc.* **2010**, 132, 13596.
32. A. Yamada *et al.*, *Nat. Mater.* **2006**, 5, 357.
33. L. Laffont *et al.*, *Chem. Mater.* **2006**, 18, 5520.
34. N. Meethong, H.-Y. S. Huang, S. A. Speakman, W. C. Carter & Y.-M. Chiang, *Adv. Funct. Mater.* **2007**, 17, 1115.
35. C. Delmas *et al.*, *Nat. Mater.* **2008**, 7, 665.
36. T. Ohzuku & Y. Makimura, *Chem. Lett.* **2001**, 30,744.
37. Z.H. Lu, Z.H. Chen & J. R. Dahn, *Chem. Mater.* **2003**, 15, 3214.
38. T. Ohzuku & Y. Makimura, *Chem. Lett.* **2001**, 30,642.
39. Z. Lu, D. D. MacNeil & J. R. Dahn, *Electrochem. Solid State Lett.* **2001**, 4, A191.
40. A. D. Robertson & P. G. Bruce, *Chem. Commun.* **2002**, 23, 2790.
41. C. S. Johnson *et al.*, *Electrochem. Commun.* **2004**, 6, 1085.
42. A. R. Armstrong *et al.*, *J. Am. Chem. Soc.* **2006**, 128, 8694.
43. M. S. Whittingham, *Prog. Solid State Chem.* **1978**, 12, 41.
44. C. Delmas, J.-J. Braconnier, C. Fouassier & P. Hagenmuller, *Solid State Ion.* **1981**, 3–4, 165.
45. N. Yabuuchi, *et al.*, *Nature Mater.* **2012**, 11, 512.
46. M. M. Thackeray, W. I. F. David, P. G. Bruce & J. B. Goodenough, *Mat. Res. Bull.* **1983**, 18, 461.
47. T. Ohzuku, A. Ueda & N. Yamamoto, *J. Electrochem. Soc.* **1995**, 142, 1431.
48. Q. Zhong, A. Banakdarpour, M. Zhong, Y. Gao & J. R. Dahn, *J. Electrochem. Soc.* **1997**, 144, 205.
49. A. Nyten, A. Abouimrane, M. Armand, T. Gustafsson & J. O. Thomas, *Electrochem. Commun.* **2005**, 7, 156.
50. A. Nyten, S. Kamali, L. Haeggstoem, T. Gustafsson & J. O. Thomas, *J. Mater. Chem.* **2006**, 16, 2266.
51. S. Nishimura *et al.*, *J. Am. Chem. Soc.* **2008**, 130, 13212.
52. A. K. Pahdi, K. S. Nanjundaswamy, C. Masquelir, S. Okada & J. B. Goodenough, *J. Electrochem. Soc.* **1997**, 144, 1609.
53. B. L. Ellis, W. R. M. Makahnouk, Y. Makimura, K. Tohgill & L. F. Nazar, *Nat. Mater.* **2007**, 6, 749.



54. N. Recham *et al.*, *Nat. Mater.* **2009**, 9, 68.
55. P. Poizot, S. Laruelle, S. Grugeon, L. Dupont & J.-M. Tarascon, *Nature* **2000**, 407, 496.
56. G. G. Amatucci & N. Pereira, *J. Fluor. Chem.* **2007**, 128, 243.
57. W. Feng *et al.*, *J. Am. Chem. Soc.* **2011**, 133, 18828.
58. H. Akamatsu, H. Inokuchi & Y. Matsunaga, *Nature* **1954**, 173, 168.
59. H. Shirakawa, E. J. Louis, A. G. MacDiarmid, C. K. Chiang, A. J. Heeger, *J. Chem. Soc., Chem. Commun.* **1977**, 578.
60. C. K. Chiang *et al.*, *Phy. Rev. Lett.* **1977**, 39, 1098.
61. P. Novák, K. Müller, K. S. V. Santhanam & O. Haas, *Chem. Rev.* **1997**, 97, 207.
62. Y. Liang, Z. Tao & J. Chen, *Adv. Energy Mater.* **2012**, 2, 742.
63. K. M. Abraham & Z. Jiang, *J. Electrochem. Soc.* **1996**, 143, 1.
64. T. Ogasawara, A. Débart, M. Holzapfel, P. Novák & P. G. Bruce, *P. J. Am. Chem. Soc.* **2006**, 128, 1390.
65. S. A. Freundberger *et al.*, *J. Am. Chem. Soc.* **2011**, 133, 8040.
66. M. Leskes *et al.*, *Angew. Chem. Int. Ed.* **2012**, 51, 8560.
67. Y. C. Lu *et al.*, *J. Am. Chem. Soc.* **2010**, 132, 12170.
68. Z. Q. Peng, S. A. Freundberger, Y. H. Chen & P. G. Bruce, *Science* **2012**, 337, 563.
69. D. Herbert & J. Ulam, *U.S. Pat.* **1962**, 3 043 896.
70. M. L. B. Rao, *U.S. Pat.* **1968**, 3 413 154.
71. X. Ji & L. F. Nazar, *J. Mater. Chem.* **2010**, 20, 9821.
72. T. Kudo, H. Obayashi & T. Gejo, *J. Electrochem. Soc.* **1975**, 122, 159.
73. M. Hibino, T. Kimura, Y. Suga, T. Kudo & N. Mizuno, *Scientific Reports* **2012**, 2, 601.
74. B. D. Cullity, *Elements of X-ray diffraction 2<sup>nd</sup> edition*, Addison-Wesley Publishing, U.S.A. **1977**.
75. *Facts of X-ray diffraction analysis (ed. I. Nakai & F. Izumi)*, Asakura shoten, Japan **2009** (Jpn.).
76. *Transmission Electron Microscope (ed. The surface science society of Japan)*, Maruzen, Japan **2005** (Jpn.).
77. T. Takeuchi, *Chemistry of adsorption*, Sangyo tosho, Japan **1995** (Jpn.).
78. S. Kondo, T. Ishikawa & I. Abe, *Science on adsorption*, Maruzen, Japan **2001** (Jpn.).
79. *Handbook of porous solids (ed. F. Schüth, K. S. W. Sing & J. Weitkamp)*, Wiley-VCH Verlag, Germany **2002**.
80. P. W. Atkins, *Physical Chemistry Sixth edition*, Oxford University Press, U.K. **1998**.
81. *Manual for Fundamental Electrochemical measurements (ed. The Electrochemical Society of Japan)*, Maruzen, Japan **2004** (Jpn.).
82. *Manual for Applied Electrochemical measurements (ed. The Electrochemical Society of Japan)*, Maruzen, Japan **2009** (Jpn.).
83. *Lithium secondary batteries (ed. Z. Ogumi)*. Ohm Publishing, Japan **2009** (Jpn.).

84. T. Kudo, M. Hibino & I. Honma, *Science of Lithium-ion Batteries*, Uchida Rokakuho Publishing, Japan **2010** (*Jpn.*).
85. B. Kang & G. Ceder, *Nature* **2009**, 458, 190.
86. H. Zhang, X. Yu & P. V. Braun, *Nat. Nanotechnol.* **2011**, 6, 277.
87. Y. Wang, H. Li, P. He, E. Hosono & H. Zhou, *Nanoscale* **2010**, 2, 1294.
88. A. M. Moraes & C. M. Lieber, *Science* **1998**, 279, 208.
89. M.H. Huang *et al.*, *Science* **2001**, 292, 1897.
90. A. R. Armstrong, G. Armstrong, J. Canales, P. G. Bruce, *Angew. Chem. Int. Ed.* **2004**, 43, 2286.
91. E. Hosono, T. Kudo, I. Honma, H. Matsuda & H. Zhou, *Nano letters* **2009**, 9, 1045.
92. K. Ariga *et al.*, *Sci. Technol. Adv. Mater.* **2008**, 9, 014109.
93. J.W. Liu, S.Y. Zhang, H. Qi, W.C. Wen & S.H. Yu, *Small* **2012**, 8, 2412.
94. J.W. Liu, H.W. Liang & S.H. Yu, *Chem. Rev.* **2012**, 112, 4770.
95. A. Tao *et al.*, *Nano Lett.* **2003**, 3, 1229.
96. A. Tao & P.D. Yang, *J. Phys. Chem. B* **2005**, 109, 15687.
97. I. Patla *et al.*, *Nano Lett.* **2007**, 7, 1459.
98. H.Y. Shi *et al.*, *Adv. Funct. Mater.* **2010**, 20, 958.
99. M. Niederberger, F. Krumeich, H. J. Muhr, M. Müller & R. Nesper, *J. Mater. Chem.* **2001**, 11, 1941.
100. G. R. Patzke, F. Krumeich & R. Nesper, *Angew. Chem. Int. Ed.* **2002**, 41, 2446.
101. G. R. Patzke *et al.*, *Chem. Mater.* **2004**, 16, 1126.
102. K. J. Reynolds, J. A. Barker, N. C. Greenham, R. H. Friend & G. L. Frey, *J. Appl. Phys.* **2002**, 92, 7556.
103. F. M. Liu, S.Y. Shao, X.Y. Guo, Y. Zhao, Z. Y. Xie, *Sol. Eng. Sol. Mat.* **2010**, 94, 842845.
104. N. A. Chernova, M. Roppolo, A. C. Dillon & M. S. Whittingham, *J. Mater. Chem.* **2009**, 19, 2526.
105. L. Campanel & G. Pistoia, *J. Electrochem. Soc.* **1971**, 118, 1905.
106. S.H. Lee *et al.*, *Adv. Mater.* **2008**, 20, 3627.
107. C. Julien, A. Khelifa, J. P. Guesdon & A. Gorenstein, *Appl. Phys. A* **1994**, 59, 173.
108. M. Winter, J. O. Besenhard, M. E. Spahr & P. Novák, *Adv. Mater.* **1998**, 10, 725.
109. A. S. Arico, P. G. Bruce, B. Scrosati, J.-M. Tarascon & W. van Schalkwijk, *Nat. Mater.* **2005**, 4, 366.
110. P. G. Bruce, B. Scrosati & J.-M. Tarascon, *Angew. Chem. Int. Ed.* **2008**, 47, 2930.
111. M. Kakihana & M. Yoshimura, *Bull. Chem. Soc. Jpn.* **1999**, 72, 1427.
112. H. Imai, Y. Oaki & A. Kotachi, *Bull. Chem. Soc. Jpn.* **2006**, 79, 1834.
113. Y. Masuda, *J. Ceram. Soc. Jpn.* **2007**, 115, 101.
114. H. Hosono, *J. Ceram. Soc. Jpn.* **2012**, 120, 47.
115. Y. Oaki & H. Imai, *Adv. Mater.* **2006**, 18, 1807.
116. H. Uchiyama, H. Ohgi & H. Imai, *Cryst. Growth Des.* **2006**, 6, 2186.

117. Y. Oaki & H. Imai *Angew. Chem. Int. Ed.* **2007**, *46*, 4951.
118. K. Sakaushi *et al.*, *Nanoscale* **2010**, *2*, 2424.
119. K. Sakaushi *et al.*, *Small* **2010**, *6*, 776.
120. H. Uchiyama & H. Imai, *Cryst. Growth Des.* **2010**, *10*, 1777.
121. Y. Oaki, T. Anzai & H. Imai, *Adv. Funct. Mater.* **2010**, *20*, 4127.
122. M. Oba, Y. Oaki & H. Imai, *Adv. Funct. Mater.* **2010**, *20*, 4279.
123. Y. Oaki, N. Yagita & H. Imai, *Chem.–Eur. J.* **2012**, *18*, 110.
124. Y. Iriyama, T. Abe, M. Inaba & Z. Ogumi, *Solid State Ion.* **2000**, *135*, 95.
125. L. Wang, F. Zhou, Y.S. Meng & G. Ceder, *Phys. Rev. B* **2006**, *76*, 165435.
126. C. A. Fisher & S. Islam, *J. Mater. Chem.* **2008**, *18*, 1209.
127. P. J. Yunker, T. Still, M. A. Lohr & A. G. Yodh, *Nature* **2011**, *476*, 308.
128. N. D. Denkov *et al.*, *Nature* **1993**, *361*, 26.
129. R. D. Deegan *et al.*, *Nature* **1997**, *389*, 827.
130. H. Hu & R. G. Larson, *J. Phys. Chem. B* **2002**, *106*, 1334.
131. H. Uchiyama, D. Shimaoka & H. Kozuka, *Soft Matter* **2012**, *8*, 11318.
132. J. Park & J. Moon, *Langmuir* **2006**, *22*, 3506
133. K. Evanoff *et al.*, *ACS Nano* **2012**, *6*, 9837.
134. K. Sakaushi *et al.*, *Angew. Chem. Int. Ed.* **2012**, *51*, 7850.
135. K. Sakaushi *et al.*, *Nat. Commun.* **2013**, *4*, 1485.
136. J. v. Liebig, *Ann. Pharm.* **1834**, *10*, 10.
137. R. Riedel *et al.*, *Chem. Mater.* **1998**, *10*, 2964.
138. F. Goettmann, A. Fischer, M. Antonietti & A. Thomas, *Angew. Chem. Int. Ed.* **2006**, *45*, 4467.
139. X.C. Wang *et al.*, *Nat. Mater.* **2008**, *8*, 76.
140. M. J. Bojdys, J.-O. Müller, M. Antonietti & A. Thomas, *Chem.–Eur. J.* **2008**, *14*, 8177.
141. P. Kuhn, M. Antonietti & A. Thomas, *Angew. Chem. Int. Ed.* **2008**, *47*, 3450.
142. K. S. Kang, Y. S. Meng, J. Breger, C. P. Grey & G. Ceder, *Science* **2006**, *311*, 977.
143. Y. G. Wang, Y. R. Wang, E. Hosono, K. X. Wang & H. S. Zhou, *Angew. Chem. Int. Ed.* **2008**, *47*, 7461.
144. B. Kang & G. Ceder, *Nature* **2009**, *458*, 190.
145. S. W. Lee *et al.*, *Nature Nanotechnol.* **2010**, *5*, 531.
146. H. Zhang, X. Yu & P. V. Braun, *Nature Nanotechnol.* **2011**, *6*, 277.
147. T. Ogasawara, A. Débart, M. Holzapfel, P. Novák & P. G. Bruce, *J. Am. Chem. Soc.* **2006**, *128*, 1390.
148. A. P. Côté *et al.*, *Science* **2005**, *310*, 1166.
149. A. I. Cooper, *Adv. Mater.* **2009**, *21*, 1291.
150. J. X. Jiang & A. I. Cooper, *Top Curr. Chem.* **2010**, *293*, 1.

151. A. Thomas, *Angew. Chem., Int. Ed.* **2010**, *49*, 8328–8344.
152. A. Thomas, P. Kuhn, J. Weber, M. M. Titirici & M. Antonietti, *Macromol. Rapid Commun.* **2009**, *30*, 221.
153. X. C. Wang *et al.*, *Nature Mater.* **2009**, *8*, 76.
154. R. Palkovits, M. Antonietti, P. Kuhn, A. Thomas & F. Schüth, *Angew. Chem. Int. Ed.* **2009**, *48*, 6909.
155. Y. Kou, Y. Xu, Z. Guo & D. Jiang, *Angew. Chem. Int. Ed.* **2011**, *50*, 8753.
156. M. Rose *et al.*, *J. Mater. Chem.* **2011**, *21*, 711.
157. M. V. Shishkina, M. M. Teplyakov, V. P. Chebotaryev & V. V. Korshak, *Makromol. Chem.* **1974**, *175*, 3475.
158. S. Sandroni & S. Geiss, *Z. Anal. Chem.* **1966**, *220*, 321.
159. K. Sato, M. Noguchi, A. Demachi, N. Oki & M. Endo, *Science* **1994**, *264*, 556.
160. J. R. Dahn, T. Zheng, Y. Liu & J. S. Xue, *Science* **1995**, *270*, 590.
161. T. Zheng, W. R. McKinnon & J. R. Dahn, *J. Electrochem. Soc.* **1996**, *143*, 2137.
162. P. Kuhn, A. Thomas & M. Antonietti, *Macromolecules* **2009**, *42*, 319.
163. M. Winter, J. O. Besenhard, M. E. Spahr & P. Novák, *Adv. Mater.* **1998**, *10*, 725.
164. H. S. Zhou, S. Zhu, M. Hibino, I. Honma & M. Ichihara, *Adv. Mater.* **2003**, *15*, 2107.
165. K. Oyaizu, T. Sukegawa & H. Nishide, *Chem. Lett.* **2011**, *40*, 184.
166. P. J. Nigrey, D. MacInnes, D. P. Nairns, A. G. MacDiarmid & A. J. Heeger, *J. Electrochem. Soc.* **1981**, *128*, 1651.
167. P. G. Bruce & M. Y. Saidi, *J. Electroanal. Chem.* **1992**, *332*, 93.
168. Y. Mizuno *et al.*, *Electrochim. Acta* **2012**, *63*, 139.
169. C. M. Burba & R. Frech, *J. Phys. Chem. B* **2005**, *109*, 15161.
170. R. Aroca, M. Nazri, G. A. Nazri, G. A. J. Camargo & M. Trisc, *J. Solution Chem.* **2000**, *29*, 1047
171. J. Barek, A. G. Fogg, J. C. Moreira, M. V. B. Zanoni & J. Zima, *Anal. Chim. Acta* **1996**, *320*, 31.
172. R. E. Del Sesto *et al.*, *J. Org. Chem.* **2003**, *68*, 3367.
173. H. Nishide & T. Suga, *Electrochem. Soc. Interface* **2005**, *15*, 32.
174. H. Chen *et al.*, *ChemSusChem* **2008**, *1*, 348.
175. T. Suga, H. Ohshiro, S. Sugita, K. Oyaizu & H. Nishide, *Adv. Mater.* **2011**, *23*, 1627.
176. T. Oshima, M. Kajita, & A. Okuno, *Int. J. Appl. Ceram. Technol.* **2004**, *1*, 269.
177. S.W. Kim, D.H. Seo, X. Ma, G. Ceder & K. Kang, *Adv. Energy. Mater.* **2012**, *2*, 710.
178. B. L. Ellis & L. F. Nazar, *Curr. Opin. Solid State Mater. Sci.* **2012**, *16*, 168.
179. M. D. Slater, D. Kim, E. Lee & C. S. Johnson, *Adv. Funct. Mater.* **2013**, *23*, 947.
180. G. H. Newman & L. P. Klemann, *J. Electrochem. Soc.* **1980**, *127*, 2097.
181. C. Delmas, J.-J. Braconnier, C. Fouassier & P. Hagenmuller, *Solid State Ion.* **1981**, *3–4*, 165.
182. Z. Lu & J. R. Dahn, *J. Electrochem. Soc.* **2001**, *148*, A1225.

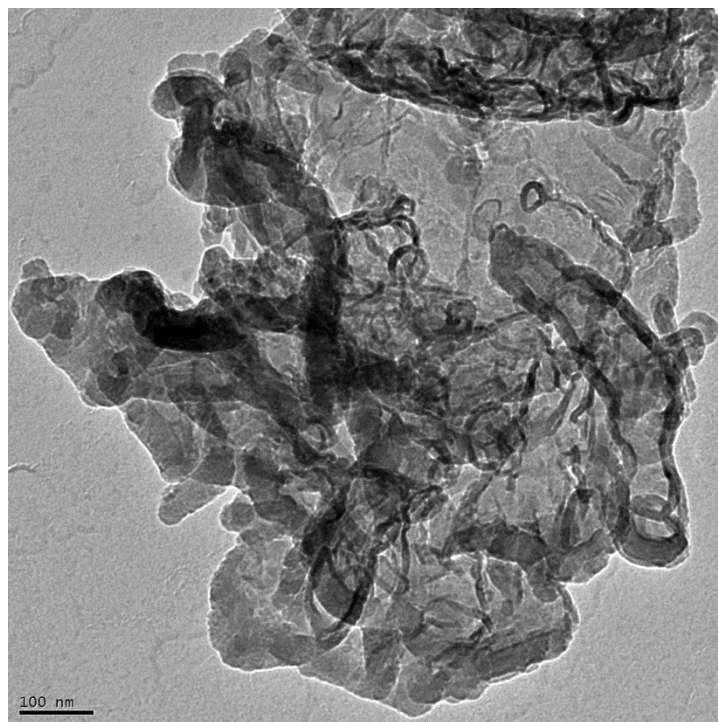
183. B. L. Ellis, W. R. M. Makahnouk, Y. Makimura, K. Toghill & L. F. Nazar, L. F. *Nat. Mater.* **2007**, *6*, 749.
184. N. Recham *et al.* *J. Electrochem. Soc.* **2009**, *156*, A993.
185. L. S. Plashnista, E. Kobayashi, Y. Noguchi, S. Okada & J. Yamaki, *J. Electrochem. Soc.* **2010**, *157*, A536.
186. K. T. Lee, T. N. Ramesh, F. Nan, G. Botton & L. F. Nazar, *Chem. Mater.* **2011**, *23*, 3593.
187. S. Komaba *et al.*, *Adv. Funct. Mater.* **2011**, *21*, 3859.
188. Z. Chen *et al.*, *ACS Nano* **2012**, *6*, 4319.
189. N. Yabuuchi *et al.*, *Nature Mater.* **2012**, *11*, 512.
190. E. Hosono *et al.*, *J. Power Sources* **2012**, *217*, 43.
191. H. Nishide & K. Oyaizu, *Science* **2008**, *319*, 737.
192. D. MacInnes *et al.*, *J. Chem. Soc., Chem. Comm.* **1981**, 317.
193. L. W. Schacklette, J. E. Toth, N. S. Murthy & R. H. Baugham, *J. Electrochem. Soc.* **1985**, *32*, 1529.
194. C. Hérold, D. Billaud & R. Yazami, *Solid State Ion.* **1990**, *40-41*, 985.
195. T. Suga, S. Sugita H. Ohshiro, K. Oyaizu & H. Nishide, *Adv. Mater.* **2011**, *13*, 751.
196. L. Zhao *et al.*, *Adv. Energy Mater.* **2012**, *2*, 962.
197. F. Tuinstra & J. L. Koenig, *J. Chem. Phys.* **1970**, *53*, 1126.
198. P. Lespade, R. Al-Jishi & M. S. Dresselhaus, *Carbon* **1982**, *20*, 427.
199. A. C. Ferrari *et al.*, *Phys. Rev. Lett.* **2006**, *97*, 187401.
200. N. Hellgren, M. P. Johansson, E. Broitman, L. Hultman & J.-E. Sundgren, *Phys. Rev. B* **1999**, *59*, 5162.
201. A. C. Ferrari & J. Robertson, *Phil. Trans. R. Soc. Lond. A* **2004**, *362*, 2477.
202. T. Zheng, W. Xing, & J. R. Dahn, *Carbon* **1996**, *34*, 1501.
203. A. Thomas *et al.*, *J. Mater. Chem.* **2008**, *18*, 4893.
204. K. S. Novoselov *et al.*, *Proc. Natl. Acad. Sci. USA* **2005**, *102*, 10451.
205. A. K. Geim & K. S. Novoselov, *Nature Mater.* **2007**, *6*, 183.
206. M. Bieri *et al.*, *Chem. Commun.* **2009**, 6919.
207. J. Weber, M. J. Bojdys & A. Thomas, Polymeric Frameworks: Toward Porous Semiconductors, in *Supramolecular Soft Matter: Applications in Materials and Organic Electronics (ed T. Nakanishi)*, John Wiley & Sons Inc., U.S.A. **2011**.
208. Y. Wang, X.C. Wang & M. Antonietti, *Angew. Chem. Int. Ed.* **2012**, *51*, 68.
209. M. Okubo *et al.*, *ACS Nano* **2010**, *4*, 741.
210. C. Ho, I. D. Raistrick & R. A. Huggins, *J. Electrochem. Soc.* **1980**, *127*, 343.
211. A. G. Miller & J. W. Macklin, *J. Phys. Chem.* **1985**, *89*, 1193.
212. S. Schantz, L. M. Torell & J. R. Stevens, *J. Appl. Phys.* **1988**, *64*, 2038.
213. S. C. Nunes *et al.*, *Electrochim. Acta* **2007**, *53*, 1466.

214. R. K. Sinha, E. Nicol, V. Steinmetz & P. Maître, *J. Am. Soc. Mass. Spectrom.* **2010**, *21*, 758.
215. T. Kudo & M. Hibino, *Solid State Ion.* **1996**, *84*, 65.
216. M. Okubo *et al.*, *J. Am. Chem. Soc.* **2007**, *29*, 7444.
217. M. Okubo, J. Kim, T. Kudo, H.S. Zhou & I. Honma, *J. Phys. Chem. C* **2009**, *113*, 15337.
218. C. Ponce de León, A. Frías-Ferrer, J. González-García, D. A. Szánto & F. C. Walsh, *J. Power Sources* **2006**, *116*, 716.
219. V. L. Chevrier & G. Ceder, *J. Electrochem. Soc.* **2011**, *158*, A1011.
220. P. Senguttuvan, G. Rousse, V. Seznec, J.-M. Tarascon & M. R. Palacín, *Chem. Mater.* **2011**, *23*, 4109.
221. A. Fukunaga *et al.*, *J. Power Sources* **2012**, *203*, 52.
222. A. Ponrouch, E. Marchante, M. Coutry, J.-M. Tarascon & M. R. Palacín, *Energy Env. Sci.* **2012**, *5*, 8572.
223. L. M. Zhu, A. W. Lei, Y. L. Cao, X. P. Ai & H. X. Yang, *Chem. Commun.* **2013**, *49*, 567.
224. M. Mastragostino, C. Arbizzani, R. Paraventi & A. Zanelli, *J. Electrochem. Soc.* **2000**, *147*, 407.
225. W. Choi, D. Harada, K. Oyaizu & H. Nishide, *J. Am. Chem. Soc.* **2011**, *133*, 19838.
226. H. Akamatsu, H. Inokuchi & Y. Matsunaga, *Nature* **1954**, *173*, 168.
227. S. R. Forrest & M. E. Thomson, *Chem. Rev.* **2007**, *107*, 923.
228. K. Walzer, B. Maennig, M. Pfeiffer & K. Leo, *Chem. Rev.* **2007**, *107*, 1233.
229. C.W. Tang & S. A. VanSlyke, *Appl. Phys. Lett.* **1987**, *51*, 913.
230. J. H. Burroughes *et al.*, *Nature* **1990**, *347*, 539.
231. J. Kido, M. Kimura & K. Nagai, *Science* **1995**, *267*, 1332–1334.
232. R. H. Friend *et al.*, *Nature* **1999**, *397*, 121.
233. C.W. Tang, *Appl. Phys. Lett.* **1986**, *48*, 183.
234. C. J. Brabec, N. S. Sariciftci & J. C. Hummelen, *Adv. Funct. Mater.* **2001**, *11*, 15.
235. K. Hayashi, S. Matsuishi, T. Kamiya, M. Hirano & H. Hosono, *Nature* **2002**, *419*, 462.
236. H. Yanagi, K. Ueda, H. Ohta, M. Orita, M. Hirano & H. Hosono, *Solid State Commun.* **2001**, *121*, 15.
237. J. Zaumseil & H. Sirringhaus, *Chem. Rev.* **2007**, *107*, 1296.
238. X. Feng *et al.*, *Adv. Mater.* **2012**, *24*, 3026.
239. A. Du, S. Sanvito & S. C. Smith, *Phys. Rev. Lett.* **2012**, *108*, 197207.
240. P.D. Yang & J.-M. Tarascon, *Nature Mater.* **2012**, *11*, 560.
241. K. Schwinghammer *et al.*, *Angew. Chem. Int. Ed.* **2013**, *52*, 2435.
242. S. Ren *et al.*, *Adv. Mater.* **2012**, *24*, 2357.
243. W. Weppner & R. A. Huggins, *J. Electrochem. Soc.* **1977**, *124*, 1569.
244. A. K. Paldi, K. S. Nanjundaswamy, C. Masquelier, S. Okada & J. B. Goodenough, *J. Electrochem. Soc.* **1997**, *144*, 1609.

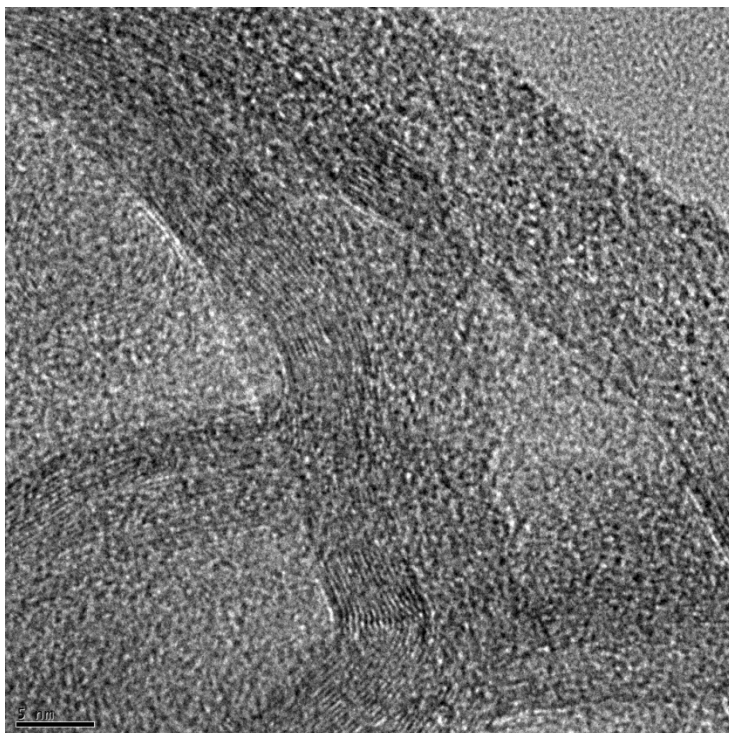
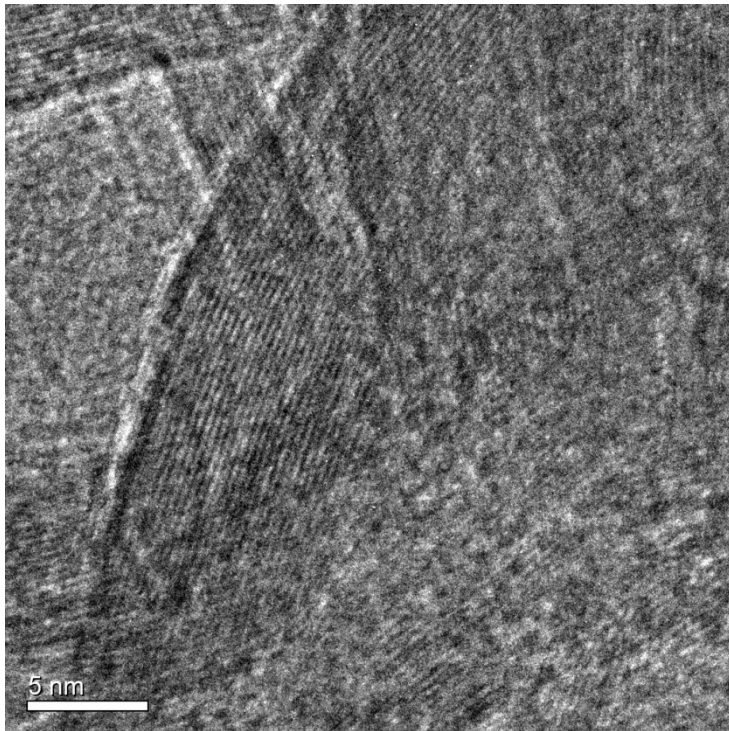
245. J. B. Goodenough & Y. Kim, *Chem. Mater.* **2010**, *22*, 587.
246. M. L. Dzurus & G. R. Henning, *J. Chem. Phys.* **1957**, *27*, 275.
247. S. Wang, Y. Matsumura & T. Maeda, *Synth. Met.* **1995**, *71*, 1759.
248. G. Profeta, M. Calandra & F. Mauri, *Nat. Phys.* **2012**, *8*, 131.
249. T. Morikazu, R. Kubo & N. Saito, *Statistical Physics I: Equilibrium Statistical Mechanics.* **1992**, Springer USA.
250. D. Nole & V. Moss, *U.S. Pat.* **1970**, 3 532 534.
251. X. Ji, K. T. Lee & L. F. Nazar, *Nat. Mater.* **2009**, *8*, 500.
252. N. Brun *et al.*, *Phys. Chem. Chem. Phys.* **2013**, *15*, 6080.
253. J. H. Shin & E. J. Cairns, *J. Power Sources* **2008**, *177*, 537.
254. X. Ji, S. Evers, R. Black & L. F. Nazar, *Nat. Commun.* **2011**, *2*, 325.
255. D. Aurbach *et al.*, *J. Electrochem. Soc.* **2009**, *8*, A694.
256. N. Jayaprakash, J. Shen, S. S. Moganty, A. Corona & L. A. Archer, *Angew. Chem. Int. Ed.* **2011**, *50*, 5904.
257. J. Schusterv *et al.*, *Angew. Chem. Int. Ed.* **2012**, *51*, 3591.
258. C. Liang, N. J. Dudney & J. Y. Howe, *Chem. Mater.* **2009**, *21*, 4724.
259. X. Li *et al.*, *J. Mater. Chem.* **2011**, *21*, 16603.
260. R. Demir-Cakan *et al.*, *J. Am. Chem. Soc.* **2011**, *133*, 16154.
261. L. Yu *et al.*, *Langmuir* **2012**, *28*, 12373.
262. Y. Yang *et al.*, *Nano Lett.* **2010**, *10*, 1486.
263. <http://sionpower.com/pdf/articles/SionPowerECS.pdf>.

# APPENDIX

## A-1. HRTEM IMAGE OF CTF-1







## **A-2. AB-INITIO CALCULATION AND TIGHT-BINDING MODEL**

Electronic structure calculations were performed in the framework of density-functional theory (DFT) using full potential local-orbital scheme implemented in FPLO codes [Refs A2-1,-2]. The exchange-correlation energy functional was evaluated within the generalized gradient approximation (GGA), using the Perdew, Burke, and Ernzerhof parametrization [Ref. A2-3]. Previous reported data<sup>141</sup> on the crystal structure of CTF-1 was used and calculated the density of states (DOS) corresponding to the ground state energy of the optimized geometry of the system, for monolayers and bulk multi-layers of CTF-1 and CTF-2 compounds. The geometry optimization was carried out by evaluating the atomic forces on each atom with a convergence criterion of 1 meV/Å.

### **Refereces**

- A2-1. Koepnik K.; Eschrig H. Full-potential nonorthogonal local-orbital minimum-basis band-structure scheme. *Phy. Rev. B* **1999**, 59, 1743-1757.
- A2-2. <http://www.fplo.de>.
- A2-3. Perdew J. P.; Burke K.; Ernzerhof M. Generalized Gradient Approximation Made Simple M. *Phys. Rev. Lett.* **1996**, 77, 3865-3868.

### **Versicherung**

Hiermit versichere ich, dass ich die vorliegende Arbeit ohne unzulässige Hilfe Dritter und ohne Benutzung anderer als der angegebenen Hilfsmittel angefertigt habe; die aus fremden Quellen direkt oder indirekt übernommenen Gedanken sind als solche kenntlich gemacht. Die Arbeit wurde bisher weder im Inland noch im Ausland in gleicher oder ähnlicher Form einer anderen Prüfungsbehörde vorgelegt.

Ich erkenne die Promotionsordnung der Technischen Universität Dresden der Fakultät Mathematik und Naturwissenschaften in ihrer Fassung vom 24. 04. 2013 an und versichere weiterhin, dass bisher kein früheres, erfolgloses Promotions verfahren statt gefunden hat.

Dresden, 24.04.2013

Ken Sakaushi